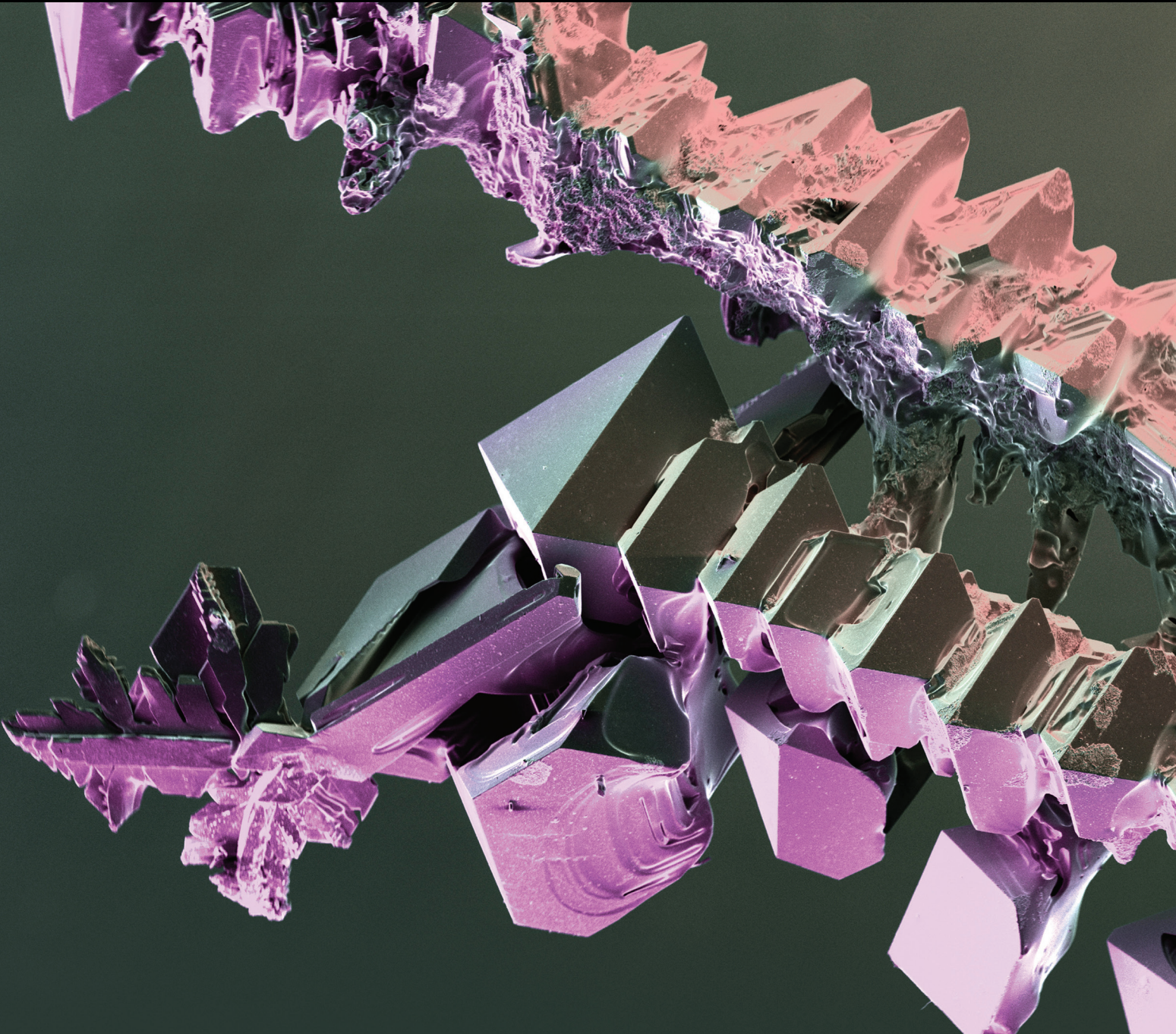


International Journal of Chemical Engineering

Multiphase Flow and Transfer Phenomenon

Lead Guest Editor: Wei Wang

Guest Editors: Panagiota Angeli, Yueshe Wang, and Bin Hu





Multiphase Flow and Transfer Phenomenon

International Journal of Chemical Engineering

Multiphase Flow and Transfer Phenomenon

Lead Guest Editor: Wei Wang

Guest Editors: Panagiota Angeli, Yueshe Wang, and Bin Hu



Copyright © 2017 Hindawi. All rights reserved.

This is a special issue published in “International Journal of Chemical Engineering.” All articles are open access articles distributed under the Creative Commons Attribution License, which permits unrestricted use, distribution, and reproduction in any medium, provided the original work is properly cited.

Editorial Board

Jerzy Baldyga, Poland
Mostafa Barigou, UK
Gino Baron, Belgium
Giuseppe Caputo, Italy
Raghunath V. Chaudhari, USA
Jean-Pierre Corriou, France
S. Déon, France
Donald L. Feke, USA
Michael Harris, USA

Xijun Hu, Hong Kong
M. G. Ierapetritou, USA
K. E. Kakosimos, Qatar
Iftekhar A. Karimi, Singapore
Bhaskar Kulkarni, India
Deepak Kunzru, India
Janez Levec, Slovenia
Jose C. Merchuk, Israel
Badie I. Morsi, USA

Dmitry Murzin, Finland
Doraiswami Ramkrishna, USA
Jose Alberto Romagnoli, USA
Evangelos Tsotsas, Germany
Maurizio Volpe, Italy
Junwu Wang, China
Jaime Wisniak, Israel
King Lun Yeung, Hong Kong

Contents

Multiphase Flow and Transfer Phenomenon

Wei Wang, Panagiota Angeli, Yueshe Wang, and Bin Hu
Volume 2017, Article ID 5083086, 2 pages

Study on Influence of Fluid Parameters on Axial Coupled Vibration of Pipeline Conveying Multiphase Flow

Ming Chen, Jimiao Duan, Dan Shu, Long Huang, and Xiaochen Chen
Volume 2017, Article ID 4824376, 10 pages

Investigation on the Transition Criterion of Smooth Stratified Flow to Other Flow Patterns for Gas-Hydrate Slurry Flow

Bohui Shi, Jiaqi Wang, Yifan Yu, Lin Ding, Yang Liu, and Haihao Wu
Volume 2017, Article ID 9846507, 13 pages

Coalbed Methane Production System Simulation and Deliverability Forecasting: Coupled Surface Network/Wellbore/Reservoir Calculation

Jun Zhou, Guangchuan Liang, Tao Deng, Shiwei Zhou, and Jing Gong
Volume 2017, Article ID 8267529, 13 pages

Route Optimization of Pipeline in Gas-Liquid Two-Phase Flow Based on Genetic Algorithm

Jun Zhou, Guangchuan Liang, Tao Deng, and Jing Gong
Volume 2017, Article ID 1640303, 9 pages

Numerical Simulation on Structure Optimization of Liquid-Gas Cylindrical Cyclone Separator

Peng Chang, Tian Hu, Li Wang, Sen Chang, Tianjing Wang, and Yueshe Wang
Volume 2016, Article ID 3187631, 9 pages

Editorial

Multiphase Flow and Transfer Phenomenon

Wei Wang,¹ Panagiota Angeli,² Yueshe Wang,³ and Bin Hu²

¹Beijing Key Laboratory of Urban Oil & Gas Distribution Technology, China University of Petroleum, Beijing, China

²Department of Chemical Engineering, University College London, Torrington Place, London WC1E 7JE, UK

³State Key Laboratory of Multiphase Flow in Power Engineering, Xi'an Jiaotong University, Xi'an 710049, China

Correspondence should be addressed to Wei Wang; w.wang@cup.edu.cn

Received 23 May 2017; Accepted 23 May 2017; Published 9 July 2017

Copyright © 2017 Wei Wang et al. This is an open access article distributed under the Creative Commons Attribution License, which permits unrestricted use, distribution, and reproduction in any medium, provided the original work is properly cited.

The main goal of this special issue was to gather the experimental, theoretical, or numerical research work emphasizing the contributions to the investigation of multiphase flow and heat transfer process. Multiphase flow is widespread in various fields, including power, chemical, petroleum, food, biomedical, metallurgical, nuclear, and hydraulic engineering. Specifically, in oil field, multiphase flow induces many problems ranging from reservoir to pipeline network. Studies on phase distribution and heat or mass transfer are fundamental to give insight into the complicated principle and the application prospect. The papers selected for this topical issue concentrate on numerical work that illustrates the practical problem and optimizes the production process. As such, they provide timely and valuable research results in petroleum field that we are pleased to share with the readers. We would like to thank all the authors for submitting their nice papers and all the referees for their excellent feedback.

This special issue includes five papers, where two papers cover the coalbed methane production, with one related to route optimization and the other concerning production simulation and deliverability forecast. One paper represents the structure optimization of liquid-gas separators by numerical simulation. In addition, one paper simulates the influence of fluid parameters on the vibration of pipeline. Finally, one paper presents both the experimental and simulated observation on the transition criterion from the stratified flow to other flow patterns in gas-hydrate slurry flow.

In the paper entitled "Route Optimization of Pipeline in Gas-Liquid Two-Phase Flow Based on Genetic Algorithm," J. Zhou et al. establish an automatic route optimization model

solved by the combination of Generic Algorithm and steady-state Generic Algorithm and discuss the influence of the parameter setting on the results. This method is also applied to determining the pipeline route in coalbed methane field in Shanxi Province, China, and proved to be feasible.

In the paper "Numerical Simulation on Structure Optimization of Liquid-Gas Cylindrical Cyclone Separator," P. Chang et al. represent a three-dimensional turbulence model to describe the multiphase flow field in the cylindrical cyclone separators which is widely used in industrial process and also investigate the dependence of separation efficiency on the separator length, the gas phase outlet diameter, and the inlet shape. Therefore, the optimal geometrical structure of the separator achieving a high efficiency of 86.15% is given by the author.

In the paper entitled "Study on Influence of Fluid Parameters on Axial Coupled Vibration of Pipeline Conveying Multiphase Flow," M. Chen et al. analyze the effect of the fluid parameters, including void fraction, density ratio, and elastic modulus ratio between solid phase and liquid phase, on the dynamic vibration of the pipe system conveying multiphase flow by numerical models when the valve at the end of pipe is rapidly closed.

In the paper "Coalbed Methane Production System Simulation and Deliverability Forecasting: Coupled Surface Network/Wellbore/Reservoir Calculation," J. Zhou et al. predicts 10 years' water and gas production and formation pressure of a Coalbed methane field with coupled surface/wellbore/reservoir calculation architecture. This paper describes the wellbore pressure drop simulation model,

surface pipeline network simulation model, and reservoir calculation model of CBM.

In the paper entitled "Investigation on the Transition Criterion of Smooth Stratified Flow to Other Flow Patterns for Gas-Hydrate Slurry Flow," B. Shi et al. develop a stability criterion for gas-hydrate slurry stratified flow with a model based on one-dimensional two-phase flow model and perturbation method after the consideration of some unstable factors including shear stress, gravity, surface tension, and the mass transfer change at the formation of hydrate, and also the criterion is validated by a series of gas-hydrate slurry flow experiments in a high pressure horizontal flow loop.

Wei Wang
Panagiota Angeli
Yueshe Wang
Bin Hu

Research Article

Study on Influence of Fluid Parameters on Axial Coupled Vibration of Pipeline Conveying Multiphase Flow

Ming Chen, Jimiao Duan, Dan Shu, Long Huang, and Xiaochen Chen

Department of Petroleum Supply Engineering, Logistical Engineering University, Chongqing 401311, China

Correspondence should be addressed to Ming Chen; chenchen8201@126.com

Received 15 November 2016; Revised 7 April 2017; Accepted 9 May 2017; Published 12 June 2017

Academic Editor: Dmitry Murzin

Copyright © 2017 Ming Chen et al. This is an open access article distributed under the Creative Commons Attribution License, which permits unrestricted use, distribution, and reproduction in any medium, provided the original work is properly cited.

Taking a slurry reservoir-pipeline-valve system as research object, axial dynamic vibrations of pipe system were induced by coupled hydraulic transient due to rapid closure of valve at the end of pipe. The influences of fluid parameters in multiphase flow, including void fraction, density ratio, and elastic modulus ratio between solid phase and liquid phase, on vibration behaviors of pipe system were analyzed. Results of this study show that wave velocities of pressure and stress can be attenuated evidently when void fraction in multiphase fluid is increased appropriately; meanwhile, the amplitudes of pressure fluctuation and pipe vibration are also weakened obviously. With the increase of density ratio between solid phase and liquid phase, the vibrational intension of pipe system becomes stronger and stronger. In this instance, the increments of vibrational energy mainly concentrate in fluid, which leads the pressure energy of fluid to rise up quickly. When elastic modulus ratio between solid phase and liquid phase increases, the total elasticity of fluid decreases gradually. At the same time, both pressure energy of fluid and vibrational intension of pipe are enhanced but the increments are very slight.

1. Introduction

As a kind of the excellent transportation mode, piping systems are widely used in many fields such as marine engineering, nuclear industries, and petroleum engineering. In the operational process of piping system, an extreme hydraulic state, that is, water hammer, is often induced by the disturbance of dynamic or controlling system. Due to the effect of fluid-structure interaction (FSI), water hammer may cause intense coupled vibration of piping system, which decreases the reliability and performance of system and even will lead to serious disasters further. Therefore, it is of great and immediate significance to accurately analyze the coupled vibration principle of piping system for taking safety precautionary measures, ensuring reliable operation of the whole systems, reducing the loss of energy sources, and so on.

Extensive investigations have been carried out on coupled vibration of piping system in the past years. Several coupled vibration models describing nonlinear dynamic behaviors of liquid-conveying pipes were developed by Paidoussis and

Li [1], Zhang and Huang [2], Gorman et al. [3], Lee and Chung [4], and Omer et al. [5], respectively. To obtain the coupled vibration response results of piping system in time and frequency domain, different numerical methods, such as MOC, FEM, MOC-FEM, traveling wave method, and transfer matrix method, were used by Wiggert and Tijsseling [6], Kochupillai et al. [7], Zanganeh et al. [8], Ren et al. [9], and Xu et al. [10], respectively.

By virtue of different theoretical models and numerical procedures, some specific researches were concerned with the influence of fluid or structural parameters on the coupled vibration characteristics of piping system. Zhang [11] conducted an investigation into the effects of fluid and shell parameters on the coupled frequencies based on wave propagation approach. Li et al. [12] analyzed the factors affecting the characteristics of FSI by changing the bend radius and angle of curved pipe. Adamkowski et al. [13] carried on their research on the influence of dynamic Poisson effect onto pressure records during hydraulic transient with FSI using experimental data and numerical computations. Yang and Fan [14] studied the influences of pipe structural

damping, pipe Poisson's ratio, and pipe wall thickness on vibration responses of the RPV system. Liu et al. [15] analyzed influences of steam parameters, that is, steam pressure and velocity, on the natural characteristics of steam pipeline systems. Lin et al. [16] discussed the effect of fluid parameters, including liquid pressure, flow velocity, and axial force, on vibration characteristics of hydraulic pipe of aero-engine. Zhang et al. [17] conducted their investigation into the influences of internal flow, the changes of internal flow velocity, and top tension amplitude on coupled vibration of deep-water riser. Eslami et al. [18] studied the effect of aspect ratio of length to diameter on the dynamic response of a fluid-conveying pipe based on the Timoshenko beam model. Their results indicate that the natural frequencies decrease with the increasing of internal fluid velocity and the critical velocity decreases with the decreasing of aspect ratio. Gu et al. [19] studied vibration behavior of a fluid-conveying cracked pipe surrounded by a viscoelastic medium. In their works, the effect of open crack parameters and flow velocity profile shape inside the pipe on natural frequency and critical flow velocity of the system has been analytically investigated. Liu et al. [20] analyzed the influences of bound manner, restraint stiffness, foundation vibration parameters, and structural parameters on pipe outlet pressure fluctuation amplitude. Tian et al. [21] studied vibration characteristics of pipeline under the action of the gas pressure pulsation and the relationships between the gas column natural frequency and orders, the gas pressure pulsation and orders, the exciting force and aspect ratio, and the vibration displacement and velocity of pipeline are acquired. Meng et al. [22] developed a simple FSI model and investigated the effect of internal flow velocity on the cross-flow vortex-induced vibration of a cantilevered pipe discharging fluid.

According to the collected literatures, these researches on coupled vibration of piping system mainly focus on the development and solution of numerical models, the critical flow velocity, parameters resonance of pipe structures, and so on. Furthermore, the pure liquid is often considered as research objects, whereas the liquid containing gas phase and solid phase is rarely taken into account [23]. Actually, with the wide application of mixed transportation technology for multiphase flow or the effect of objective factors (such as interlarding the liquid with some gas or solid impurities), the actual fluid in the pipelines always exists as a kind of multiphase fluids and gas-liquid-solid three-phase mixed flow is the most general and representative in multiphase flows. Thus, this paper takes gas-liquid-solid three-phase mixed flow as research object and the influences of parameters, including void fraction, density ratio, and elastic modulus ratio between solid phase and liquid phase, on vibration characteristics of piping system are studied to illuminate coupled water hammer problems of pipelines further.

2. Mathematical Model

Hydraulic transportation is often used to transport concentrate and tailings in the metallurgical industry as well as cinder in the coal and power industries. To facilitate hydraulic transportation by pipeline, decreasing the wear of

the equipment, reducing the conveying velocity, and lowering the operational costs, the fine solid granular materials are usually applied to maintain an even suspended motion in the effect of turbulent diffusion. In such condition, this kind of gas-liquid-solid three-phase mixed flow formed by solid granule, liquid, and some other small amount of gas mixed in is relatively stable, and the concentration of every phase is well-distributed at the cross-section of pipeline. Generally, for such kind of piping system, the flow is treated as homogeneous flow or pseudo-homogeneous flow which can be analyzed on the basis of homogeneous flow theory [24].

To obtain a set of convenient FSI governing equations for piping system conveying the mentioned three-phase flow in this paper, the following assumptions are made:

- (a) Gas phase, liquid phase, and solid phase are mixed evenly, and there are no velocity difference and no mass exchange among the three phases in an adiabatic state.
- (b) Cross-section changes and deformations along the pipe are small; that is, $\partial A_f / \partial x \approx 0$.
- (c) The material of pipe wall is isotropic and presents a linear-elastic mechanical behavior.
- (d) Liquid flashing is not considered in the process of hydraulic transient, and fluid velocity is a cross-section averaged scalar value.

Because many pipes in practice have relatively thick walls, for example, high-pressure pipes in chemical and power industries, the usual assumption of thin-walled pipes is not adopted in this research. Therefore, the ratio e/R of wall thickness to pipe-radius cannot be neglected. Based on the above assumptions, the FSI model can be described by the following expression [25]:

$$\mathbf{A} \frac{\partial \Phi}{\partial t} + \mathbf{B} \frac{\partial \Phi}{\partial x} = \mathbf{F}, \quad (1)$$

where

$$\Phi = \begin{bmatrix} V_m \\ H \\ U \\ \sigma \end{bmatrix};$$

$$\mathbf{A} = \begin{bmatrix} 1 & 0 & 0 & 0 \\ 0 & K^* \rho_m g & 0 & 0 \\ 0 & 0 & 1 & 0 \\ 0 & \frac{2\mu R^2 \rho_m g}{[(2Re + e^2) E]} & 0 & \frac{-1}{E} \end{bmatrix};$$

$$\mathbf{B} = \begin{bmatrix} 0 & g & 0 & 0 \\ 1 & 0 & -2\mu \left(1 + \frac{e}{R}\right) & 0 \\ 0 & 0 & 0 & \frac{-1}{\rho_p} \\ 0 & 0 & 1 & 0 \end{bmatrix};$$

$$\mathbf{F} = \begin{bmatrix} -\frac{F_m}{(\rho_m A_f)} - g \sin \alpha \\ 0 \\ \frac{F_m}{(\rho_p A_p)} - g \sin \alpha \\ 0 \end{bmatrix};$$

$$K^* = \frac{1}{K_m} + \frac{4R(1 - \mu^2)(R + e)}{(2REe + Ee^2)};$$

$$K_m = \left[\frac{\nu_g}{K_g} + \frac{\nu_s}{K_s} + \frac{(1 - \nu_g - \nu_s)}{K_1} \right]^{-1};$$

$$\rho_m = \rho_g \nu_g + \rho_s \nu_s + \rho_l (1 - \nu_g - \nu_s);$$

$$F_m = \frac{\rho_m f_m A_f V_m |V_m| \left\{ 1 + \varphi \left[\nu_s (\rho_s / \rho_l - 1) + \nu_g \sin \alpha \right] \right\}}{(4R)}.$$
(2)

The characteristic formula for (1) is $|\mathbf{B} - \lambda \mathbf{A}| = 0$ and its four unequal real roots are

$$\lambda_{1,2} = \pm C_m = \pm \sqrt{\frac{1}{2} \left[q^2 - (q^4 - 4a_m^2 a_p^2)^{1/2} \right]},$$

$$\lambda_{3,4} = \pm C_p = \pm \sqrt{\frac{1}{2} \left[q^2 + (q^4 - 4a_m^2 a_p^2)^{1/2} \right]},$$
(3)

where $q^2 = a_m^2 + a_p^2 + (4\mu^2 R(R + e)/(2R + e)e)(\rho_m/\rho_p)a_m^2$.

3. Numerical Scheme

To the numerical simulation of water hammer events without FSI, MOC is always regarded as an excellent numerical strategy. However, for solving FSI model, MOC may introduce excessive numerical dispersion and attenuation in the solutions, which will induce a bad influence on the accuracy of computational results [26]. To avoid the embarrassment, flux vector splitting method is used to solve the proposed FSI model.

Make (1) flux splitting and numerical discretization based on Lax-Wendroff central difference scheme and Warming-Beam upwind difference scheme, both of which possess second-order precision in time and space [27]. According to the literature [28], (1) can be written as the following difference form:

$$\mathbf{W}_j^{n+1} = \mathbf{W}_j^n - \frac{\Delta t}{\Delta x} \left(\mathbf{D}_{j+\frac{1}{2}}^n \mathbf{1} - \mathbf{D}_{j-\frac{1}{2}}^n \mathbf{1} \right) + \Delta t \mathbf{T} \mathbf{F}_j^n,$$

$$\mathbf{D}_{j+1/2} = \mathbf{Y}_{j+1/2}^+ + \mathbf{Y}_{j-1/2}^-,$$

$$\mathbf{D}_{j-1/2} = \mathbf{Y}_{j-1/2}^+ + \mathbf{Y}_{j-3/2}^-,$$

$$\mathbf{Y}_{j+1/2}^+ = \mathbf{Y}_j^+ + \frac{1}{2} \left(\mathbf{I} - \frac{\Lambda^+ \Delta t}{\Delta x} \right)$$

$$* \text{MINMOD}(\Delta \mathbf{Y}_{j-1}^+, \Delta \mathbf{Y}_j^+),$$

$$\mathbf{Y}_{j-1/2}^- = \mathbf{Y}_{j+1}^- - \frac{1}{2} \left(\mathbf{I} + \frac{\Lambda^- \Delta t}{\Delta x} \right)$$

$$* \text{MINMOD}(\Delta \mathbf{Y}_j^-, \Delta \mathbf{Y}_{j+1}^-),$$

$$\Delta \mathbf{Y}_{j-1}^\pm = \mathbf{Y}_j^\pm - \mathbf{Y}_{j-1}^\pm,$$

$$\Delta \mathbf{Y}_j^\pm = \mathbf{Y}_{j+1}^\pm - \mathbf{Y}_j^\pm,$$

$$\Delta \mathbf{Y}_{j+1}^\pm = \mathbf{Y}_{j+2}^\pm - \mathbf{Y}_{j+1}^\pm,$$

(4)

where $\mathbf{W} = \mathbf{T} \mathbf{A} \Phi$; $\mathbf{T} = [t_{ij}]_{4 \times 4}$; for $i = 1$ or 2 , $t_{i1} = 1$, $t_{i2} = \lambda_i$, $t_{i3} = 2\mu(1 + e/R)\lambda_i^2/(C_p^2 - \lambda_i^2)$, $t_{i4} = 2\mu C_p^2(1 + e/R)\lambda_i/(C_p^2 - \lambda_i^2)$; for $i = 3$ or 4 , $t_{i1} = (2\mu R^2 \rho_m / (2Re + e^2)E)(C_m^2 \lambda_i^2 / (C_m^2 - \lambda_i^2))$, $t_{i2} = (2\mu R^2 \rho_m / (2Re + e^2)E)(C_m^2 \lambda_i^3 / (C_m^2 - \lambda_i^2))$, $t_{i3} = 1 - (4\mu^2(R^2 + Re)\rho_m / (2Re + e^2)E)(C_m^2 \lambda_i^2 / (C_m^2 - \lambda_i^2))$, $t_{i4} = \lambda_i$; $\mathbf{Y}^+ = \Lambda^+ \mathbf{W}$, $\mathbf{Y}^- = \Lambda^- \mathbf{W}$; $\Lambda^+ = \text{diag}(\lambda_1^+, \lambda_2^+, \lambda_3^+, \lambda_4^+)$, $\Lambda^- = \text{diag}(\lambda_1^-, \lambda_2^-, \lambda_3^-, \lambda_4^-)$, $\lambda_i^+ = (\lambda_i + |\lambda_i|)/2$, $\lambda_i^- = (\lambda_i - |\lambda_i|)/2$; \mathbf{I} is an identity matrix; MINMOD(a, b) function is described as follows: when $ab \leq 0$, the value of function equals zero; when $ab > 0$, the value of function equals the lesser one of absolute values of a and b .

The stability condition of the above difference schemes is $Cr = \max(C_m, C_p)\Delta t/\Delta x \leq 1$. These equations are solved subject to boundary conditions at the upstream and downstream ends of the pipeline and initial conditions. For a pipeline connected to a reservoir with constant piezometric head H_{up} and an unfixed valve at the upstream and downstream ends, respectively, the boundary conditions can be derived from Rankine-Hugoniot condition [29]:

For upstream end,

$$\Phi_0^{n+1} = \begin{bmatrix} V_{m0}^{n+1} \\ H_0^{n+1} \\ U_0^{n+1} \\ \sigma_0^{n+1} \end{bmatrix} = \begin{bmatrix} V_{m1}^n + \frac{(H_{up} - H_1^n)g}{C_m} \\ H_{up} \\ 0 \\ \sigma_1^n + C_p \rho_p U_1^n \end{bmatrix}. \quad (5)$$

For downstream end,

TABLE 1: Physical parameters of the RPV system.

Parameter name	Parameter unit	Parameter value
Length of pipe	m	20
Outer diameter of pipe	m	0.813
Pipe wall thickness	m	0.008
Young's modulus of pipe material	GPa	210
Density of the pipe material	kg/m ³	7900
Poisson's ratio	—	0.3
Initial velocity of internal flow in pipe	m/s	1
Pressure behind valve	MPa	0

$$\Phi_N^{n+1} = \begin{bmatrix} V_{mN}^{n+1} \\ H_N^{n+1} \\ U_N^{n+1} \\ \sigma_N^{n+1} \end{bmatrix} = \begin{bmatrix} U_N^{n+1} \\ H_{N-1}^n - \frac{C_m (U_N^{n+1} - V_{mN-1}^n)}{g} \\ \frac{(A_f \rho_m g H_{N-1}^n + A_f C_m \rho_m V_{mN-1}^n + A_p C_p \rho_p U_{N-1}^n - A_p \sigma_{N-1}^n)}{(C_m \rho_m A_f + C_p \rho_p A_p)} \\ \frac{A_f \rho_m g H_N^{n+1}}{A_p} \end{bmatrix}. \quad (6)$$

4. Discussion about the Influence of Correlative Parameters

A slurry reservoir-pipeline-valve system shown in Figure 1 is taken as a research object in this paper. The pipe and valve are allowed to move freely in the axial direction. The physical parameters of this RPV system are listed in Table 1.

In the multiphase fluid, water is taken as liquid phase, where the density is 1000 kg/m³ and bulk modulus equals 2.14 GPa. The coupled water hammer event is induced by instantaneous closure of valve at downstream end.

4.1. The Influence of Void Fraction on Vibration Characteristics of Piping System. Void fraction is one of the most important parameters of multiphase fluid. The bulk modulus of gas phase is usually 4~6 quantity grades less than that of liquid phase and solid phase. So even if the change of void fraction is very inconspicuous, the influence on vibration characteristics of piping system cannot be ignored. Assume the solid phase in the slurry is iron concentrate, whose dry density is 4760 kg/m³, elasticity modulus is 105 GPa, solid particulate diameter is about 0.071 mm, and bulk concentration equals 0.168. The gas phase is air bubble, whose bulk modulus is obtained by [30]

$$K_g = \rho_m g H \gamma. \quad (7)$$

The curves of pressure wave velocity with the change of void fraction are shown in Figure 2. Pressure wave velocity decreases sharply in the process of void fraction increasing from 0 to 0.001. When void fraction exceeds 0.2, pressure

wave velocity tends toward stabilization. Before and after considering fluid-structure interaction, the difference between two curves of pressure wave velocity is not obvious. When void fraction equals zero, pressure wave velocity without FSI is 861 m/s, exceeding the value of pressure wave velocity with FSI, that is, 839 m/s. The curves of stress wave velocity with the change of void fraction are shown in Figure 3. According to Figure 3, the variational trend of stress wave velocity is similar to that of pressure wave velocity when FSI is considered. However, when FSI is not considered, stress wave velocity is a constant. This is because stress wave velocity is only related to elastic modulus and density of pipe material in the equation for stress wave velocity without FSI.

The pressure response and pipe structure vibration at valve are analyzed with the void fraction in the slurry equaling 0.000035, 0.00035, and 0.0035, respectively, as shown in Figures 4 and 5. As void fraction increases, the amplitudes of pressure and structure vibration decrease obviously and the fluctuation frequency also reduces. Such situations are similar to system energy dissipation induced by structure damp of piping system. So the gas phase can be regarded as a kind of energy dissipation damp. Increasing appropriately void fraction in the conveyed medium may effectively weaken the fluctuations of fluid pressure and pipe vibration on the premise of maintaining the current flow pattern.

4.2. The Influence of Density Ratio between Solid Phase and Liquid Phase on Vibration Characteristics of Piping System. At present, in the industrial production, many kinds of solid material particulates can be conveyed by hydraulic



FIGURE 1: Sketch of slurry reservoir-pipeline-valve system.

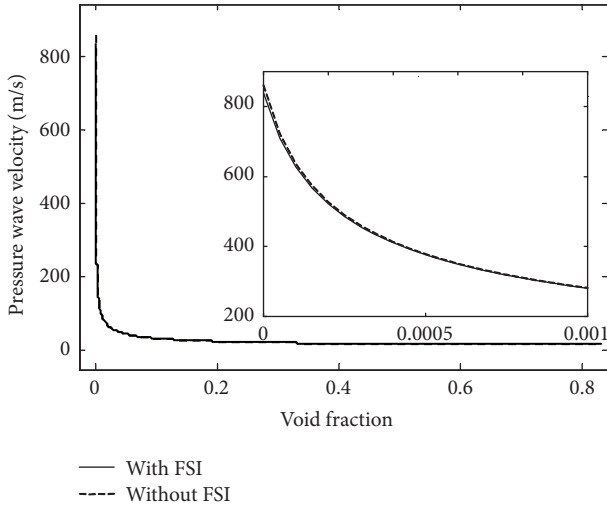


FIGURE 2: Variation of pressure wave velocity with void fraction.

transportation in pipeline. With the further investigation, it can be pointed out that the influence of density ratio between solid phase and liquid phase (density ratio for short in the following content) on dynamic behaviors of piping system is quite conspicuous. The influence of slurry concentration (i.e., solid phase content in the fluid) on pressure wave velocity shows some obvious discrepancies because of different density ratios.

Assume the content of void fraction in the slurry maintains 0.00035. The influences of slurry concentration on pressure wave velocity are shown in Figure 6 with different density ratios. According to Figure 6, the density ratio has a critical value (it is about 1.15 in this instance). When density ratio is less than the critical value, pressure wave velocity will quicken with increase of slurry concentration, whereas pressure wave velocity will decrease. The curves of stress wave velocity with density ratios are shown in Figure 7. According to Figure 7, the changing trends of stress wave velocity with the slurry concentration are not affected by density ratios. Only under different density ratios, increasing extent of stress wave velocities varies.

Let slurry concentration equal 0.568 and density ratios equal 0.5~5.0 with an interval of 0.3. Then the maximum values and virtual values of fluid pressure and vibration velocity at valve are shown in Figures 8 and 9.

According to the computational curves in Figures 8 and 9, the maximum values and virtual values of fluid pressure are enhanced with the increase of density ratio, and due to junction coupled effect, the axial vibration velocity has same

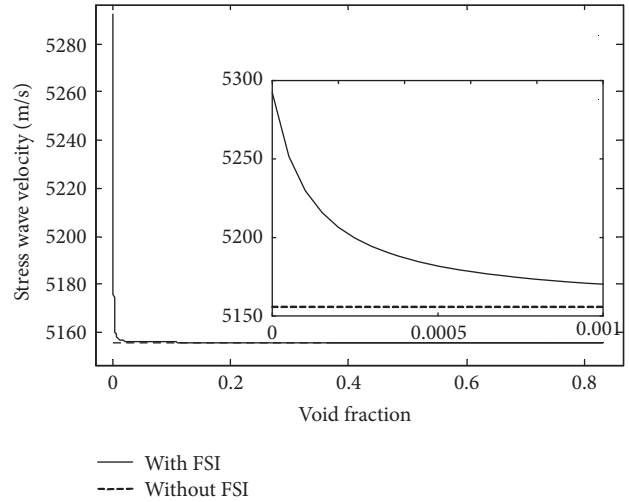


FIGURE 3: Variation of stress wave velocity with void fraction.

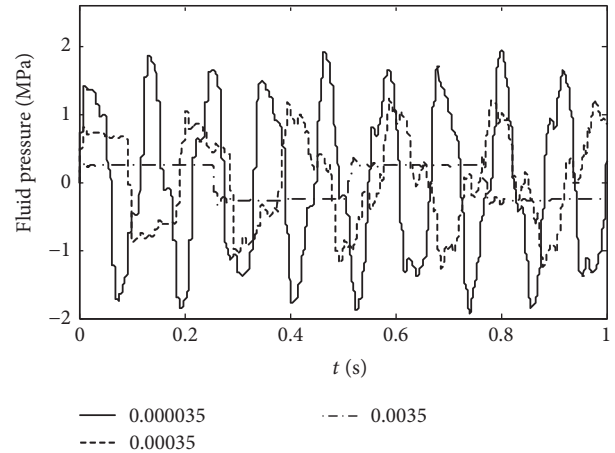


FIGURE 4: Comparison among pressure responses at valve with the different void fraction.

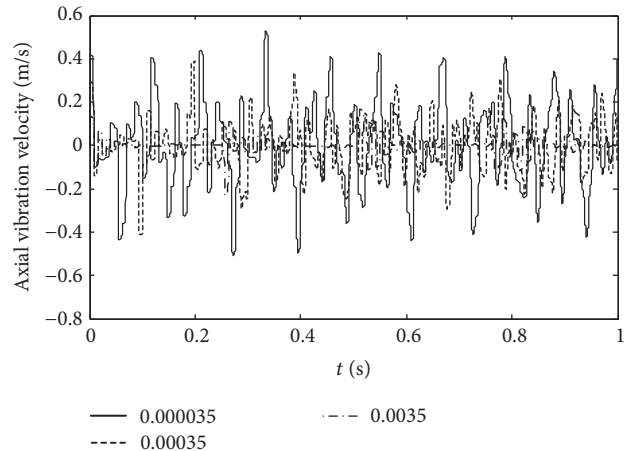


FIGURE 5: Comparison among axial vibration velocity responses at valve with the different void fraction.

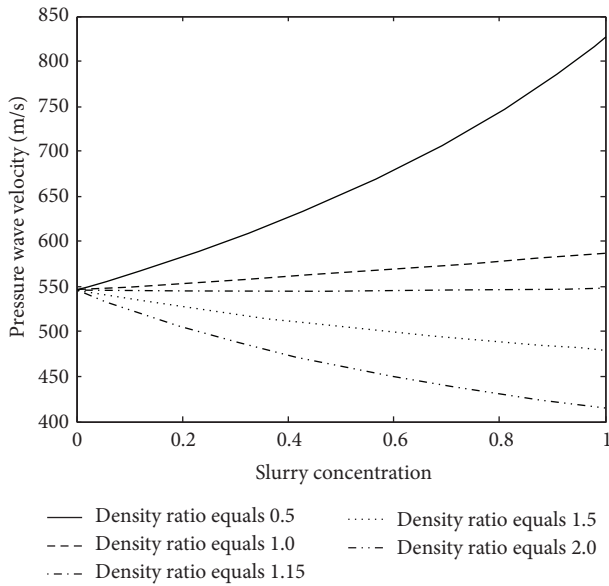


FIGURE 6: Influence of density ratio on pressure wave velocity.

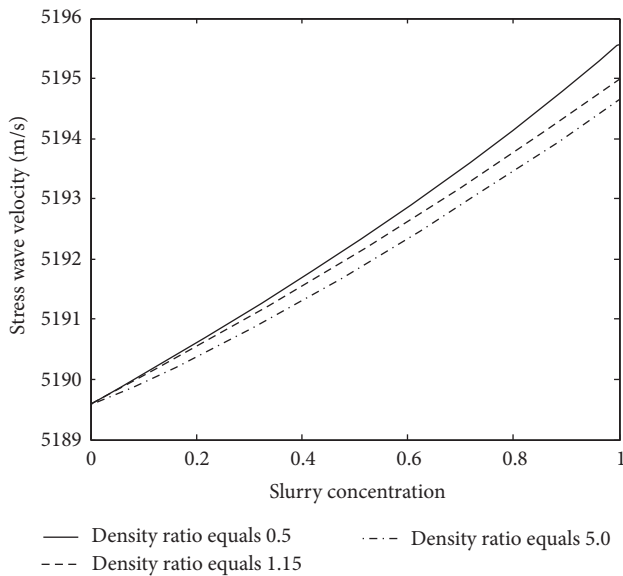


FIGURE 7: Influence of density ratio on stress wave velocity.

changing trend. The phenomenon explains that the vibration extent of piping system will be enhanced with the increase of density ratio. Combined with the computational curves in Figure 6, pressure wave velocity is decreased because of the increase of density ratio, but the total density of fluid gains more enhancement. Then the inertia of unit volume of fluid is stronger and the intensity of water hammer pressure will be enhanced correspondingly from the principle of inertial water hammer. The increasing extent of virtual values of pipe vibration velocity (i.e., vibration energy) is less than that of virtual values of fluid pressure (i.e., pressure energy), which indicates that the increments of systemic vibration energy mainly centralize in the slurry with the increase of density

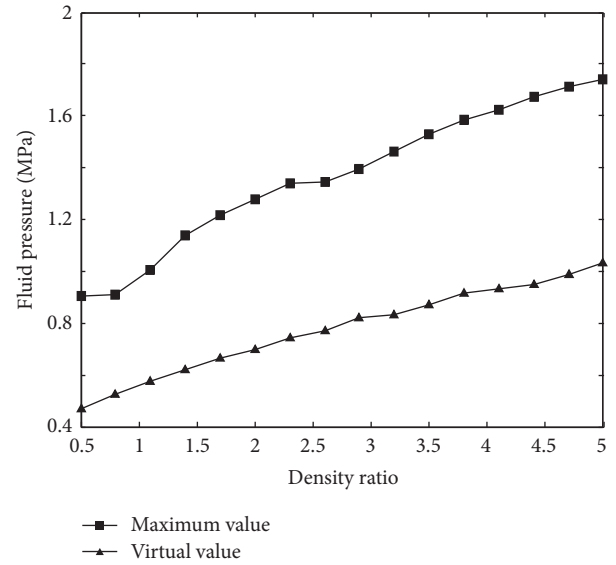


FIGURE 8: Pressure responses of fluid at valve.

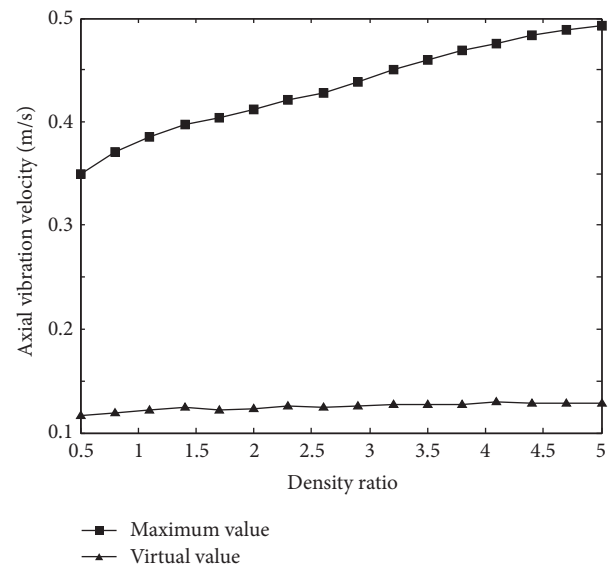


FIGURE 9: Axial vibration velocity responses of pipe at valve.

ratio. Hence the pressure energy in the slurry can get a more rapid rise.

4.3. The Influence of Elastic Modulus Ratio between Solid Phase and Liquid Phase on Vibration Characteristics of Piping System. As the slurry concentration changes, different elastic modulus ratio between solid phase and liquid phase (elastic modulus ratio for short in the following content) may lead to different transformation of overall bulk modulus of multiphase fluid and further influences the changing trend of pressure and stress wave velocity. The influence of different elastic modulus on pipe stress wave velocity is shown in Figure 10, in which solid line and broken line denote density ratio equaling 4.76 or 0.76, respectively. According to Figure 10,

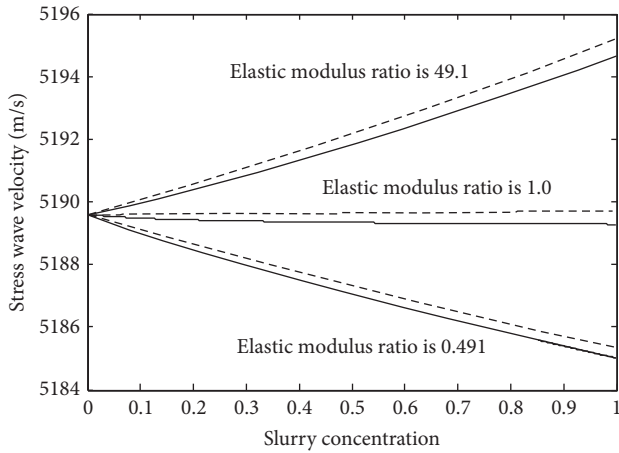


FIGURE 10: Influence of elastic modulus ratio on stress wave velocity.

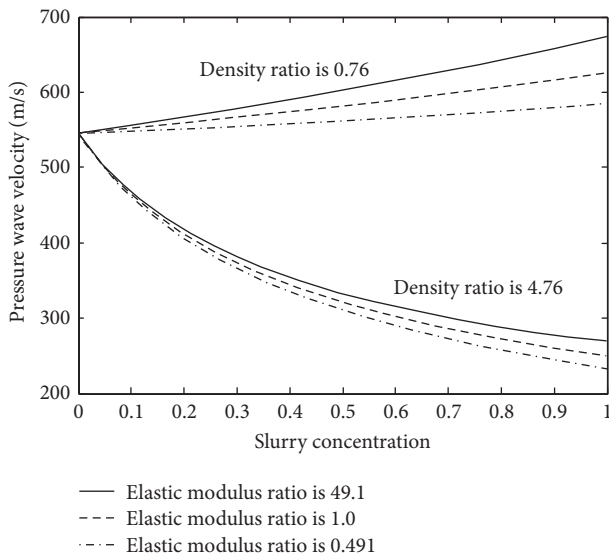


FIGURE 11: Influence of elastic modulus ratio on pressure wave velocity.

the influence of elastic modulus ratio on stress wave velocity is obvious, whereas density ratio has a less effect on stress wave velocity comparatively. Similarly there exists a critical value (it is about 1.0 in this instance) in elastic modulus ratio. When elastic modulus ratio is less than the critical value, stress wave velocity will decrease with the increase of slurry concentration. Otherwise stress wave velocity will quicken with the increase of slurry concentration.

The influence of elastic modulus ratio on pressure wave velocity is shown in Figure 11. As presented in this figure, with the transformation of slurry concentration, the changing trend of pressure wave velocity is not affected by elastic modulus ratio but the changing extent of pressure wave velocity is influenced. In general, its influence on pressure wave velocity is less than that of density ratio. In addition, according to Figure 11, the pressure wave velocity grows with the increase of elastic modulus ratio at the same slurry concentration. This is because the increase of elastic modulus ratio can make the

total bulk modulus of multiphase fluid augment. It means that the slurry becomes harder gradually and its elasticity decreases and rigidity increases. So the pressure wave velocity travels faster and faster. If bulk modulus of the slurry is infinite, pressure wave velocity will become infinite too.

Let the slurry concentration equal 0.568 and density ratio equal 0.76 or 4.76, respectively. The values of elastic modulus ratio are assigned between 0.1 and 50. Then the maximum and virtual values of pressure and vibration velocity at valve are shown in Table 2.

According to the data as shown in Table 2, although density ratio takes different values, the maximum and virtual values of slurry pressure always grow with the increase of elastic modulus ratio. But the growth is low. When elastic modulus ratio exceeds a certain value (it is about 1.0 in this instance), the changing extent of slurry pressure response decreases and tends to be stable. Due to the junction coupled effect, the change of pipe axial vibration velocity is similar to that of slurry pressure response. The result shows that when the elasticity of slurry decreases to certain extent with the increase of elastic modulus ratio, its influence on pressure energy and vibration intensity of pipe can be ignored.

5. Conclusions

The slurry reservoir-pipeline-valve system is taken as a research object in this paper and the influences of physical parameters of multiphase fluid on system vibration response are analyzed. The main conclusions are as follows:

- (1) With the increase of void fraction, the wave velocities of pressure and stress decrease rapidly then tend to be stable. At the same time, the amplitudes of slurry pressure and pipe vibration decline obviously. So the gas phase can be regarded as a kind of energy dissipation damp. Increasing moderately void fraction can weaken slurry pressure and pipe vibration effectively if the current flow pattern is maintained.
- (2) For pressure wave velocity in the slurry, density ratio has a critical value. When density ratio is less than the critical value, pressure wave velocity will grow with the increase of slurry concentration; otherwise the pressure wave velocity will decrease. The changing trend of stress wave velocity with slurry concentration is not affected by density ratio. Just the increasing extent of stress wave velocity is dissimilar to the different density ratio. When density ratio increases, the vibration intensity of piping system grows too. The increment of vibration energy of pipe system is mainly concentrated in the slurry.
- (3) For stress wave velocity of pipe, there also exists a critical value in elastic modulus ratio. When elastic modulus ratio is less than the critical value, stress wave velocity decreases with the increase of slurry concentration. On the contrary, stress wave velocity will grow. However, the changing trends of pressure wave velocity with slurry concentration are not affected obviously by elastic modulus ratio and only small variations of its changing extent are shown with

TABLE 2: Numerical results with the different elastic modulus ratio.

Elastic modulus ratio	Slurry pressure/MPa (density ratio is 0.76)		Vibration velocity/m/s (density ratio is 0.76)		Slurry pressure/MPa (density ratio is 4.76)		Vibration velocity/m/s (density ratio is 4.76)	
	Maximum values	Virtual values	Maximum values	Virtual values	Maximum values	Virtual values	Maximum values	Virtual values
0.1	0.7053	0.3796	0.3059	0.0865	1.1811	0.7338	0.4240	0.0936
1.0	0.8605	0.4962	0.3620	0.1136	1.6601	0.9692	0.4833	0.1242
5.0	0.8978	0.5149	0.3671	0.1190	1.7122	0.9952	0.4885	0.1286
10.0	0.8992	0.5151	0.3677	0.1191	1.7164	0.9969	0.4891	0.1287
30.0	0.9008	0.5157	0.3682	0.1191	1.7192	0.9982	0.4895	0.1291
50.0	0.9011	0.5159	0.3682	0.1192	1.7193	0.9984	0.4895	0.1292

different elastic modulus ratio. The increase of elastic modulus enhances the pressure energy and vibrational intension slightly. When elastic modulus ratio grows to a certain extent, its influence on pressure energy and vibrational intension of pipe system can be ignored.

Nomenclature

V_m : Average velocity of multiphase fluid (m/s)
 H : Pressure head of multiphase fluid (m)
 U : Axial velocity of the pipe (m/s)
 σ : Axial normal stress of the pipe wall (Pa)
 E : Young's modulus of pipe wall material (Pa)
 μ : Poisson's ratio of pipe material
 R : Internal radius of the pipe (m)
 e : Thickness of pipe wall (m)
 A_p : Cross-sectional area of pipe wall (m²)
 A_f : Internal cross-sectional area of the pipe (m²)
 ρ_p : Density of pipe wall material (kg/m³)
 g : Gravity acceleration (m/s²)
 α : Inclination angle of the pipe (°)
 ρ : Density of each phase in multiphase fluid (kg/m³)
 v : Volume percentage of each phase in multiphase fluid
 K : Bulk modulus of each phase in multiphase fluid (Pa)
 x : Axial direction of the pipe (m)
 t : Time (s)
 f_m : Friction factor between pipe wall and multiphase fluid
 φ : Pressure coefficient
 a_m : Pressure wave velocity without FSI ($= (K * \rho_m)^{-0.5}$) (m/s)
 a_p : Axial stress wave velocity without FSI ($= (E/\rho_p)^{0.5}$) (m/s)
 Δt : Time step (s)
 Δx : Pipe element length (m)
 γ : Adiabatic exponent of air.

Superscripts

n : Time step number.

Subscript

j : Node number of the difference grid, $j = 0, 1, \dots, N$
 g : Gas phase
 s : Solid phase
 l : Liquid phase
 m : Mixed phase.

Conflicts of Interest

The authors declare that they have no conflicts of interest regarding the publication of this paper.

Acknowledgments

The authors acknowledge the financial support of the National Natural Science Foundation of China (Grant no. 51604282) and Chongqing Research Program of Basic Research and Frontier Technology (Grant nos. cstc2016jcyjA0171 and cstc2016jcyjA0095).

References

- [1] M. P. Paidoussis and G. X. Li, "Pipes conveying fluid: a model dynamical problem," *Journal of Fluids and Structures*, vol. 7, no. 2, pp. 137–204, 1993.
- [2] L. X. Zhang and W. H. Huang, "Nonlinear dynamical modeling of fluid-structure interaction of fluid-conveying pipes," *Journal of Hydrodynamics (Series A)*, vol. 15, no. 1, pp. 116–128, 2000.
- [3] D. G. Gorman, J. M. Reese, and Y. L. Zhang, "Vibration of a flexible pipe conveying viscous pulsating fluid flow," *Journal of Sound and Vibration*, vol. 230, no. 2, pp. 379–392, 2000.
- [4] S. I. Lee and J. Chung, "New non-linear modelling for vibration analysis of a straight pipe conveying fluid," *Journal of Sound and Vibration*, vol. 254, no. 2, pp. 313–325, 2002.
- [5] F. Omer, L. Y. Pan, and B. R. Li, "Study of transient transverse vibration for a pipe," *Journal of Engineering and Applied Sciences*, vol. 6, no. 2, pp. 114–121, 2011.
- [6] D. C. Wiggert and A. S. Tijsseling, "Fluid transients and fluid-structure interaction in flexible liquid-filled piping," *Applied Mechanics Reviews*, vol. 54, no. 5, pp. 455–481, 2001.
- [7] J. Kochupillai, N. Ganesan, and C. Padmanabhan, "A new finite element formulation based on the velocity of flow for water hammer problems," *International Journal of Pressure Vessels and Piping*, vol. 82, no. 1, pp. 1–14, 2005.
- [8] R. Zanganeh, A. Ahmadi, and A. Keramat, "Fluid—structure interaction with viscoelastic supports during waterhammer in a pipeline," *Journal of Fluids and Structures*, vol. 54, no. 4, pp. 215–234, 2015.
- [9] J. T. Ren, L. Lin, and J. S. Jiang, "Traveling wave method for pipe fluid-structure interaction," *Chinese Journal of Applied Mechanics*, vol. 22, no. 4, pp. 530–535, 2005.
- [10] Y. Xu, D. N. Johnston, Z. Jiao, and A. R. Plummer, "Frequency modelling and solution of fluid-structure interaction in complex pipelines," *Journal of Sound and Vibration*, vol. 333, no. 10, pp. 2800–2822, 2014.
- [11] X. M. Zhang, "Parametric studies of coupled vibration of cylindrical pipes conveying fluid with the wave propagation approach," *Computers and Structures*, vol. 80, no. 3, pp. 287–295, 2002.
- [12] Y. H. Li, G. M. Liu, and J. Ma, "Research on fluid-structure interaction in fluid-filled pipes," *Journal of Vibration and Shock*, vol. 29, no. 6, pp. 50–53, 2010.
- [13] A. Adamkowski, S. Henclik, and M. Lewandowski, "Experimental and numerical results of the influence of dynamic poison effect on transient pipe flow parameters," *IOP Conference Series: Earth and Environmental Science*, vol. 12, no. 1, pp. 1–9, 2010.
- [14] C. Yang and S.-J. Fan, "Influence of pipe parameters on fluid-structure coupled vibration of a fluid-conveying pipe," *Journal of Vibration and Shock*, vol. 30, no. 7, pp. 210–213, 2011.
- [15] G. M. Liu, H. Chen, and S. J. Li, "Research on the influence of steam parameters on dynamic characteristics of pipeline system," *Chinese Journal of Solid Mechanics*, vol. 33, no. 2, pp. 168–175, 2012.

- [16] J. Z. Lin, E. T. Zhou, L. S. Du, and B. C. Wen, "Effect of fluid parameters on vibration characteristics of hydraulic pipe of aero-engine," *Journal of Northeastern University (Natural Science)*, vol. 33, no. 10, pp. 1453–1456, 2012.
- [17] L. Zhang, H. Wu, Y. Yu, X. H. Zeng et al., "Axial and transverse coupled vibration characteristics of deep-water riser with internal flow," *Procedia Engineering*, vol. 126, pp. 260–264, 2015.
- [18] G. Eslami, V. A. Maleki, and M. Rezaee, "Effect of open crack on vibration behavior of a fluid-conveying pipe embedded in a visco-elastic medium," *Latin American Journal of Solids and Structures*, vol. 13, no. 1, pp. 136–154, 2016.
- [19] J. Gu, T. Ma, and M. Duan, "Effect of aspect ratio on the dynamic response of a fluid-conveying pipe using the Timoshenko beam model," *Ocean Engineering*, vol. 114, pp. 185–191, 2016.
- [20] S. Liu, H. L. Zhang, and H. Peng, "Fluid-pipe coupling axis vibration characteristics induced by foundation vibration," *Journal of Beijing University of Aeronautics and Astronautics*, vol. 42, no. 3, pp. 610–618, 2016.
- [21] J. Tian, C. Yuan, L. Yang, C. Wu, G. Liu, and Z. Yang, "The vibration characteristics analysis of pipeline under the action of gas pressure pulsation coupling," *Journal of Failure Analysis and Prevention*, vol. 16, no. 3, pp. 499–505, 2016.
- [22] S. Meng, H. Kajiwara, and W. Zhang, "Internal flow effect on the cross-flow vortex-induced vibration of a cantilevered pipe discharging fluid," *Ocean Engineering*, vol. 137, pp. 120–128, 2017.
- [23] M. Li, J. Gong, Q. P. Li, and L. J. Wang, "Fluid structure interaction vibration of pipes conveying fluid," *Journal of Petrochemical Universities*, vol. 23, no. 1, pp. 60–65, 2010.
- [24] Y. L. Zhou, W. P. Hong, and B. Sun, *Multiphase Hydrodynamics Theory and Its Application*, Science Press, Beijing, China, 1st edition, 2008.
- [25] M. Chen, G.-W. Jiao, Q. W. Yong, and J. Feng, "Study on coupling hydraulic transient model of gas-liquid-solid three-phase flows in the pipelines," *Journal of Logistical Engineering University*, vol. 27, no. 3, pp. 30–34, 2011.
- [26] R. Gomes da Rocha and F. Bastos de Freitas Rachid, "Numerical solution of fluid—structure interaction in piping systems by Glimm's method," *Journal of Fluids and Structures*, vol. 28, no. 1, pp. 392–415, 2012.
- [27] W. S. Zhang, *Finite Difference Methods for Partial Differential Equations in Science Computation*, Higher Education Press, Beijing, China, 1st edition, 2006.
- [28] M. Chen, G.-W. Jiao, S.-S. Deng, and J.-H. Wang, "Flux vector splitting solutions for coupling hydraulic transient of gas-liquid-solid three-phase flow in pipelines," *Applied Mathematics and Mechanics*, vol. 34, no. 7, pp. 811–822, 2013.
- [29] X.-B. Lin, "Generalized Rankine-Hugoniot condition and shock solutions for quasilinear hyperbolic systems," *Journal of Differential Equations*, vol. 168, no. 2, pp. 321–354, 2000.
- [30] R. D. Bao, W. J. Bi, and L. M. Tang, "Acoustic transmitting characteristics in gas-oil two-phase pipeline flowing," *Journal of Shenyang Institute of Chemical Technology*, vol. 22, no. 3, pp. 238–242, 2008.

Research Article

Investigation on the Transition Criterion of Smooth Stratified Flow to Other Flow Patterns for Gas-Hydrate Slurry Flow

Bohui Shi, Jiaqi Wang, Yifan Yu, Lin Ding, Yang Liu, and Haihao Wu

National Engineering Laboratory for Pipeline Safety, MOE Key Laboratory of Petroleum Engineering, Beijing Key Laboratory of Urban Oil and Gas Distribution Technology, China University of Petroleum-Beijing, Changping, Beijing 102249, China

Correspondence should be addressed to Bohui Shi; bh.shi@cup.edu.cn

Received 14 November 2016; Revised 6 February 2017; Accepted 27 March 2017; Published 2 May 2017

Academic Editor: Jerzy Baldyga

Copyright © 2017 Bohui Shi et al. This is an open access article distributed under the Creative Commons Attribution License, which permits unrestricted use, distribution, and reproduction in any medium, provided the original work is properly cited.

A stability criterion for gas-hydrate slurry stratified flow was developed. The model was based on one-dimensional gas-liquid two-fluid model and perturbation method, considering unstable factors including shear stress, gravity, and surface tension. In addition, mass transfer between gas and liquid phase caused by hydrate formation was taken into account by implementing an inward and outward natural gas hydrates growth shell model for water-in-oil emulsion. A series of gas-hydrate slurry flow experiments were carried out in a high-pressure (>10 MPa) horizontal flow loop. The transition criterion of smooth stratified flow to other flow patterns for gas-hydrate slurry flow was established and validated and combined with experimental data at different water cuts. Meanwhile, parameters of this stability criterion were defined. This stability criterion was proved to be efficient for predicting the transition from smooth to nonsmooth stratified flow for gas-hydrate slurry.

1. Introduction

Gas hydrates are ice-like crystals formed by inclosing gas molecules (guests) in clathrates of water molecules (host) under high pressure and low temperature [1]. Gas hydrates are known to cause blockage in oil and gas transportation pipelines [2]. With the tendency of offshore oil industry towards deeper water, gathering systems are confronting unprecedented flow assurance challenges on hydrate formation and plugging. Safety has become an unparalleled problem in offshore oil and gas facilities under undulating terrain condition, especially for high-pressure and low temperature operation conditions owing to the risk of hydrate blockage.

Conventionally, chemical-based injection and insulation are two major techniques to prevent hydrate plugging in offshore production pipelines. However, these two techniques are of high capital expenditure and technical limitations [1, 3]. Recently, hydrate slurry technique has turned out to be a new option to avoid hydrate blocking. In this method, hydrates are not prevented from formation but are made transportable suspending in liquid phase under complex multiphase flow condition [4–9]. Obviously, multiphase flow analysis is an

important factor for implementing hydrate slurry technique in deep water petroleum explorations and developments.

Flow pattern is the key issue in characterizing multiphase flow. There are two generally recognized methods for flow pattern determination: plotting flow pattern map according to the experimental data [10–13] and establishing flow pattern transition criterion based on flow mechanism [14–16]. These two methods have been widely implemented in gas-liquid two-phase flow. However, the flow would be much too complicated, when hydrate forms in the liquid phase.

Though lots of investigations have been made on thermodynamic and kinetic of gas-hydrate formation and decomposition [17–24], study on multiphase flow of gas-hydrate slurry is far from sufficient. Tajima et al. [25] observed CO₂ hydrate slurry flow patterns in CO₂-water two-phase flow using different types of static mixers. Zerpa et al. [26] and Joshi et al. [27] proposed a conceptual model for hydrate plug formation mechanism in water-dominated system, where gas-liquid and liquid-solid flow pattern were defined and characteristics of flow pattern transition with increasing of hydrates volume fraction were studied. Zhao [28] and Gong et al. [7, 8] numerically simulated gas-hydrate slurry stratified

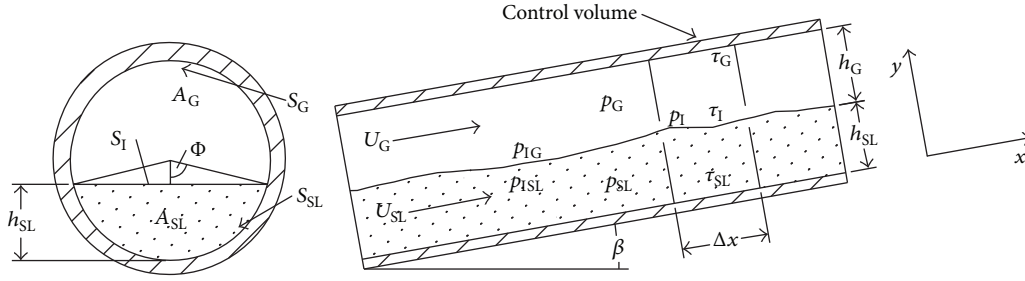


FIGURE 1: Sectional geometry of gas-hydrate slurry stratified flow.

flow, and Kwon et al. [29] simulated the oil-gas-water-hydrate annular-mist flow. Ding et al. [30] reported the difference of the flow patterns with and without hydrates. And, it was concluded that hydrates formation resulted in the decrease of stratified smooth flow area on flow map and less stability of stratified smooth flow. However, little attention has been paid to the flow pattern transition criterion of gas-hydrate slurry flow, especially the stability criterion of stratified flow.

In this paper, gas-hydrate slurry interface stability was analyzed by deriving dispersion function of the interface wave, and then the transition criterion from smooth stratified flow to other flow patterns was obtained. Thereafter, a set of gas-hydrate slurry flow experiments in high-pressure (>10 MPa) horizontal flow loop were carried out to investigate the flow pattern characteristics of gas-hydrate slurry flow. The transition criterion of smooth stratified flow to other flow patterns for gas-hydrate slurry flow was established and validated, combined with experimental data at different water cuts.

2. Model Development

A one-dimensional two-fluid model describing gas-hydrate slurry stratified flow was developed. The schematic description is shown in Figure 1. In this work, the slurry phase was simplified as incompressible. Moreover, work exchange between the fluid and the environment as well as temperature change caused by hydrates formation was ignored.

In Figure 1, h_G and h_{SL} represent the height of gas phase and hydrate slurry phase, A_G and A_{SL} represent the cross section area of gas phase and hydrate slurry phase, U_G and U_{SL} represent velocity of gas phase and hydrate slurry phase, τ_G , τ_{SL} , and τ_I are shear friction at interface of gas phase-pipe wall, hydrate slurry-pipe wall, and gas-hydrate slurry phase, S_G , S_{SL} , and S_I represent wetted perimeter of gas phase, hydrate slurry phase, and gas-hydrate slurry interface, p_G , p_{SL} , and p_I represent pressure of gas phase, hydrate slurry phase, and pressure at the interface, p_{IG} and p_{ISL} represent relative pressure at the interface of gas phase and hydrate slurry phase, β represents angle of inclination, Δx represents distance to the infinitesimal segment, and x and y represent axial and radial direction of the pipe. In addition, the cross section geometry can be found in the supporting

information document in Supplementary Material available online at <https://doi.org/10.1155/2017/9846507> (cross section geometry).

2.1. Flow Analysis

2.1.1. Continuity Equation. For the gas-hydrate slurry stratified flow shown in Figure 1, continuity equation for each phase can be derived as follows:

$$\frac{\partial}{\partial t} (\rho_G A_G) + \frac{\partial}{\partial x} (\rho_G A_G U_G) = \Gamma A, \quad (1a)$$

$$\frac{\partial}{\partial t} (\rho_{SL} A_{SL}) + \frac{\partial}{\partial x} (\rho_{SL} A_{SL} U_{SL}) = -\Gamma A, \quad (1b)$$

where ρ_G and ρ_{SL} are densities of gas and hydrate slurry phase, A represents overall cross section area, and Γ represents mass transfer rate, which is sectional average weight of gas transferred from gas to liquid per second for hydrate formation. The mass transfer rate, Γ , can be estimated using the inward and outward gas-hydrate growth shell model [23], since this model was developed to describe the hydrates formation in water-in-oil emulsion system. The process of hydrates nucleating, forming, and growing as shell covering the water droplets suspended in the continuous liquid phase can be simulated. And, this inward and outward gas-hydrate growth shell model is proved suitable and preferred to be applied in the hydrates slurry flow for the calculation of hydrates fraction and gas consumption. And, the application of this hydrate growth shell model is available in the supporting information (Hydrate Growth Model Implementation).

By introducing slurry phase height h_{SL} , which is a key parameter for stratified flow, (1a) and (1b) can be transformed into (2a) and (2b) as function of h_{SL} .

$$\frac{\partial (\rho_G h_{SL})}{\partial t} - \frac{A_G}{A'_{SL}} \frac{\partial (\rho_G U_G)}{\partial x} + \rho_G U_G \frac{\partial h_{SL}}{\partial x} = -\frac{\Gamma A}{A'_{SL}}, \quad (2a)$$

$$\frac{\partial (\rho_{SL} h_{SL})}{\partial t} + \frac{A_{SL}}{A'_{SL}} \frac{\partial (\rho_{SL} U_{SL})}{\partial x} + \rho_{SL} U_{SL} \frac{\partial h_{SL}}{\partial x} = -\frac{\Gamma A}{A'_{SL}}, \quad (2b)$$

where $A'_{SL} = dA_{SL}/h_{SL}$.

2.1.2. *Momentum Balance Equation.* Momentum balance for each phase can be described as follows:

$$\begin{aligned} & \frac{\partial(\rho_G A_G U_G)}{\partial t} + \frac{\partial(\rho_G A_G U_G^2)}{\partial x} - \Gamma A U_G \\ & = -\tau_G S_G - \tau_I S_I - \rho_G g A_G \sin \beta - A_G \frac{\partial p_{IG}}{\partial x} \\ & - A_G \rho_G g \cos \beta \frac{\partial h_{SL}}{\partial x}, \end{aligned} \quad (3a)$$

$$\begin{aligned} & \frac{\partial(\rho_{SL} A_{SL} U_{SL})}{\partial t} + \frac{\partial(\rho_{SL} A_{SL} U_{SL}^2)}{\partial x} + \Gamma A U_G \\ & = -\tau_{SL} S_{SL} + \tau_I S_I - \rho_{SL} g A_{SL} \sin \beta - A_{SL} \frac{\partial p_{ISL}}{\partial x} \\ & - A_{SL} \rho_{SL} g \cos \beta \frac{\partial h_{SL}}{\partial x}. \end{aligned} \quad (3b)$$

Assuming the interface to be flat in radial direction [31] and ignoring the influence of shorter waves on flow stability [32], the pressure difference at the interface can be approximated as

$$P_{IG} - P_{ISL} = \sigma \frac{\partial^2 h_{SL}}{\partial x^2}, \quad (4)$$

where σ represents interfacial tension and is considered constant in the control volume.

Interfacial shear stress τ_I consists of smooth interface shear stress and instability contribution. The following method, (5a) and (5b), is used in this work [33] to determine interfacial shear stress τ_I , introducing a correlated coefficient C_h

$$\begin{aligned} \tau_I & = f_I \rho_f \frac{(U_G - U_{SL}) |U_G - U_{SL}|}{2} \\ & + \rho_f (U_G - U_{SL})^2 C_h \frac{\partial h_{SL}}{\partial x}, \end{aligned} \quad (5a)$$

$$f_I = \xi_I \left[\left(\frac{S_I}{\pi} \right) \frac{U_f \rho_f}{\mu_f} \right]^{-\eta_I}, \quad (5b)$$

where ρ_f , U_f , and μ_f refer to corresponding density, velocity, and viscosity of the phase with higher velocity and subscript f represents G or SL according to the specific situation. Interfacial friction factor f_I can be calculated after obtaining empirical parameters ξ_I and η_I through experiments.

Substituting (4) and (5a) and (5b) into (3a) and (3b), the key equation of momentum balance relationship can be obtained as follows:

$$\begin{aligned} & \frac{\partial(\rho_G U_G)}{\partial t} - \frac{\partial(\rho_{SL} U_{SL})}{\partial t} + \frac{\partial(\rho_G U_G^2)}{\partial x} - \frac{\partial(\rho_{SL} U_{SL}^2)}{\partial x} \\ & - U_G \Gamma \left(\frac{1}{R_{SL}} + \frac{1}{R_G} \right) + \Pi \frac{\partial h_{SL}}{\partial x} + \sigma \frac{\partial^3 h_{SL}}{\partial x^3} = F, \end{aligned} \quad (6a)$$

$$\Pi = \rho_f (U_G - U_{SL})^2 C_h S_I \left(\frac{1}{A_G} + \frac{1}{A_{SL}} \right) \quad (6b)$$

$$- (\rho_{SL} - \rho_G) g \cos \beta,$$

$$\begin{aligned} F & = \frac{\tau_{SL} S_{SL}}{A_{SL}} - \frac{\tau_G S_G}{A_G} \\ & - f_I \rho_f \frac{(U_G - U_{SL}) |U_G - U_{SL}|}{2} S_I \left(\frac{1}{A_G} + \frac{1}{A_{SL}} \right) \\ & + (\rho_{SL} - \rho_G) g \sin \beta, \end{aligned} \quad (6c)$$

where $R_{SL} = A_{SL}/A$ and $R_G = A_G/A$ refer to liquid holdup and void fraction, respectively. For steady state, $F = 0$, (6a), (6b), and (6c) reduce to steady-state momentum equation.

Gas and hydrate slurry shear stresses at the pipe wall can be expressed as (7a) and (7b) by introducing fanning friction factor.

$$\tau_G = \frac{1}{2} f_G \rho_G U_G |U_G|, \quad (7a)$$

$$\tau_{SL} = \frac{1}{2} f_{SL} \rho_{SL} U_{SL} |U_{SL}|. \quad (7b)$$

For gas phase, the following methods as (8a) and (8b) are applied for friction coefficient f_G .

$$f_G = \frac{16}{Re_G}, \quad \text{laminar flow where } Re_G < 2300, \quad (8a)$$

$$f_G = \frac{0.07725}{[\log(Re_G/7)]^2}, \quad (8b)$$

turbulent flow where $Re_G \geq 2300$.

For hydrate slurry phase, a friction coefficient method, (9) [34], is used, considering the influence of liquid flow as well as hydrate formation and agglomeration.

$$\begin{aligned} f_{SL} & = \left[4 \log \left(\frac{D_{SL}}{2\epsilon_f} \right) + 3.48 \right]^{-2} \\ & + 47 \frac{\rho_H}{\rho_L} \left[\left(\frac{\psi_{\max}}{\psi_h} \right)^{1/3} - 1 \right]^{-2} \left(\frac{d_p}{D_{SL}} \right)^2, \end{aligned} \quad (9)$$

where ρ_H and ρ_L are hydrate and liquid densities, ψ_h and ψ_{\max} are hydrate volume fraction and its maximum value, d_p is hydrate particle diameter, D_{SL} is wetted perimeter diameter of hydrate slurry phase, and ϵ_f is the absolute roughness of the pipe wall.

Substituting (7a) and (7b) into (6c), (10) can be obtained.

$$\begin{aligned} F & = \pm f_{SL} \frac{\rho_{SL} U_{SL}^2}{2} \frac{S_{SL}}{A_{SL}} - f_G \frac{\rho_G U_G^2}{2} \frac{S_G}{A_G} \\ & \mp f_I \frac{\rho_f (U_G - U_{SL})^2}{2} S_I \left(\frac{1}{A_G} + \frac{1}{A_{SL}} \right) \\ & + (\rho_{SL} - \rho_G) g \sin \beta, \end{aligned} \quad (10)$$

where the first term is positive when $U_{SL} > 0$ and third term is negative when $U_G - U_{SL} > 0$, and vice versa [35].

2.2. Stability Analysis

2.2.1. Flow Stability Equation. Referring to the method used in interface stability analysis, where the steady-state contribution and perturbation contribution are separated, U_{SL} , U_G , and h_{SL} can be rewritten as combinations of steady-state part and perturbed part shown in

$$\begin{aligned} U_{SL} &= \bar{U}_{SL} + \hat{U}_{SL}, \\ U_G &= \bar{U}_G + \hat{U}_G, \end{aligned} \quad (11a)$$

$$\begin{aligned} h_{SL} &= \bar{h}_{SL} + \hat{h}_{SL}, \\ \frac{\partial \bar{U}_{SL}}{\partial x} &= \frac{\partial \bar{U}_G}{\partial x} = \frac{\partial \bar{h}_{SL}}{\partial x} = 0, \end{aligned} \quad (11b)$$

$$\begin{aligned} \frac{\hat{U}_{SL}}{\bar{U}_{SL}} &\ll 1, \\ \frac{\hat{U}_G}{\bar{U}_G} &\ll 1, \\ \frac{\hat{h}_{SL}}{\bar{h}_{SL}} &\ll 1. \end{aligned} \quad (11c)$$

Based on (11a), (11b), and (11c), continuous equations (2a) and (2b) and momentum equations (6a), (6b), and (6c) can be linearized and simplified. The following fifth-order linear equation can be obtained to describe one-dimensional steady-state gas-hydrate slurry stratified flow.

$$\begin{aligned} &\sigma \frac{A}{A'_{SL}} \frac{\partial^5 \hat{h}_{SL}}{\partial x^5} + 2 \left[\frac{\bar{\rho}_G \bar{U}_G}{R_G} + \frac{\bar{\rho}_{SL} \bar{U}_{SL}}{R_{SL}} \right] \frac{\partial^3 \hat{h}_{SL}}{\partial t \partial x^2} \\ &+ \left[\frac{\bar{\rho}_G \bar{U}_G^2}{R_G} + \frac{\bar{\rho}_{SL} \bar{U}_{SL}^2}{R_{SL}} + \Pi \frac{A}{A'_{SL}} \right] \frac{\partial^3 \hat{h}_{SL}}{\partial x^3} \\ &+ \left[\frac{\bar{\rho}_G}{R_G} + \frac{\bar{\rho}_{SL}}{R_{SL}} \right] \frac{\partial^3 \hat{h}_{SL}}{\partial t^2 \partial x} - \left[\frac{\Gamma_G}{R_G} \left(\frac{1}{R_{SL}} + \frac{1}{R_G} \right) \right. \\ &\left. - \frac{1}{R_{SL}} \left(\frac{\partial F}{\partial \bar{U}_{SL}} \right)_{h_{SL}, U_G} + \frac{1}{R_G} \left(\frac{\partial F}{\partial \bar{U}_G} \right)_{h_{SL}, U_{SL}} \right] \frac{\partial^2 \hat{h}_{SL}}{\partial t \partial x} \\ &- \left[\frac{\Gamma_G \bar{U}_G}{R_G} \left(\frac{1}{R_{SL}} + \frac{1}{R_G} \right) + \frac{A}{A'_{SL}} \left(\frac{\partial F}{\partial \bar{h}_L} \right)_{U_{SL}, U_G} \right. \\ &\left. - \frac{\bar{U}_{SL}}{R_{SL}} \left(\frac{\partial F}{\partial \bar{U}_{SL}} \right)_{h_{SL}, U_G} + \frac{\bar{U}_G}{R_G} \left(\frac{\partial F}{\partial \bar{U}_G} \right)_{h_{SL}, U_{SL}} \right] \frac{\partial^2 \hat{h}_{SL}}{\partial x^2} \\ &= 0. \end{aligned} \quad (12)$$

Characterize the perturbation of liquid hold-up in exponential form as in the following [36]:

$$\hat{h}_{SL} = \varepsilon e^{i(\omega t - kx)}, \quad (13)$$

where ω , k , and ε are parameters in wave equation.

Substituting (13) into (12), (14a), (14b), (14c), (14d), (14e), (14f), (14g), (14h), (14i), and (14j) can be obtained to describe the stratified smooth flow stability of gas-hydrate slurry stratified flow.

$$\omega^2 - 2(a^*k - ib^*)\omega - d^*k^4 + c^*k^2 - ie^*k = 0, \quad (14a)$$

where following parameters are defined to simplify expression (14a):

$$a^* = \frac{1}{\rho^*} \left[\frac{\bar{\rho}_G \bar{U}_G}{R_G} + \frac{\bar{\rho}_{SL} \bar{U}_{SL}}{R_{SL}} \right], \quad (14b)$$

$$\begin{aligned} b^* &= \frac{1}{2\rho^*} \left[\frac{\Gamma}{R_G} \left(\frac{1}{R_{SL}} + \frac{1}{R_G} \right) - \left(\frac{\partial F}{\partial \bar{U}_{SL,S}} \right)_{R_{SL}, U_{G,S}} \right. \\ &\left. + \left(\frac{\partial F}{\partial \bar{U}_{G,S}} \right)_{R_{SL}, U_{SL,S}} \right], \end{aligned} \quad (14c)$$

$$\begin{aligned} c^* &= \frac{1}{\rho^*} \left\{ \frac{\bar{\rho}_G \bar{U}_G^2}{R_G} + \frac{\bar{\rho}_{SL} \bar{U}_{SL}^2}{R_{SL}} \right. \\ &+ \frac{1}{A'_{SL}} \left[\rho_f (U_G - U_{SL})^2 C_{hS1} \left(\frac{1}{R_G} + \frac{1}{R_{SL}} \right) \right. \\ &\left. \left. - A(\rho_{SL} - \rho_G) g \cos \beta \right] \right\}, \end{aligned} \quad (14d)$$

$$d^* = \frac{\sigma}{\rho^*} \frac{A}{A'_{SL}}, \quad (14e)$$

$$e^* = \frac{1}{\rho^*} \left[\frac{\Gamma_G \bar{U}_G}{R_G} \left(\frac{1}{R_{SL}} + \frac{1}{R_G} \right) + \left(\frac{\partial F}{\partial \bar{R}_L} \right)_{U_{SL}, U_G} \right], \quad (14f)$$

$$\rho^* = \frac{\bar{\rho}_G}{R_G} + \frac{\bar{\rho}_{SL}}{R_{SL}}, \quad (14g)$$

$$\left(\frac{\partial F}{\partial \bar{U}_{SL,S}} \right)_{R_{SL}, U_{G,S}} = \frac{1}{R_{SL}} \left(\frac{\partial F}{\partial \bar{U}_{SL}} \right)_{h_{SL}, U_G}, \quad (14h)$$

$$\left(\frac{\partial F}{\partial \bar{U}_{G,S}} \right)_{R_{SL}, U_{SL,S}} = \frac{1}{R_G} \left(\frac{\partial F}{\partial \bar{U}_G} \right)_{h_{SL}, U_{SL}}, \quad (14i)$$

$$\left(\frac{\partial F}{\partial \bar{R}_L} \right)_{U_{SL,S}, U_{G,S}} = \frac{A}{A'_{SL}} \left(\frac{\partial F}{\partial \bar{h}_L} \right)_{U_{SL}, U_G} \quad (14j)$$

$$- \frac{\bar{U}_{SL}}{R_{SL}} \left(\frac{\partial F}{\partial \bar{U}_{SL}} \right)_{h_{SL}, U_G} + \frac{\bar{U}_G}{R_G} \left(\frac{\partial F}{\partial \bar{U}_G} \right)_{h_{SL}, U_{SL}}.$$

2.2.2. *Stability Criterion.* Analytically solve quadratic equations (14a), (14b), (14c), (14d), (14e), (14f), (14g), (14h), (14i), and (14j), and roots can be expressed as follows:

$$w = (a^*k - ib^*) \pm \sqrt{(a^{*2} - c^*)k^2 - b^{*2} + d^*k^4 + i(e^*k - 2a^*b^*k)}. \quad (15)$$

Substituting $w = w_R + w_I$, (14a) can be split into imaginary part and real part as follows:

Imaginary part:

$$-2a^*kw_I + 2b^*w_R - e^*k + 2w_Rw_I = 0 \quad (16a)$$

Real part:

$$w_R^2 - 2a^*kw_R - d^*k^4 + c^*k^2 - 2b^*w_I - w_I^2 = 0 \quad (16b)$$

It could be found in (16a) and (16b) that if $w_I < 0$, perturbation contribution of liquid holdup increases exponentially with time, resulting in flow instability. With w_I approaching zero, stability criterion for gas-hydrate slurry stratified smooth flow can be derived as follows:

$$\left(\frac{e^*}{2b^*} - a^*\right)^2 - (a^{*2} - c^*) - d^*k^2 < 0. \quad (17)$$

Analyzing (17), two critical wave velocities at the inception of instability are introduced as (18a) and (18b). C_V is the critical wave velocity considering the viscous effect, while C_{IV} is the one without the influence of viscosity [33, 37, 38].

$$C_V = \frac{w_R}{k} = \frac{e^*}{2b^*} = \frac{(\Gamma\bar{U}_G/R_G)(1/R_{SL} + 1/R_G) + (\partial F/\partial \bar{R}_L)_{U_{SL}, U_G}}{(\Gamma/R_G)(1/R_{SL} + 1/R_G) - (\partial F/\partial \bar{U}_{SL,S})_{R_{SL}, U_{G,S}} + (\partial F/\partial \bar{U}_{G,S})_{R_{SL}, U_{SL,S}}}, \quad (18a)$$

$$C_{IV} = a^* = \frac{\bar{\rho}_G\bar{U}_GR_{SL} + \bar{\rho}_{SL}\bar{U}_{SL}R_G}{\bar{\rho}_GR_{SL} + \bar{\rho}_{SL}R_G}. \quad (18b)$$

Substituting (14a), (14b), (14c), (14d), (14e), (14f), (14g), (14h), (14i), and (14j) and (18a) and (18b) into (17), the stability criterion for gas-hydrate slurry stratified smooth flow can be obtained as follows:

$$\begin{aligned} (C_V - C_{IV})^2 + \frac{\bar{\rho}_G\bar{\rho}_{SL}}{\rho^{*2}R_G R_{SL}} (\bar{U}_G - \bar{U}_{SL})^2 \\ - \frac{\bar{\rho}_{SL} - \bar{\rho}_G}{\rho^*} g \cos \beta \frac{A}{S_I} - \frac{\sigma}{\rho^*} \frac{A}{S_I} k^2 \\ + \frac{\rho_f (U_G - U_{SL})^2 C_h}{\rho^*} \left(\frac{1}{R_G} + \frac{1}{R_{SL}} \right) < 0. \end{aligned} \quad (19)$$

In (19), the first term corresponds to the viscous shear stress that amplifies any disturbance on the surface; the second and third terms are stability criterion disregarding viscous effects, also known as the one-dimensional interface IKH instability criterion; the fourth term stands for the surface tension contribution and depends mainly on wave variable k ; the last term amplifies instability brought by other factors and is independent of the direction of relative velocity as well as shear stress between the two phases.

Neglecting interfacial tension, viscous shear stress, and interface shear stress, (20) can be simplified.

$$\begin{aligned} (\bar{U}_G - \bar{U}_{SL}) \\ < \left(\frac{\bar{\rho}_GR_{SL} + \bar{\rho}_{SL}R_G}{\bar{\rho}_{SL}} \frac{\bar{\rho}_L - \bar{\rho}_G}{\bar{\rho}_G} g \cos \beta \frac{A}{S_I} \right)^{0.5}. \end{aligned} \quad (20)$$

Considering the large density difference between gas and hydrate slurry phases, (20) can be further simplified as follows, shown in (21). This equation matches the criterion presented by Taitel and Dukler [14] in 1976.

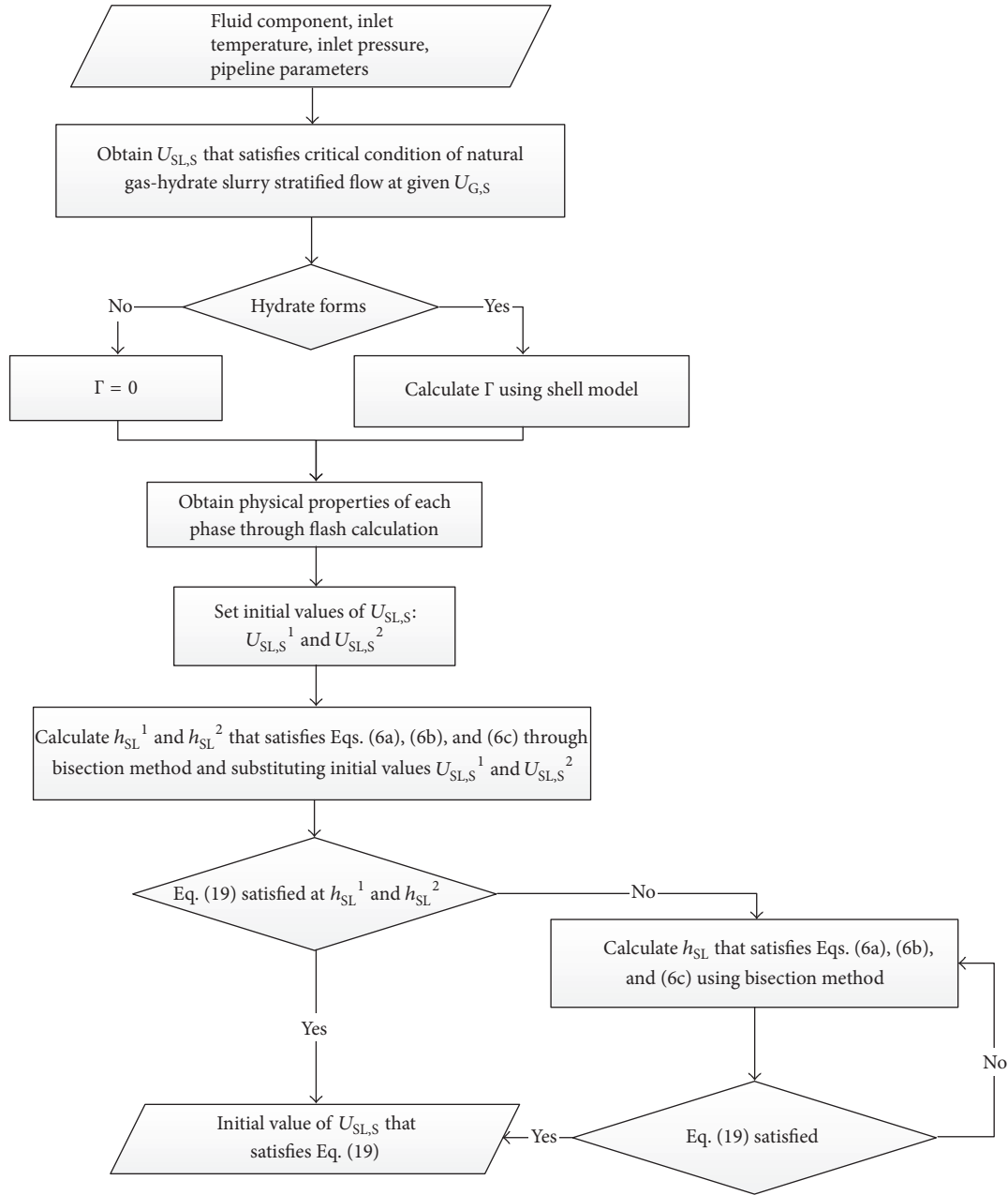
$$(\bar{U}_G - \bar{U}_{SL}) < \left(\frac{\bar{\rho}_L - \bar{\rho}_G}{\bar{\rho}_G} g \cos \beta \frac{A_G}{S_I} \right)^{0.5}. \quad (21)$$

Calculation procedure based on the criterion is presented in Scheme 1. For stratified flow boundary determination, superficial velocity of one phase can be calculated when that of the other phase is given. In implanting this model, bisection method is applied in the iteration calculation. Scheme 1 shows the flowchart to calculate liquid superficial velocity $U_{SL,S}$ at a given gas superficial velocity $U_{G,S}$, while $U_{G,S}$ at given $U_{SL,S}$ can be obtained through similar procedure.

3. Experiments

To analyze stability transition criterion for stratified smooth flow using (19), parameters including ξ_I , η_I , C_h , and k need to be determined. In this paper, these parameters were obtained based on the experiments at different water cuts using high-pressure hydrates slurry flow loop.

3.1. *Material and Facility.* A double-pass high-pressure horizontal flow loop shown in Figure 2 was designed and established in China University of Petroleum, Beijing, supported by CNOOC [24, 39–42]. This flow loop is 30 m long, with inner diameter of 1 inch and pressure exceeding 10 MPa. Test section temperature can be maintained from



SCHEME 1: Algorithm to determine the stratified flow boundary by calculating liquid superficial velocity $U_{SL,S}$ at a given gas superficial velocity $U_{G,S}$.

-20°C to 80°C by circulating water-glycol blend with the countercurrent flowing surrounding it in a 2-inch jacket. Fluid inside the loop can be observed through high-pressure windows at two different locations. Gas and liquid can be injected separately by a plunge compressor ($2200\text{ m}^3/\text{h}$) and a magnetic centrifugal pump ($12.0\text{ m}^3/\text{h}$). Gas is injected at the inlet of the test section. At the outlet of the test section, gas and liquid flow into an insulated separator and are redirected towards the test section after pressurization.

Thermocouples are placed along the pipe, inside the separator, inside the water-glycol system, and on different gas utilities. A Coriolis flow meter is stalled to measure liquid

mixture density and flow rate. Two FM1000 gamma ray densitometers are available to measure the mean density of the multiphase fluid. Differential pressure sensors are installed to follow the evolution of pressure. Rapid data acquisition system permits the detection of quickly occurring events. A Focused Beam Reflectance Measurements (FBRM) probe and Particle Video Microscope (PVM) are installed to capture the evolution of the droplets, bubbles, or solid particles in fluid.

Deionized water, civil natural gas, and $-20\#$ diesel (compositions listed in Table 1) were used for the experiments. The dosage of added antiagglomerate was 3 wt% (measuring error $\pm 0.01\text{ g}$) to prevent the hydrate crystals from aggregating [43].

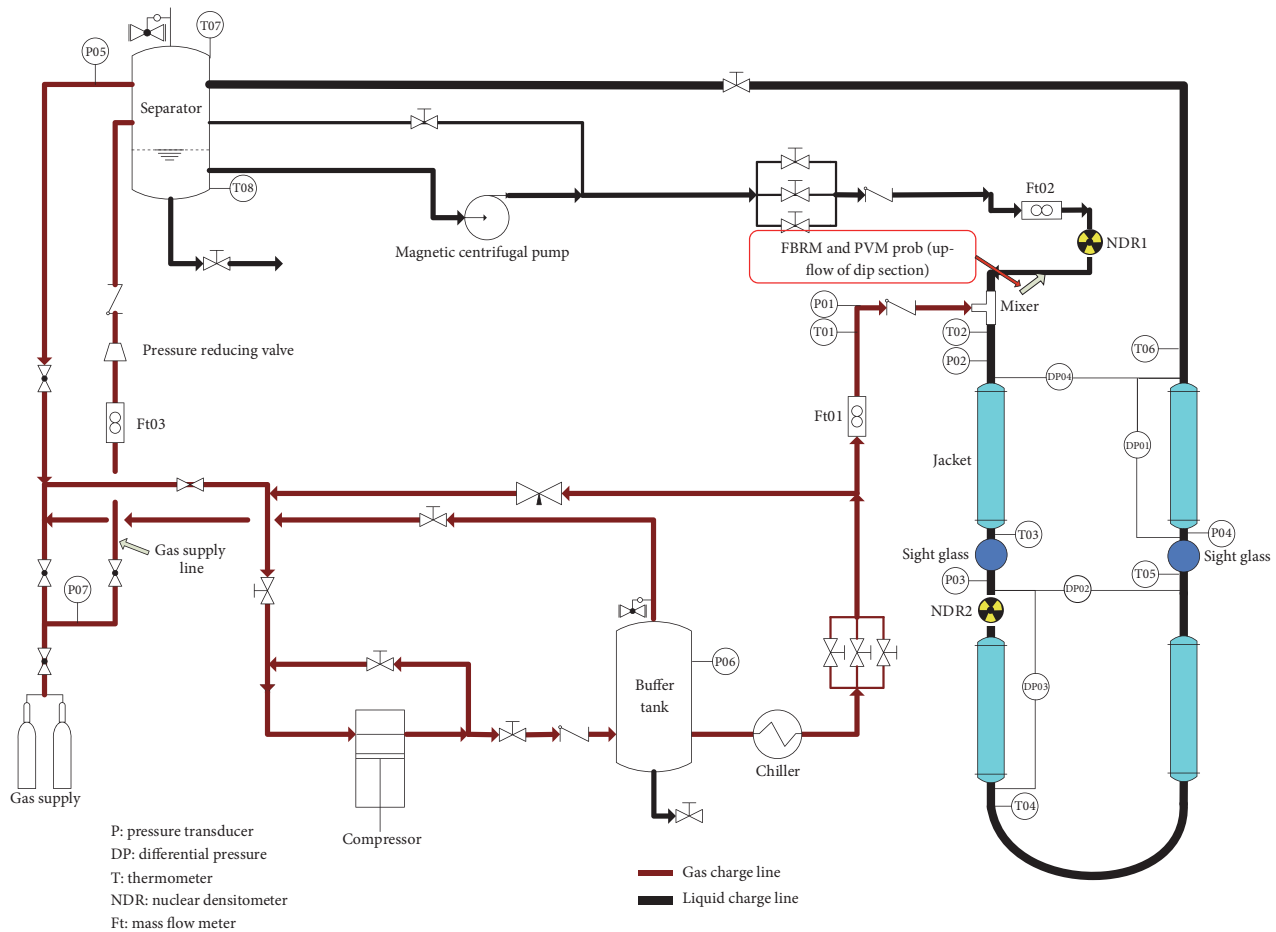


FIGURE 2: Sketch of high-pressure hydrate flow loop.

3.2. Experiment Procedure. Four groups of experiments at different water cuts (15%, 20%, 25%, and 30%) were carried out with gas, -20# diesel oil, and deionized water. Experimental conditions are listed in Table 2. Specific experimental procedure is detailed as follows:

- (1) Vacuum the experimental system one hour before injecting the required amount of -20# diesel oil, deionized water, and antiagglomerates.
- (2) Start and set the temperature controller at 18°C, the magnetic centrifugal pump at 40 Hz, and the control valve at 100%, get the liquid phase well circulated for least 5 hours to form water-in-oil emulsion, and then open FBRM to monitor changes of the particles in the fluid.
- (3) Open the gas injection valve and pressure the system up to experimental set point, after the temperature of the system stays constant at 18°C and particles size observed using FBRM becomes stable.
- (4) Set the system temperature to experimental set point and cool the flow loop; hydrate would form as the temperature drops below the hydrate equilibrium temperature at the system pressure.
- (5) Maintain temperature and pressure at experimental set point for at least 5 hours to ensure the fully hydrate formation, adjust compressor inlet valve and pump speed to attain a gas flow rate within 20~195 kg/h and liquid flow rate within 75~860 kg/h, and then observe the flow pattern and record the data; for each data point presented in this work, flow rate of both gas and slurry phase were controlled and flow pattern was observed when the flow rates, pressure, and temperature were stabilized.
- (6) Increase the system temperature, stop the compressor and pump, evacuate the residual gas, discharge the experiment liquid, clean and flush the flow loop with compressed air, and replace it with nitrogen.
- (7) Repeat the procedure at different water cuts.

4. Results and Discussions

4.1. Experiment Results. In the experiments, 293 smooth and nonsmooth stratified flow pattern data points at different water cuts were obtained under steady-state conditions (Tables S.1-S.4), which was visually observed through the sight glass of the loop. Four types of flow patterns were found,

TABLE 1: Compositions of civil natural gas and -20# diesel oil.

Comp	Mol%
Civil natural gas	
N ₂	1.5603
CO	2.0911
CO ₂	0.9129
C ₁	90.6061
C ₂	3.1207
C ₃	3.1207
iC ₄	0.3291
iC ₅	0.0425
nC ₆₊	0.0106
-20# diesel oil	
C ₁₁	0.8863
C ₁₂	3.3586
C ₁₃	5.3886
C ₁₄	6.1990
C ₁₅	6.7780
C ₁₆	6.8310
C ₁₇	7.9890
C ₁₈	7.4618
C ₁₉	6.3752
C ₂₀₊	48.7325

TABLE 2: Experimental conditions of gas-hydrate slurry flow.

Water cut (%)	P (MPa)	T (K)	V _L (m ³)	N _{exp} [*] (-)
15	4.13	277.33	0.0777	34
20	4.26	279.82	0.0875	75
25	3.85	278.99	0.0933	96
30	4.20	278.99	0.1000	88

* N_{exp}: number of experimental data points.

including two typical flow patterns (stratified smooth flow and slug flow) and two transitional flow patterns (stratified wavy flow and short slug flow). Distinct gas-liquid interface can be observed, and the interface was flat for the stratified smooth flow (Figure 3(a)) and was wavy for stratified wave flow (Figure 3(b)). A liquid film zone and a liquid slug were found intermittently for slug flow (Figure 4), while a relatively longer liquid film and shorter slug length were found for short slug flow.

The morphologies, sizes, and distributions of fully formed hydrate particles in the slurry were recorded by PVM as shown in Figure 5. The chord length distribution before and after hydrates formation is displayed in Figure 6. According to experimental observations, it can be concluded that hydrates particles form as shells covering water droplets in the water-in-oil emulsion, and the size of hydrates particles will be enlarged compared with water droplet. In addition, hydrate particle morphologies, sizes, and distributions

showed no distinguishable difference at different flow patterns, implying that their influences on flow pattern transition were not significant.

4.2. Model Implementation. Based on experimental conditions listed in Table 2, hydrate growth parameters and gas consumption rate at different water cuts were calculated using the inward and outward hydrate growth shell model [23]. Results presented in Table 3 showed that gas consumption rate increased with water cut. Detailed calculation procedure including water consumption and hydrate fraction is presented in the supporting information (Hydrate Growth Model Implementation). Gas-slurry stratified smooth flow region transition boundary at different water cuts was obtained by implementing the calculation procedure presented in Scheme 1. Parameters in the model are obtained, where ξ_1 is 0.01, η_1 is -0.2, C_h is 0.01, and k is 10.

4.3. Model Evaluation. To compare the transition criterion of smooth stratified flow to other flow patterns for gas-hydrate slurry flow developed in this work with the classical flow pattern distribution models, flow region boundaries calculated using this model as well as that calculated using Taitel-Dukler [14] and Mandhane [13] methods are presented in Figure 7.

As is shown in Figure 7, Mandhane's model can roughly divide stratified flow from nonstratified flow at four water cuts, yet the results lead to a larger smooth stratified flow region. Taitel-Dukler model cannot give a satisfying stratified flow transition boundary, due to not considering the effect of hydrate formation on flow stability. Transition boundaries obtained based on the model developed in this work show good agreement with experimental data.

All data points are summarized in Figure 8. It can be seen that no distinctive effect of water cut on flow pattern division is observed, though gas consumption rate differs evidently according to Table 3. This may be due to the similar water consumption rates and hydrate fractions as shown in Figure 9. As calculated flow pattern boundary is primarily affected by fluid viscosity, and hydrate slurry viscosity is further determined by hydrate volume fraction, proximal transition lines are obtained under similar hydrate fraction though at different water cuts.

The pattern experiment data of gas-hydrate slurry multiphase flow pattern in this work are not effectively enough to obtain more precise correlation parameters or investigate the flow pattern transition mechanism deeply. More experimental and theoretical research should be carried out in the future. Nevertheless, the good agreement with experimental data proved this work to be both feasible and significant.

5. Conclusion

In this work, a one-dimension two-fluid model for gas-hydrate slurry stratified flow was developed based on perturbation method, and a stability criterion for smooth stratified flow was proposed. In establishing the criterion, mass transfer between gas and slurry phase caused by hydrate formation

TABLE 3: Hydrate growth parameters of different water cuts and gas consumed rate.

Water cut %	$K^* \times 10^{-7}$ mol/(m ² ·Mpa·s)	$D_f^0 \times 10^{-9}$ m ² /s	ξ	$\epsilon_H^0 \times 10^{-32}$ m ³	ζ	$\Gamma_G \times 10^{-4}$ kg/m ³ ·s
15	4.364	1.149	1.489	14.66	0.2527	7.188
20	7.606	13.82	1.527	6.339	0.2679	9.575
25	8.980	30.62	1.546	4.891	0.2767	11.72
30	16.16	321.5	1.564	2.994	0.2820	13.88

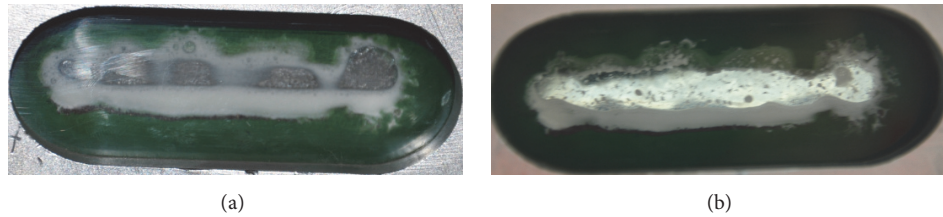


FIGURE 3: Photos of stratified flow: (a) stratified smooth flow and (b) stratified wave flow.

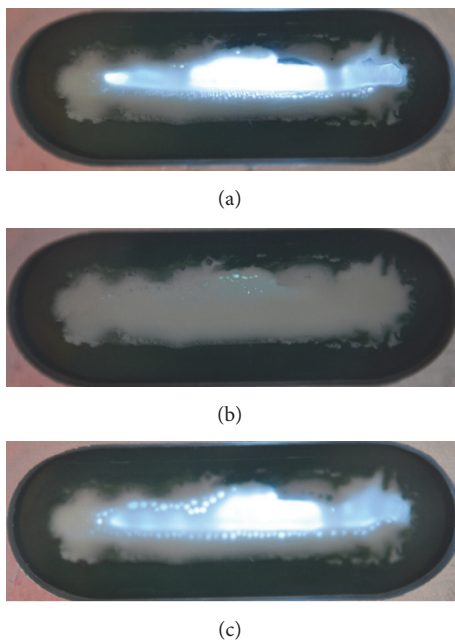


FIGURE 4: Photos of slug flow: (a) liquid film zone before liquid slug, (b) liquid slug, and (c) liquid film zone after liquid slug.

was considered, and various mathematical techniques were applied in linearizing the equation sets. As the formation of hydrate would evidently complicate the flow, the influences of shear stress, gravity, surface tension, hydrate formation, and other unstable factors were considered. Compared with the classical two-phase gas-liquid stratified flow stability criteria proposed by Taitel-Dukler [14] and Mandhane [13], transition boundary based on this study showed better agreement with experiment results.

Groups of gas-hydrate slurry multiphase flow experiments were carried out on a most advanced high-pressure

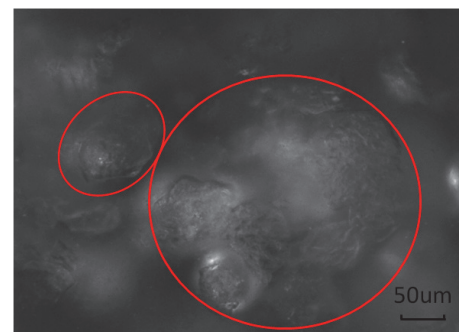


FIGURE 5: Hydrate particles (marked in the red circles) in gas-liquid multiphase system.

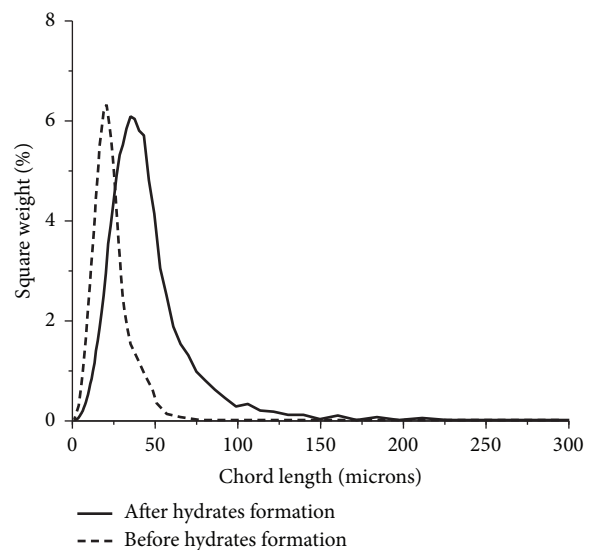


FIGURE 6: Chord length distribution before and after hydrates formation.

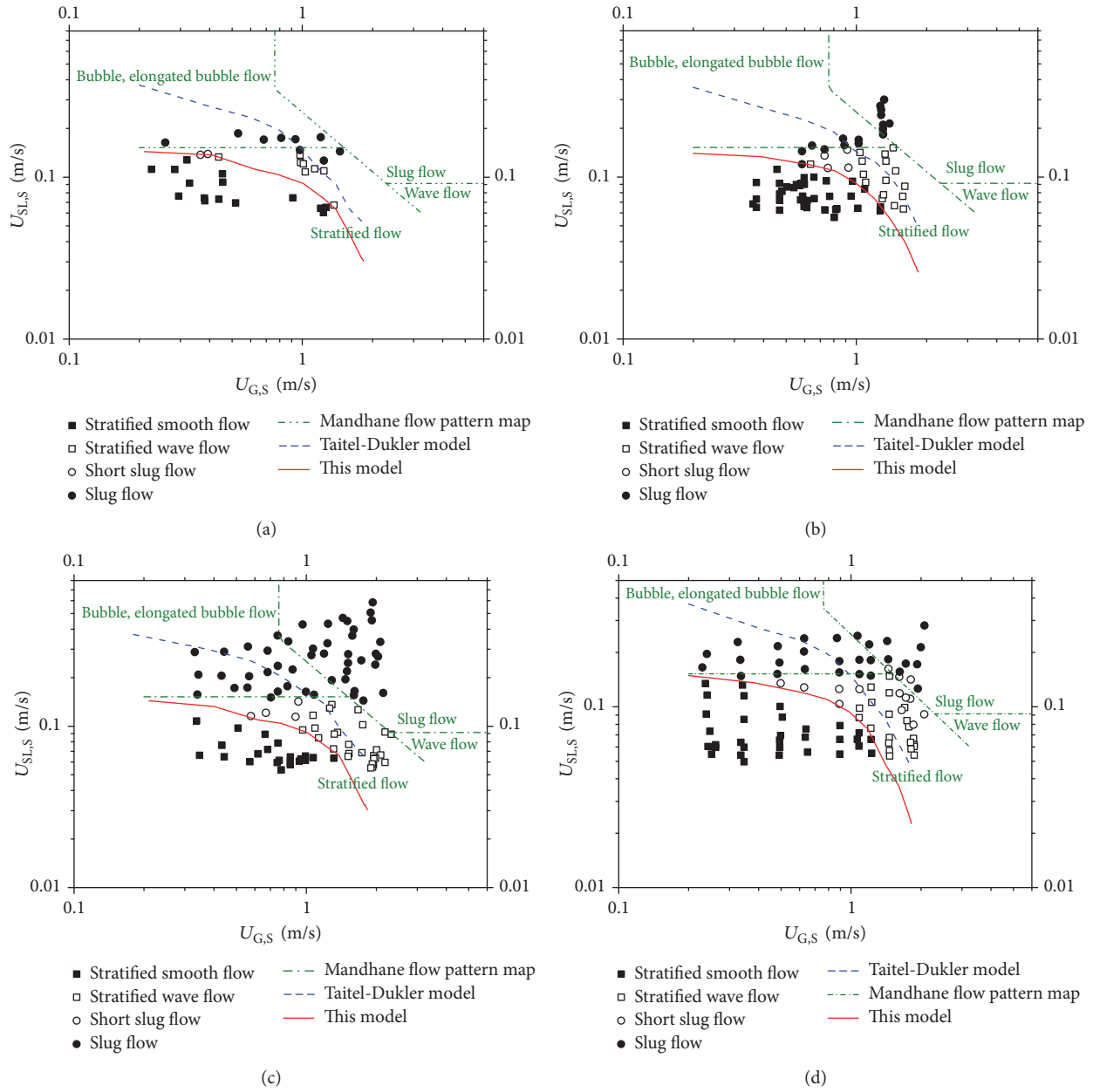


FIGURE 7: Flow pattern map and boundary for stratified flow of gas-slurry flow at different water cuts: (a) 15%, (b) 20%, (c) 25%, and (d) 30%.

(>10 MPa) hydrate slurry flow loop in China, and 293 experimental data points of both smooth and nonsmooth stratified flow were obtained. Model parameters were generated in combining the experiment data with the gas-hydrate slurry stratified flow stability creation developed in this work, and the model was proved applicable in gas-hydrate slurry multi-phase flow numerical simulation and characteristic study.

Nomenclature

A : Cross area of the pipeline, m^2
 A_G : Cross area of gas phase, m^2
 A_{SL} : Cross area of hydrate slurry phase, m^2

C_V : Viscosity critical wave velocity at the inception of instability, $m s^{-1}$
 C_{IV} : Nonviscosity critical wave velocity at the inception of instability, $m s^{-1}$
 C_h : Correlated coefficient
 d_p : Diameter of hydrates particle, m
 D_{SL} : Diameter of the wetted perimeter of hydrate slurry phase, m
 f_I : Friction coefficient of interface gas-slurry phase
 f_G : Friction coefficient of interface gas phase at pipe wall
 f_{SL} : Friction coefficient of interface slurry at pipe wall
 h_G : Height of gas phase, m
 h_{SL} : Height of hydrate slurry phase, m

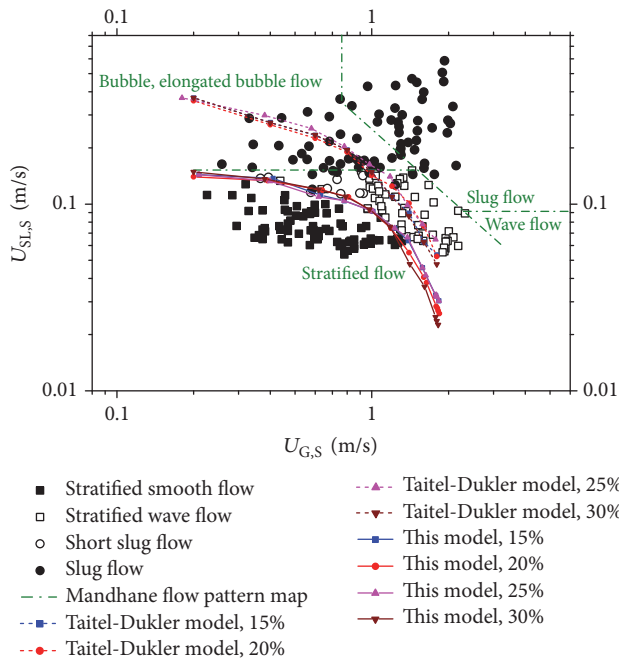


FIGURE 8: Flow pattern distribution for gas-slurry stratified flow at different water cuts.

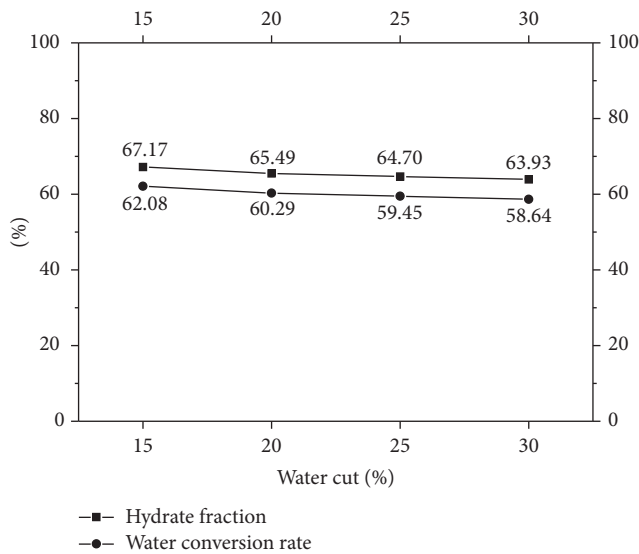


FIGURE 9: Hydrate fraction and water conversion rate at different water cuts.

k : Parameter in wave equation
 p_G : Pressure of gas phase
 p_{SL} : Pressure of hydrate slurry phase
 p_I : Pressure at the interface
 p_{IG} : Relative pressure at the interface of gas phase
 p_{ISL} : Relative pressure at the interface of hydrate slurry phase
 R_G : Gas phase fraction of pipe cross area
 R_{SL} : Hydrate slurry phase fraction of pipe cross area
 Re_G : Reynolds number of gas phase

S_G : Wetted perimeter of gas phase, m
 S_I : Wetted perimeter of interface gas-slurry phase, m
 S_{SL} : Wetted perimeter of hydrate slurry phase, m
 t : Time, s
 U_G : Velocity of gas phase, $m \cdot s^{-1}$
 U_{SL} : Velocity of hydrate slurry phase, $m \cdot s^{-1}$
 w : Parameter in wave equation
 x : Axial direction of the pipe, m
 Δx : Distance to the infinitesimal segment, m
 y : Radial direction of the pipe, m
 ρ_H : Density of hydrates, $kg \cdot m^{-3}$
 ρ_L : Density of oil phase, $kg \cdot m^{-3}$
 ψ_h : Hydrate volume fraction
 ψ_{max} : Maximum hydrate volume fraction
 Γ : Mass transfer rate between gas phase and hydrate slurry phase, $kg \cdot s^{-1} \cdot m^{-3}$
 β : Angle of inclination, rad
 σ : Interfacial tension, N/m
 ρ_G : Density of gas phase, $kg \cdot m^{-3}$
 ρ_{SL} : Density of hydrate slurry phase, $kg \cdot m^{-3}$
 ρ_f : Density of faster phase: subscript f represents the faster phase, $kg \cdot m^{-3}$
 τ_G : Shear friction of interface gas phase at pipe wall, N
 τ_I : Shear friction of interface of gas-slurry phase, N
 τ_{SL} : Shear friction of interface of slurry at pipe wall, N
 ε_f : Absolute roughness of the pipe wall, m
 ξ_I : Friction calculated empirical parameter
 η_I : Friction calculated empirical parameter
 ε : Parameter in wave equation.

Conflicts of Interest

The authors declare that they have no conflicts of interest.

Acknowledgments

This work was supported by the National Natural Science Foundation of China (51306208, 51534007, and 51274218), National Science and Technology Major Project of China (2016ZX05028004-001), National Key Research and Development Plan of China (SQ2016YFSF010222), and Science Foundation of China University of Petroleum-Beijing (2462015YQ0404 and 201602), which are gratefully acknowledged.

References

- [1] E. Dendy Sloan and C. A. Koh, *Clathrate Hydrates of Natural Gas*, Crc Press, 2008.
- [2] E. G. Hammerschmidt, "Formation of gas hydrates in natural gas transmission lines," *Industrial & Engineering Chemistry*, vol. 26, no. 8, pp. 851–855, 1934.
- [3] D. Sloan et al., *Natural Gas Hydrates in Flow Assurance*, 2010.
- [4] Y. Peysson, "Collision process between particles in the transport of dispersed hydrates in production lines," in *Proceedings of the 5th International Conference on Gas Hydrate*, Houston, Tex, USA, 2005.

- [5] O. C. Hernandez, *Investigation of Hydrate Slurry Flow in Horizontal Pipelines*, 2006.
- [6] E. Dellecase, G. Geraci, L. Barrios, D. Estanga, R. Domingues, and M. Volk, *Hydrate plugging or slurry flow: Effect of key variables*, 2008.
- [7] J. Gong, B. Shi, and J. Zhao, "Natural gas hydrate shell model in gas-slurry pipeline flow," *Journal of Natural Gas Chemistry*, vol. 19, no. 3, pp. 261–266, 2010.
- [8] J. Gong, B. Shi, and W. Wang, "Numerical study the flow characteristics of gas-hydrate slurry two phase stratified flow," in *Proceeding of the 7th International Conference on Multiphase Flow*, Tampa, Fla, USA, 2010.
- [9] M. Gainville, A. Sinquin, and M. Darbouret, *Hydrate Slurry Characterisation for Laminar and Turbulent Flows in Pipelines*, 2011.
- [10] O. Baker, "Simultaneous flow of oil and gas," *Oil & Gas Journal*, vol. 53, p. 185, 1954.
- [11] H. Duns and N. C. Ros, *Vertical Flow of Gas and Liquid Mixtures in Wells*, 1963.
- [12] G. W. Govier, K. Aziz, and W. R. Schowalter, *The Flow of Complex Mixtures in Pipes*, Van Nostrand Reinhold Co., 1972.
- [13] J. M. Mandhane, G. A. Gregory, and K. Aziz, "A flow pattern map for gas—liquid flow in horizontal pipes," *International Journal of Multiphase Flow*, vol. 1, no. 4, pp. 537–553, 1974.
- [14] Y. Taitel and A. E. Dukler, "A model for predicting flow regime transitions in horizontal and near horizontal gas-liquid flow," *AIChE Journal*, vol. 22, no. 1, pp. 47–55, 1976.
- [15] Y. Taitel, D. Bornea, and A. E. Dukler, "Modelling flow pattern transitions for steady upward gas-liquid flow in vertical tubes," *AIChE Journal*, vol. 26, no. 3, pp. 345–354, 1980.
- [16] D. Barnea, "A unified model for predicting flow-pattern transitions for the whole range of pipe inclinations," *International Journal of Multiphase Flow*, vol. 13, no. 1, pp. 1–12, 1987.
- [17] A. L. Ballard and E. D. Sloan Jr., "The next generation of hydrate prediction: part III. Gibbs energy minimization formalism," *Fluid Phase Equilibria*, vol. 218, no. 1, pp. 15–31, 2004.
- [18] L. Ballard and E. D. Sloan Jr., "The next generation of hydrate prediction IV: a comparison of available hydrate prediction programs," *Fluid Phase Equilibria*, vol. 216, no. 2, pp. 257–270, 2004.
- [19] G.-J. Chen and T.-M. Guo, "A new approach to gas hydrate modelling," *Chemical Engineering Journal*, vol. 71, no. 2, pp. 145–151, 1998.
- [20] P. D. Dholabhai, P. Englezos, and N. Kalogerakis, *Kinetics of formation of methane and ethane gas hydrates*, 1987.
- [21] P. Englezos et al., "Kinetics of gas hydrate formation from mixtures of methane and ethane," *Chemical Engineering Science*, vol. 42, no. 11, pp. 2659–2666, 1987.
- [22] H. C. Kim, P. R. Bishnoi, R. A. Heidemann, and S. S. H. Rizvi, "Kinetics of methane hydrate decomposition," *Chemical Engineering Science*, vol. 42, no. 7, pp. 1645–1653, 1987.
- [23] B.-H. Shi, J. Gong, C.-Y. Sun, J.-K. Zhao, Y. Ding, and G.-J. Chen, "An inward and outward natural gas hydrates growth shell model considering intrinsic kinetics, mass and heat transfer," *Chemical Engineering Journal*, vol. 171, no. 3, pp. 1308–1316, 2011.
- [24] X.-S. Li and Y. Zhang, "Study on dissociation behaviors of methane hydrate in porous media based on experiments and fractional dimension shrinking-core model," *Industrial and Engineering Chemistry Research*, vol. 50, no. 13, pp. 13–17, 2011.
- [25] H. Tajima, A. Yamasaki, and F. Kiyono, "Effects of mixing functions of static mixers on the formation of CO₂ hydrate from the two-phase flow of liquid CO₂ and water," *Energy and Fuels*, vol. 19, no. 6, pp. 2364–2370, 2005.
- [26] L. E. Zerpa et al., "Overview of Csmhyk: a Transient Hydrate Formation Model Developed Over a Decade of Hydrate Research," 2011.
- [27] S. Joshi, I. Rao, L. Zerpa et al., "Understanding hydrate plug formation from high water cut systems with a four inch flowloop," in *Proceedings of the 7th International Conference on Gas Hydrates (ICGH '11)*, Edinburgh, UK, July 2011.
- [28] J. Zhao, "Study on flow properties of hydrate slurry in multiphase pipeline," in *Oil and Gas Storage and Transportation*, China University of Petroleum, Beijing, China, 2009.
- [29] O. Kwon, S. Ryou, and W. Sung, "Numerical modeling study for the analysis of transient flow characteristics of gas, oil, water, and hydrate flow through a pipeline," *Korean Journal of Chemical Engineering*, vol. 18, no. 1, pp. 88–93, 2001.
- [30] L. Ding, B. Shi, X. Lv et al., "Investigation of natural gas hydrate slurry flow properties and flow patterns using a high pressure flow loop," *Chemical Engineering Science*, vol. 146, pp. 199–206, 2016.
- [31] P. Becher, *Principles of Colloid and Surface Chemistry*, Dekker, 1977.
- [32] D. Barnea and Y. Taitel, "Non-linear interfacial instability of separated flow," *Chemical Engineering Science*, vol. 49, no. 14, pp. 2341–2349, 1994.
- [33] N. Brauner and D. M. Maron, "Stability of two-phase stratified flow as controlled by laminar/turbulent transition," *International Communications in Heat and Mass Transfer*, vol. 21, no. 1, pp. 65–74, 1994.
- [34] P. Yannick et al., *Flow of Hydrates Dispersed in Production Lines*, 2003.
- [35] D. Deng, "Simulation study on natural gas-gas condensate flow characteristics in multiphase transportation pipeline," in *Oil and Gas Storage and Transportation*, China University of Petroleum, Beijing, China, 2005.
- [36] P. Drazin and W. Reid, "Hydrodynamic stability," *Journal of Fluid Mechanics*, vol. 124, 1981.
- [37] D. Barnea, "On the effect of viscosity on stability of stratified gas—liquid flow—application to flow pattern transition at various pipe inclinations," *Chemical Engineering Science*, vol. 46, no. 8, pp. 2123–2131, 1991.
- [38] D. Barnea and Y. Taitel, "Kelvin-Helmholtz stability criteria for stratified flow: viscous versus non-viscous (inviscid) approaches," *International Journal of Multiphase Flow*, vol. 19, no. 4, pp. 639–649, 1993.
- [39] W. Li, "Experimental study on multiphase flow mechanism of hydrate slurry in pipes," in *Oil and Gas Storage and Transportation Engineering*, China University of Petroleum, Beijing, China, 2012.
- [40] X. Lv et al., "Experimental study on natural gas hydrate slurry flow," *Spe Journal*, vol. 2, no. 2, pp. 199–216, 2012.
- [41] X. Lv, D. Yu, W. Li, B. Shi, and J. Gong, "Experimental study on blockage of gas hydrate slurry in a flow loop," in *Proceeding of the 9th International Pipeline Conference (IPC '12)*, pp. 37–43, 2012.

- [42] X. Lv, J. Gong, W. Li, Y. Tang, and J. Zhao, "Focused-beam reflectance method aids hydrate blockage prediction," *Oil and Gas Journal*, vol. 111, no. 1, pp. 99–107, 2013.
- [43] C. Y. Sun et al., "The experimental evaluation for controlling hydrate plug in oil-gas-water multiphase pipeline," in *Proceeding of the 2nd Chinese National Chemical and Biochemical Engineering Annual Meeting*, Beijing, China, 2005.

Research Article

Coalbed Methane Production System Simulation and Deliverability Forecasting: Coupled Surface Network/Wellbore/Reservoir Calculation

Jun Zhou,¹ Guangchuan Liang,¹ Tao Deng,² Shiwei Zhou,³ and Jing Gong⁴

¹Southwest Petroleum University, Chengdu 610500, China

²China National Petroleum Corporation Guangzhou Petroleum Training Center, Guangzhou 510510, China

³Branch of China Petrochemical Marketing Co. Ltd., Jiangxi Yichun Oil Company, Yichun 336000, China

⁴China University of Petroleum, Beijing 102249, China

Correspondence should be addressed to Jun Zhou; 201599010096@swpu.edu.cn and Guangchuan Liang; lgcdjr@163.com

Received 21 October 2016; Accepted 21 December 2016; Published 31 January 2017

Academic Editor: Bhaskar Kulkarni

Copyright © 2017 Jun Zhou et al. This is an open access article distributed under the Creative Commons Attribution License, which permits unrestricted use, distribution, and reproduction in any medium, provided the original work is properly cited.

As an unconventional energy, coalbed methane (CBM) mainly exists in coal bed with adsorption, whose productivity is different from conventional gas reservoir. This paper explains the wellbore pressure drop, surface pipeline network simulation, and reservoir calculation model of CBM. A coupled surface/wellbore/reservoir calculation architecture was presented, to coordinate the gas production in each calculation period until the balance of surface/wellbore/reservoir. This coupled calculation method was applied to a CBM field for predicting production. The daily gas production increased year by year at the first time and then decreased gradually after several years, while the daily water production was reduced all the time with the successive decline of the formation pressure. The production of gas and water in each well is almost the same when the structure is a star. When system structure is a dendritic surface system, the daily gas production ranked highest at the well which is the nearest to the surface system collection point and lowest at the well which is the farthest to the surface system collection point. This coupled calculation method could be used to predict the water production, gas production, and formation pressure of a CBM field during a period of time.

1. Introduction

CBM is one of the most important sustainable energy for the strategy of sustainable development in the 21st century. China is abundant with CBM resource. About 36.81 trillion cubic meters is stored in depth of less than 2000 m under the ground in the field [1]. The wells are intensively distributed in the on-site CBM blocks. The gas production and pipeline operation parameters for undergoing construction project could be predicted by the integration of surface/wellbore/surface pipeline network to get closer to the actual production data, which optimizes and guides the CBM surface construction and improves the production to maximize the industry economic benefit. Over the past few decades, many scholars have been studying the integration of the oil and gas production system and several models have been put forward. Dempsey et al. [2] first studied the coupling of

gas reservoir flow simulation and surface system simulation, which built the foundation of other relative research on the production system integration. Startzman et al. [3], Trick et al. [4], Litvak and Darlow [5], Coats et al. [6], Al-Mutairi et al. [7], and Guyaguler et al. [8] also put forward their models of the reservoir/wellbore/surface system integration afterwards. Startzman et al. [3] proposed a model of reservoir-to-surface system coupled simulation, but this model only applied to the development of large offshore oil fields and the scope of application was narrow. Trick et al. [4] combined the black oil reservoir simulation software IMEX and the ground system simulation software FORGAS for forecasting the production of gas field. The coupling process of these two models is applicable to the coupling of any reservoir simulator with the ground system model which includes bottom-hole inflow dynamic curve and bottom-hole pressure loss calculation module. Litvak and Darlow [5] studied the

coupled model of reservoir and ground pipe network and proposed an implicit method to solve the network node and the reservoir grid. Coats et al. [6] proposed a model of the reservoir/wellbore/surface system integration. The model considered the complex condition of wellbore size and the down-hole equipment and solved the entire system at every step of the Newton iteration. Al-Mutairi et al. [7] calculated the IPR curves by using the pressure in the near-well drainage area, which overcome the shortcomings of previous sensitivity to the variation of well production when calculating the IPR curves using the grid parameters of reservoirs. Guyaguler et al. [8] proposed a similar approach, but in this method each subdomain needs to be solved repeatedly before reaching equilibrium, and then when the final equilibrium is reached the IPR curve that can reflect the condition of near-well reservoir is obtained. Although this method is time-consuming and the amount of calculation is large, it can reduce the balance error. The IPR curve method is mainly used for the conventional reservoir simulation and the unconventional gas reservoir numerical simulation method is time-consuming. Combined with material balance method for isothermal adsorption of coalbed methane, this paper proposes a method to meet the need of unconventional coalbed methane integrated simulation coupling CBM considering network model, wellbore pressure drop, CBM adsorbed state, and its drainage gas recovery mechanism.

2. Model Description

2.1. Wellbore Model. Coal reservoir and surface pipeline network was connected by CBM wellbore. The wellbore flow parameters directly affect gas production and surface network flow state. In the process of CBM production, the production is directly determined by bottom-hole flow pressure (BHFP). Figure 1 shows the annulus fluid distribution in the CBM wellbore. Gas and water enter the surface system from the annulus and tubing, respectively. Fluid in annulus can be distinguished by working fluid level as the gas column in the upper level and aerated fluid column in the lower level. Wellbore annulus pressure drop consists of the pressure drop of both parts. Many researches about calculation of BHFP had been suggested.

2.1.1. Single Phase Flow Model. Cullender and Smith [9] derived the calculation equation for pure gas well bottom-hole pressure (BHP) through the analysis of the energy equation for gas steady flow. This equation is known as Cullender-Smith method. Later, Texas Railroad Commission presented another calculation method for pure gas well BHP which is the average temperature mean deviation coefficient method [10]. The equations are as follows:

$$P_g = \sqrt{P_c^2 e^{2s} + \frac{1.324 \times 10^{-18} \lambda (TZq_{sc})^2}{(d_2 - d_1)^3 (d_2 + d_1)^2} (e^{2s} - 1)}, \quad (1)$$

$$s = \frac{0.03418 \gamma_g H}{TZ}.$$

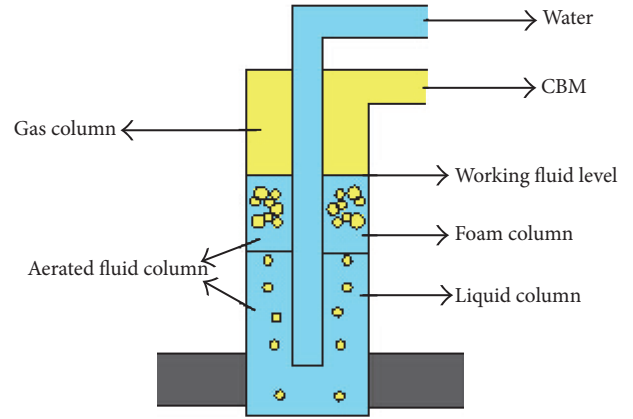


FIGURE 1: The annulus fluid distribution in the CBM wellbore.

2.1.2. Gas-Liquid Phase Flow Model. Takacs and Guffey [11], Chen and Yue [12], Oden and Jennings [13], Hasan and Kabir [14], Liu et al. [15], and Beggs and Brill [16] have proposed different calculation methods, respectively. Among those, Hasan-Kabir's method is as follows:

$$P_{wf} = P_c + \Delta P_g + r_L h_L - I_1 + I_2, \quad (2)$$

$$I_1 = \frac{C}{a(1-f_g)_{avg}} \ln \left[1 + \frac{ar_L(1-f_g)_{avg} h_L}{bC + a(P_c + \Delta P_g)} \right], \quad (3)$$

$$I_2 = \frac{M_g g C h_L}{ZRTa} - \frac{M_g g C^2 b}{ZRa^2 T r_L (1-f_g)_{avg}} \cdot \ln \left[1 + \frac{ar_L(1-f_g)_{avg} h_L}{bC + a(P_c + \Delta P_g)} \right], \quad (4)$$

$$C = \frac{q_{sc} T Z P_{sc}}{86400 A T_{sc}}, \quad (5)$$

$$f_g = \frac{v_{sg}}{a + b v_{sg}}, \quad (6)$$

$$v_{sg} = \frac{q_{sc} T Z P_{sc}}{A_a T_{sc} P}. \quad (7)$$

2.2. Surface Pipeline Network Model

2.2.1. Hydraulic Model of Pipe. Steady-state hydraulic calculation for a pipe is used to decide the pipeline pressure drop. Below is the calculation model of gas pipeline pressure drop:

$$q = \frac{\pi}{4} \sqrt{\frac{(P_Q^2 - P_Z^2) D^5}{\lambda Z R T L}}. \quad (8)$$

2.2.2. Hydraulic Calculation of Pipeline Network. For a pipeline network system with n nodes (wellhead and surface

system nodes) and m sections, n nodes are corresponding to n flow continuity equations. The node matrix equation formed by those the continuity equations can be written as the following form:

$$\mathbf{A}\mathbf{Q} = \mathbf{q}. \quad (9)$$

Usually, the relationship between the pressure loss and the flow rate of each pipe section could be expressed as the form of a vector function:

$$\mathbf{Q} = \phi(\Delta\mathbf{P}). \quad (10)$$

Pipe section pressure drop could be expressed by the pressure difference between the two endpoints of the section:

$$\Delta\mathbf{P} = \mathbf{A}^T\mathbf{P}. \quad (11)$$

Substituting (9), (10), and (11), the mathematical model for the node method could be derived as follows:

$$\mathbf{A}[\phi(\mathbf{A}^T\mathbf{P})] = \mathbf{q}. \quad (12)$$

2.2.3. Thermodynamic Calculation of Pipeline Network. Steady-state thermodynamic calculation is based on the analysis of steady-state hydraulic analysis. Gas phase temperature drop of the pipeline could be calculated by the Gertjan Zuilhof temperature drop formula which is frequently used in gas pipeline.

$$T = T_0 + (T_Q - T_0)e^{-ax}. \quad (13)$$

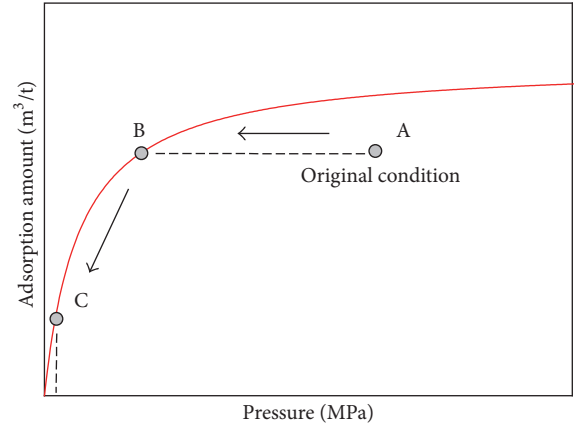
During the solving process, the main aim is to obtain the network node temperature and solve the problem by this parameter. The equation presented by Wei et al. [17] was employed.

$$T_i = \frac{\sum_{k=1}^m a_{ik}q_k c_k T_k^R + q_{gi}c_{gi}T_{gi}}{q_{ii}c_i}. \quad (14)$$

2.3. Reservoir Model. Three phases, coal, gas and water, coexist in CBM. The unique characteristics of dual porosity system make the productivity prediction different from the method used in conventional gas reservoir. So far, some people tried to predict the production performance using the CBM reservoir numerical simulation [18]. This approach requires a large amount of production data and geological data. It is therefore difficult to solve the model. The long calculation running time limits the application of the numerical method. In this paper, simple but effective material balance method is utilized to forecast the CBM well production performance.

2.3.1. CBM Mining. CBM is mainly stored as an adsorption state on the coal surface. Langmuir sorption isotherm equation is usually used to describe the relationship between the adsorption gas volume and pressure.

$$V = \frac{V_L P_r}{P_L + P_r}. \quad (15)$$



— Langmuir isothermal adsorption curve

FIGURE 2: Langmuir isothermal adsorption curve.

P_r represents the pressure (MPa); V represents the amount of gas at the pressure P_r (m^3/ton); V_L represents the Langmuir volume coefficient (m^3/ton); P_L represents the Langmuir pressure coefficient (MPa). Langmuir volume coefficient describes the adsorption constant (V_L) of methane adsorption isotherm. The physical meaning of this constant is the adsorbed gas volume when unit quality coal is under saturation condition at a given temperature. Coalbed methane Langmuir pressure coefficient describes the adsorption constants (P_L). The physical meaning of this constant is the pressure when the amount of methane adsorbed on the coal reaches half of the Langmuir volume.

The red curve in Figure 2 shows the Langmuir isothermal adsorption curve when P_r is 2.38 and V_L is $38.16 \text{ m}^3/\text{t}$. The adsorption volume increases with pressure, but when the pressure rises to a certain value, the volume does not change, which means that the adsorption of coal surface is under saturation.

In addition, the Langmuir pressure coefficient is a parameter which affects the shape of isotherm curve of coal adsorption. The smaller the Langmuir pressure coefficient, the greater the degree of bending of the adsorption curve.

Furthermore, adsorption isotherm curve has obvious effect on coalbed methane production. Coalbed can be divided into 3 states [19] in theory, supersaturated, saturated, and undersaturated. In real situation, the coal bed is mostly undersaturated. Figure 2 shows the CBM mining stage in undersaturated condition. Point A in the picture shows the initial point of the reservoir. Point B is the saturation point. Point C indicates the shut-in pressure. As water exists in coal bed cracks, the coal reservoir pressure can be reduced by pumping the confined water at the beginning till the reservoir pressure reduced to the critical pressure point B. Then the adsorbed methane starts releasing a large amount of free methane and flowing to the wellhead. This stage is influenced by coal matrix permeability. As more and more water is discharged, gas production increases rapidly to reach a peak. After the reservoir pressure decreases to a certain level, gas

production rate will decline gradually (B-C) until the shut-in condition (C). The whole CBM exploitation cycle completes at this point.

2.3.2. *Material Balance Method.* The CBM formation reserve equals the sum of the amount of adsorption and free gas.

$$V_r = \rho_b Ah \frac{V_L P_r}{P_L + P_r} + \frac{\phi Ah (1 - S_w)}{B_g}. \quad (16)$$

Material balance method [20] includes King model, Seidle model, and Jensen-Smith model, in which King model is the most commonly used one. This model assumes that the gas adsorption and desorption equilibrium follow Langmuir sorption isotherms. Gas output can be written as the following form:

$$G_p = \rho_b Ah V_L \left(\frac{P_i}{P_L + P_i} - \frac{P_r}{P_L + P_r} \right). \quad (17)$$

Substituting the formation coefficient to (17), the equation can be transformed to the following form:

$$G_p = \phi_i Ah \frac{T_{sc} Z_{sc}}{P_{sc} T_r} \left(\frac{P_i}{Z_i^*} - \frac{P_r}{Z^*} \right), \quad (18)$$

Z^*

$$= \frac{Z}{[1 - c_f (P_i - P_r)] (1 - \bar{S}_w) + (\rho_b B_g / \phi_i) (V_L P_r / (P_L + P_r))}, \quad (19)$$

$$\bar{S}_w = \frac{S_{wi} [1 + c_w (P_i - P_r)] + 5.615 (W_e - B_w W_p) / \phi_i Ah}{[1 - c_f (P_i - P_r)]}. \quad (20)$$

Original gas in place (OGIP) can be calculated as follows:

$$\text{OGIP} = \phi_i Ah \frac{T_{sc} Z_{sc} P_i}{P_{sc} T_r Z_i^*}. \quad (21)$$

Substituting (21) in (18), a linear relation between the average gas reservoir pressure and the cumulative gas production can be obtained as follows:

$$\frac{P_r}{Z^*} = - \frac{P_i}{Z_i^* (\text{OGIP})} G_p + \frac{P_i}{Z_i^*}. \quad (22)$$

At the beginning of undersaturated CBM exploration well, formation water is the main product. Gas production is too small to ignore. Water production in well is constant. The formation pressure difference equation at this time can be written as

$$P_r - P_{wf} = \frac{q_w t}{c_i N_w} + \frac{141.2 B_w \mu_w q_w}{kh} \left(\ln \frac{r_e}{r_{wa}} - \frac{3}{4} \right), \quad (23)$$

$$N_w = \frac{7758 \phi Ah}{B_w}.$$

2.3.3. Productivity Prediction

(1) *Gas Production Equation.* Below is the gas production equation for CBM:

$$q_g = \frac{k_g h [m(P_r) - m(P_{wf})]}{1422 T \left[\ln \frac{r_e}{r_w} - \frac{3}{4} + s_f \right]}. \quad (24)$$

Among those, $m(P)$ is the gas pseudo-pressure whose definition is the followed one:

$$m(P) = \int_{P_b}^P \frac{P}{\mu_g Z} dP. \quad (25)$$

(2) *Water Production Equation.* Below is the water production equation for CBM:

$$q_w = \frac{k_w h [P_r - P_{wf}]}{141.2 \mu_w B_w \left[\ln \frac{r_e}{r_w} - \frac{3}{4} + s \right]}. \quad (26)$$

(3) *Relationship between Coal Bed Permeability and Porosity.*

Coal is composed of cracks and coal matrix. Coal matrix stores gas by adsorption. Diffusion is the primary means of the gas flowing in the matrix. There is a huge difference between the permeability in coal and in conventional fracture gas reservoir. Below is the relationship between the porosity and permeability:

$$\left(\frac{k_f}{k_0} \right) = \left(\frac{\phi_f}{\phi_0} \right)^n. \quad (27)$$

The declination of formation pressure will result in absolute permeability change in the reservoir. This influence can be described using Palmer-Mansoori model [21]:

$$\frac{\phi}{\phi_0} = 1 + \frac{C_m}{\phi_0} (P_r - P_i) + \frac{\varepsilon_l}{\phi_0} \left(\frac{K}{M} - 1 \right) \left(\frac{P_r}{P_L + P_r} - \frac{P_i}{P_L + P_i} \right), \quad (28)$$

$$C_m = \frac{1}{M} - \left(\frac{K}{M} + f - 1 \right) \gamma,$$

$$\frac{K}{M} = \frac{1}{3} \left(\frac{1 + \gamma}{1 - \gamma} \right).$$

With the dehydration of coal, the gas and water in the cracks is in Darcy flow. Coal saturation changes so that the relative gas-water permeability changes as well. So Corey and Rathjens [22] presented the equations below:

$$\frac{k_{rg}}{k_{rg0}} = \left(\frac{S_g - S_{gc}}{1 - S_{wc} - S_{gc}} \right)^{n_g} \quad (S_g > S_{gc}), \quad (29)$$

$$\frac{k_{rw}}{k_{rw0}} = \left(\frac{S_w - S_{wc}}{1 - S_{wc}} \right)^{n_w} \quad (S_g \geq 1 - S_{wc}).$$

3. Problem Statement

Coalbed methane production system simulation and deliverability forecasting can be described below. The following parameters are given:

- (1) reservoir parameters: initial reservoir pressure, reservoir temperature, coalbed thickness, and so on,
- (2) basic wellbore parameters: tubing diameter, inner diameter, well depth, liquid level depth, drilling fluid density, and so on,
- (3) surface pipeline network: network structure, pipe diameter, and so on,
- (4) composition of CBM.

The following parameters need to be determined:

- (1) reservoir pressure,
- (2) bottom hole flowing pressure,
- (3) gas rate,
- (4) water rate,
- (5) node pressure and flow rate of the pipeline network.

4. Solution Algorithm

4.1. Calculation Algorithm of BHFP. The calculation process of BHFP is described as follows:

- (1) The pressure of the working fluid level P_g is unknown. To obtain the average pressure and average temperature, we should first assume the initial value of P_g .
- (2) The gas deviation factor and the friction coefficient at the average pressure and average temperature will be then calculated.
- (3) Substitute the results in (1) to calculate P_g .
- (4) Comparing the calculated result and the assumed value of P_g , if the difference of P_g does not meet the error requirement, the calculated P_g will be used as the assumed value. Then repeat step (1) to step (3) until the difference of P_g meets the error requirement.
- (5) The initial value of BHFP P_{wf} should also be assumed. The average pressure and average temperature will be calculated then.
- (6) The average deviation coefficient Z could be calculated based on the average pressure and average temperature.
- (7) According to (7), v_{sg} can be calculated to determine the value of a and b .
- (8) After evaluating I_1 and I_2 , P_{wf} can be calculated from (2).
- (9) Comparing the calculated result and the assumed value of P_{wf} , if the difference of P_{wf} does not meet the error requirement, the calculated P_{wf} will be used as the assumed value. Then repeat step (5) to step (8) until the difference of P_{wf} meets the error requirement.

4.2. Surface Network Parameters Calculation. During the calculation process of gas phase pipeline network, the hydraulic calculation and thermodynamic calculation influence each other; therefore, the entire calculation is a coupling hydraulic/thermodynamic iterative process. The specific calculation steps are described below:

- (1) Input basic data of the pipeline network, including pipe length, diameter, absolute roughness, gas composition, ambient temperature, and overall heat transfer coefficient.
- (2) The initial value of node pressure vector \mathbf{P}_0 , node flow vector \mathbf{q}_0 and node temperature vector \mathbf{T}_0 should be assumed. The initial value of k is 1.
- (3) The solution (12) should be calculated using the node method for steady-state hydraulic pipe network. The node pressure vector \mathbf{P}_k and node flow vector \mathbf{q}_k under the current node temperature vector \mathbf{T}_{k-1} could be both obtained.
- (4) According to (13), the temperature drop vector $\Delta\mathbf{T}_k$ under \mathbf{P}_k and \mathbf{q}_k for each pipe branch can be calculated.
- (5) The solving sequence of the network node temperature should be established.
- (6) Node temperature vector \mathbf{T}_k can be solved by temperature for each node calculated from the solving sequence and (14).
- (7) If $|\mathbf{T}_k - \mathbf{T}_{k-1}| < \varepsilon$ (ε is the error precision), the calculation can be stopped. If not, \mathbf{T}_k should be treated as the initial node temperature vector for a new iterative calculation circle, and $k = k + 1$. Then repeat step (3) to step (7).

4.3. Reservoir Simulation. Coal reservoir production can be roughly predicted if the material balance equation and the CBM gas/water production equation are combined with the known BHFP. The specific steps are as follows:

- (1) Input basic data of reservoir, including Langmuir volume, Langmuir pressure, bulk density, initial reservoir pressure, and porosity.
- (2) OGIP can be obtained by (21). Then the desorption pressure corresponding with the gas reserves can be obtained. This result will be compared to the gas reservoir pressure at this time.
- (3) If gas reservoir pressure is bigger than desorption pressure, that means the coalbed is undersaturated. Water production rate at this time q_w and the cumulative water production in a period $\Delta\mathbf{T}$ can be calculated by (26). Then this cumulative water production can be utilized to calculate the gas reservoir pressure at the end of the time period. Repeat step (3) until the gas reservoir pressure equals the desorption pressure. Then proceed to step (4).
- (4) If gas reservoir pressure equals the desorption pressure (supersaturated state of the coal is not considered

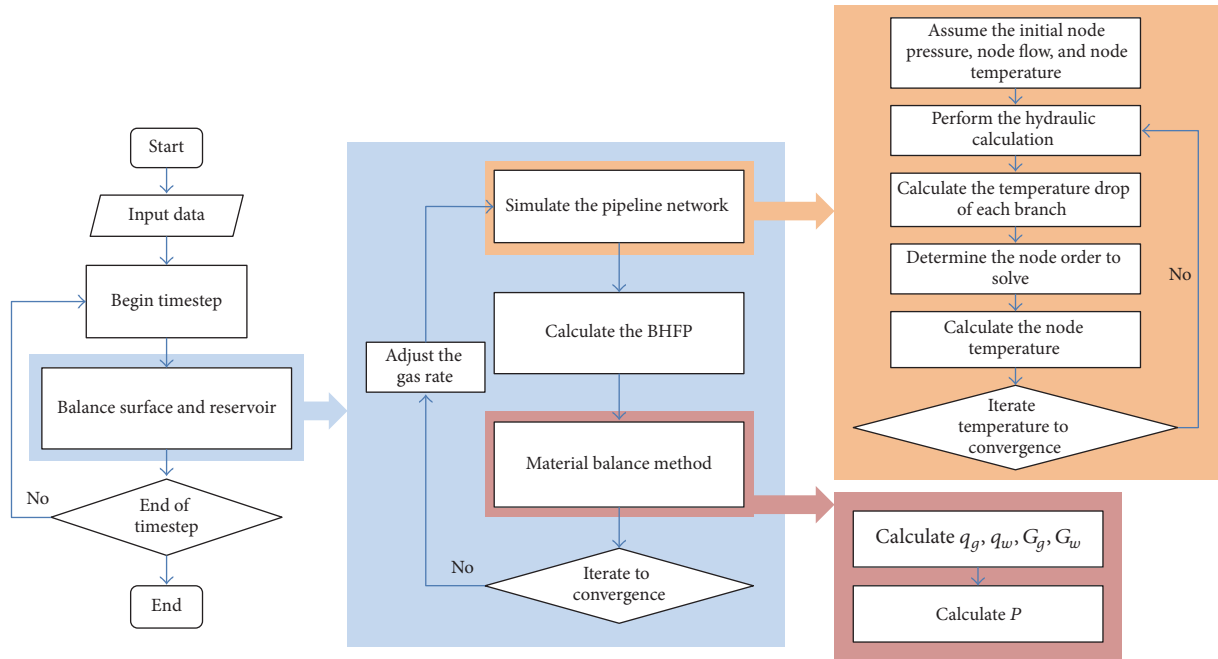


FIGURE 3: CBM reservoir/surface coupling algorithm.

here), that means the coalbed is saturated. Both gas and water will be produced from the coalbed. Q_w will be calculated. The gas production per unit time q_g and the cumulative gas production and cumulative water production can be calculated from (24). Then the gas reservoir pressure at the end of the time period can be calculated. Repeat step (4) until it reaches the shut-in pressure.

4.4. Production System Coupling Calculation. The basic assumptions of CBM production system coupling calculation are as follows:

- (1) During the gas production process of CBM, although the gas production changes with time, it still can be treated as constant in a small time interval. In this time interval, the flow in the wellbore and the surface pipe network can be regarded as a steady flow.
- (2) In the actual production, the working liquid level in the wellbore always changes due to the influence of gas production, water production, and the formation condition. The main factor is the production rate. In this case, the working liquid level is assumed constant.

Figure 3 shows the flow chart of CBM production system coupling calculation.

CBM production system coupling calculation model is the unity of CBM well productivity prediction model, wellbore calculation model, and surface pipe network model. The production indexes such as formation pressure, bottom hole pressure, and gas production can be determined by coupling iterations of the three models. This calculation model can

be employed to optimizing the production plan. The specific calculation process is described below:

- (1) Input the basic data of CBM reservoir, wellbore, and surface network.
- (2) Do the surface, wellbore, and reservoir coupling calculation.
- (3) Assume the initial iteration value of gas production for each well at this time; then calculate the wellhead pressure for each well according to the surface pipe network model.
- (4) According to the calculated initial value of wellhead pressure and gas production, calculate the BHFP for each well using the wellbore model, respectively.
- (5) According to the calculated BHFP, calculate the gas production at the end of the production period for each well using the CBM reservoir productivity prediction model.
- (6) Compare the calculated value and the assumed value. If the difference satisfies the requirements of the error precision, calculate the cumulative gas production and cumulative water production. If not, replace the calculated value as the initial iteration value and then repeat step (3) to step (5).
- (7) See whether it reaches the end of the production period or not. If yes, the calculation ends. If not, repeat step (2) to step (5).

5. Examples

5.1. Evaluation of BHFP Calculation Method. In the calculation of CBM BHFP, wellhead casing pressure data can be

generally read by the wellhead pressure gauge. The pressure difference of pure gas column and the pressure difference of mixed gas liquid column can be calculated from the model introduced above. The sum of these three values is the BHFP. Although many scholars have proposed different methods to calculate BHFP, they did not compare or evaluate the applicable range and calculation accuracy.

In this paper, different calculation models have been studied and effective model with higher calculation accuracy is recommended by comparing different models. Study shows that the results of average temperature, average deviation coefficient method, and the results of Cullender-Smith method are approximately the same [10]. So the average temperature average deviation coefficient method is used to calculate the pressure difference for pure gas column. The following four models to calculate CBM BHFP are studied by combining the method for calculating mixed gas liquid pressure difference.

Model 1. Average temperature and average deviation coefficient method is used to calculate the pressure difference for pure gas column. Jialang Chen-Xiang'an Yue method [12] is used to calculate the pressure difference for mixed gas liquid column.

Model 2. Average temperature and average deviation coefficient method is used to calculate the pressure difference of pure gas column. Hasan-Kabir analytic method [14] is used to calculate the pressure difference for mixed gas liquid column.

Model 3. Average temperature and average deviation coefficient method is used to calculate the pressure difference for pure gas column. Beggs-Brill method [16] is used to calculate the pressure difference for mixed gas liquid column.

Model 4: Xinfu Liu Method. To obtain the optimized model to calculate CBM BHFP, these 4 models are used for 21 gas wells and the results will be compared with the field measured data. In Figure 4, the red line shows the field measured data of BHFP. Data number 1 to number 6 (dataset 1) are from [23], data number 7 to number 15 (dataset 2) are from [15], and data number 16 to number 21 (dataset 3) are the measured data from a certain block of field. Figures 4 and 5 are the calculation results and the relative error of each model.

After comparing these 4 models, the result of Model 1 for dataset 2 is close to the measured value, yet the calculation result error is large, which means the calculation precision of this model changes with the gas well conditions. The same result can be drawn from Model 3 as well. The calculation results of Model 1 for dataset 1 and dataset 3 are both close to the measured result. Using Model 2, we can also obtain the result close to the measured value. The error is within 20% and calculation accuracy is relatively high.

Table 1 is the summary of the application, calculation accuracy, and the advantages and disadvantages of each model. From the present result, though the calculation results of Jialang Chen-Xiang'an Yue method and Hasan-Kabir analytic method are close to each other, Jialang Chen-Xiang'an Yue method has a narrower applicable condition

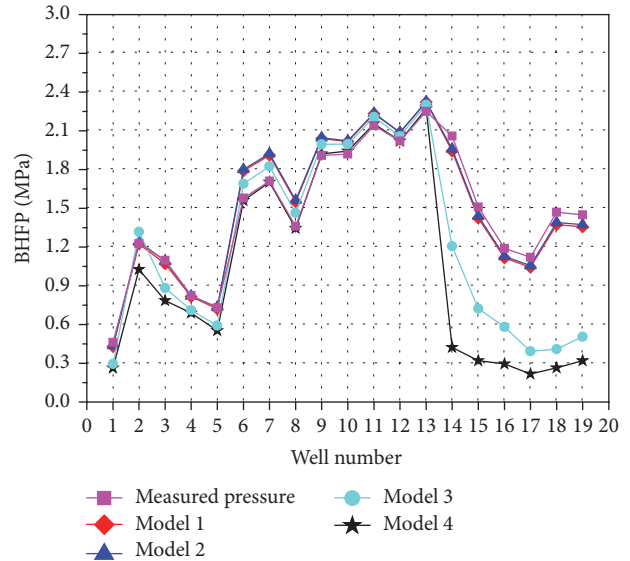


FIGURE 4: Comparison of calculated result with measured value.

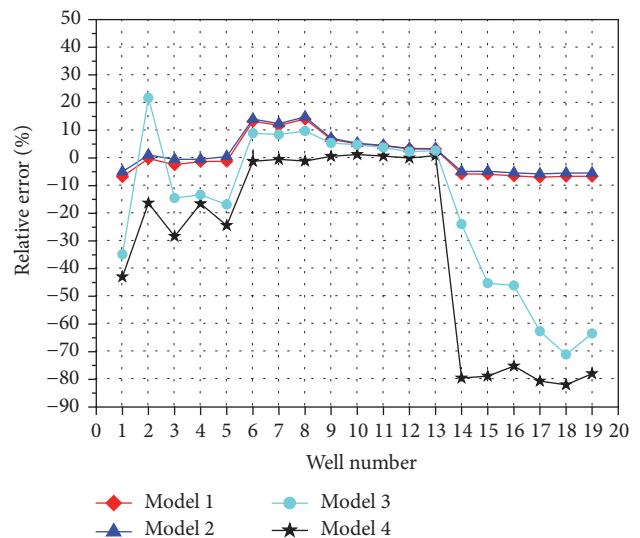


FIGURE 5: Relative errors of calculated result.

which is $GCF > 0.3$. Among the 3 models, Hasan-Kabir analytic method has a relatively high calculation accuracy and wide applicability. So this model is chosen to calculate the CBM well BHFP.

5.2. Example 1. Coupled calculation method was applied to 2 blocks of a CBM field. System structure is illustrated in Figure 6, which is a star shaped structure. The output for each well will be collected to the center node (Node 12) through a separate line.

Coupling algorithms are used for productivity prediction. The parameters of coal reservoir and gas composition are given in Tables 2 and 3.

(1) *Daily Gas Production.* Predicted gas production of each well is shown in Figure 7.

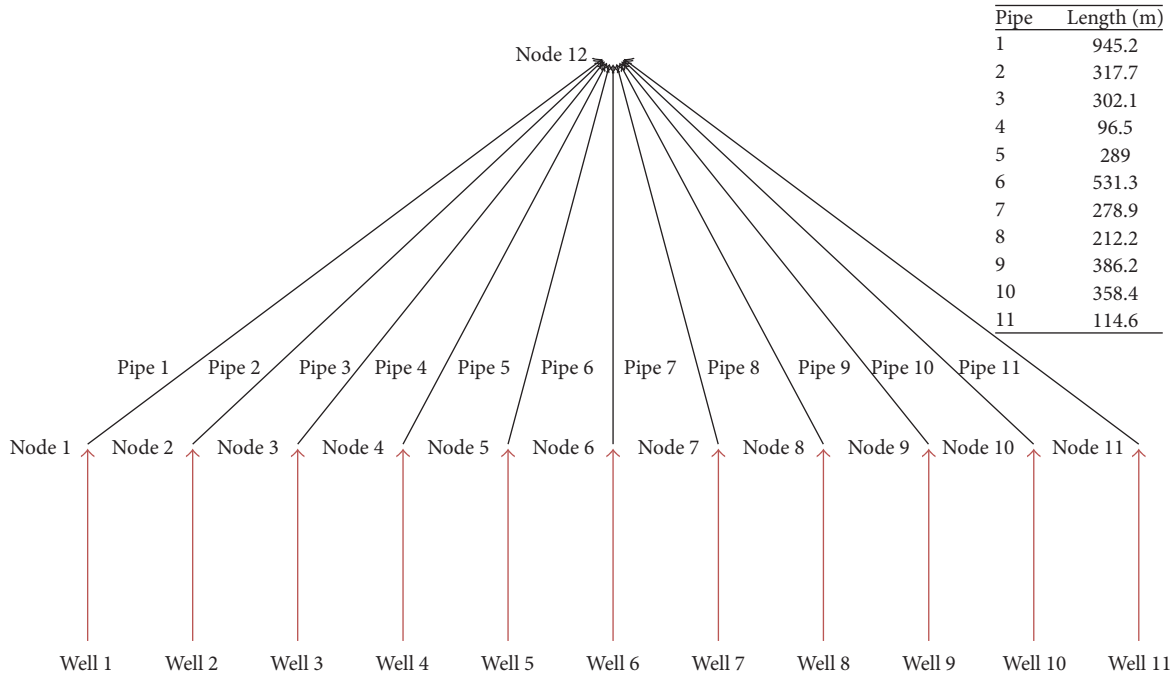


FIGURE 6: Surface pipeline network system.

TABLE 1: Comparison of the four models.

Calculation method	Application	Calculation accuracy	Advantages/disadvantages
Model 1	GCF > 0.3	Relatively high	High precision, but large amount of calculation, narrow application scope
Model 2	All cases	Relatively high	Simple calculation process, high precision, good stability
Model 3	All cases	Change with the gas well conditions	Complex calculation process, poor stability
Model 4	All cases	Change with the gas well conditions	Large amount of calculation, poor stability

TABLE 2: Parameters of coal reservoir.

Input parameters	Value
Initial reservoir pressure (MPa)	5.28
Reservoir temperature (K)	304.15
Initial porosity (%)	4.5
Formation thickness (m)	6.2
Drainage area (m ²)	90000
Bulk density (t/m ³)	1.45
Gas content (m ³ /t)	14.1
Langmuir volume (m ³ /t)	38.16
Langmuir pressure (MPa)	2.38

TABLE 3: Composition of CBM.

Composition	CH ₄	C ₂ H ₆	N ₂	CO ₂
Mole present (%)	96.17	0.05	3.71	0.07

Figure 7 shows the gas production for each well in the next 10 years. As can be seen from Figure 7, the daily gas

production change trend of all wells is basically identical. In the initial production stage, water is the main product. Gas production is 0. As time goes by, these 11 gas wells begin to produce gas. The gas production of each well is close to each other, and they increase year by year at the beginning and then decrease afterwards. The peak appears in the 2280th days at about 2800 m³/d.

(2) *Daily Gas Production.* Water production of each gas well under the star shaped gathering structure is shown in Figure 8.

Figure 8 shows the water production for each well in the next 10 years. As can be seen from Figure 8, the daily water production is nearly the same with obvious change trend. In the initial time of production, all gas wells begin to show formation water and the production rate is 35.67 m³/d. Along with the water emergence, the formation pressure decreased gradually to the critical desorption pressure of CBM. Gas begins to desorb. Throughout the whole gas production process, formation water discharged from each gas well reduces gradually. In the 10th year, it reaches 1.97 m³/d. In the later stages of production, water production of each gas well

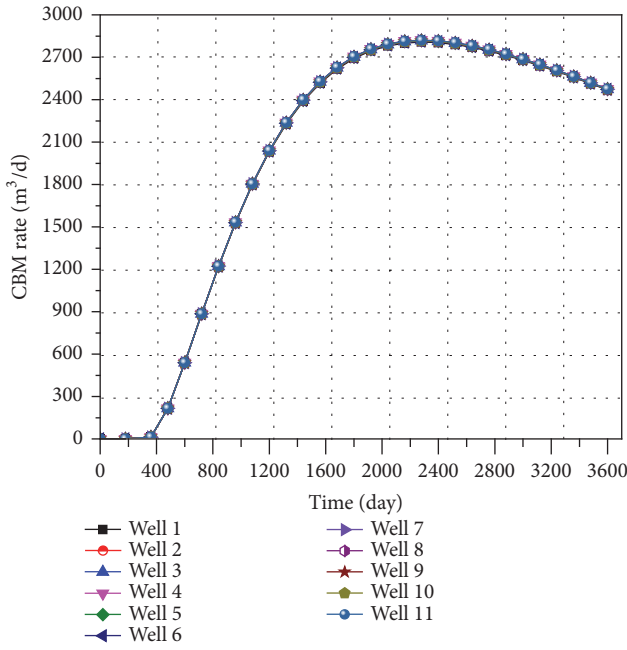


FIGURE 7: Daily well gas productions.

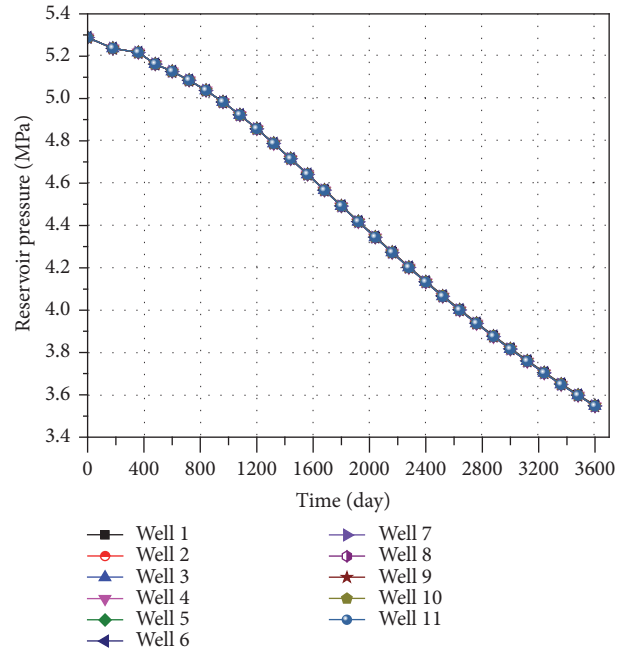


FIGURE 9: Reservoir pressures.

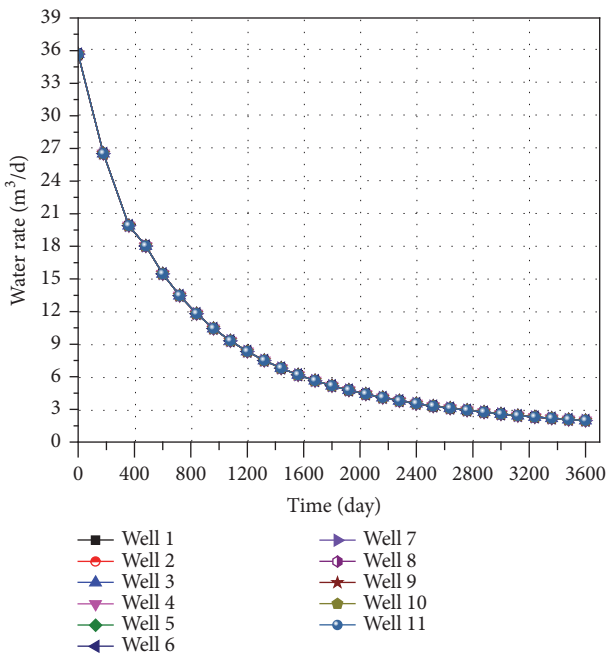


FIGURE 8: Daily well water productions.

become less and less and almost no water is produced after a period of time.

(3) *Formation Pressure.* The formation pressure changes are shown in Figure 9.

Figure 9 is the reservoir pressure of each well with the change of time. As can be seen from Figure 9, the gas reservoir pressure of each well is almost the same which all decreases with the time. During this process, water production of

each gas well reduces gradually. When the reservoir pressure decreases to the critical desorption pressure of CBM, gas begins to desorb from the surface of the coal matrix and comes out from the wellhead. In the 10th year after production, reservoir pressure drops from 5.28 MPa to 3.55 Pa.

5.3. *Example 2.* System structure is shown in Figure 10, which is a dendritic surface system.

(1) *Daily Gas Production.* Future gas production for each gas well is shown in Figure 11.

Figure 11 shows the gas production for each well in the next 10 years. It can be observed in Figure 11 that the daily gas production for each well is approximately the same at the beginning of production but different significantly afterwards. The largest production goes to Well 7 which is the nearest to the collection point (Node 12), while the smallest production is of Well 1 which is the farthest to the collection point. However, during the whole process, the change trend of gas production for each well is consistent basically. At the first time, only formation water is desorbed so the gas production is 0. As time goes by, these 11 gas wells begin to produce with the gas production increasing at the beginning and decreasing after a few years. Nevertheless, the peak time for each well is not the same. Among them, the gas production of Well 1, Well 2, Well 3, and Well 4 arrives to the peak in the 2520th day, while the gas production of Well 5 and Well 11 reaches a peak in the 2400th day.

(2) *Daily Water Production.* Future water production for each gas well is shown in Figure 12.

Figure 12 is the water production for each well in the next 10 years. As shown, the water production for each well

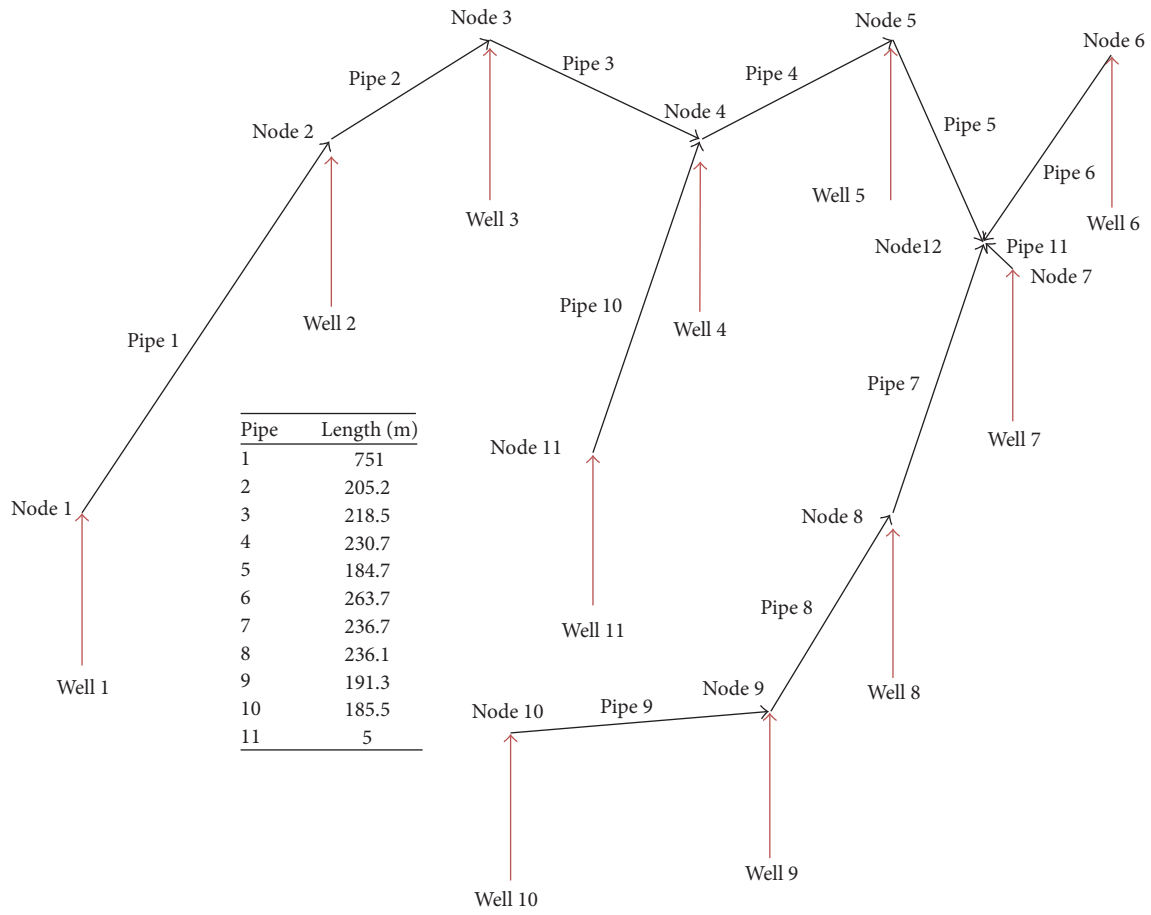


FIGURE 10: Surface pipeline network system.

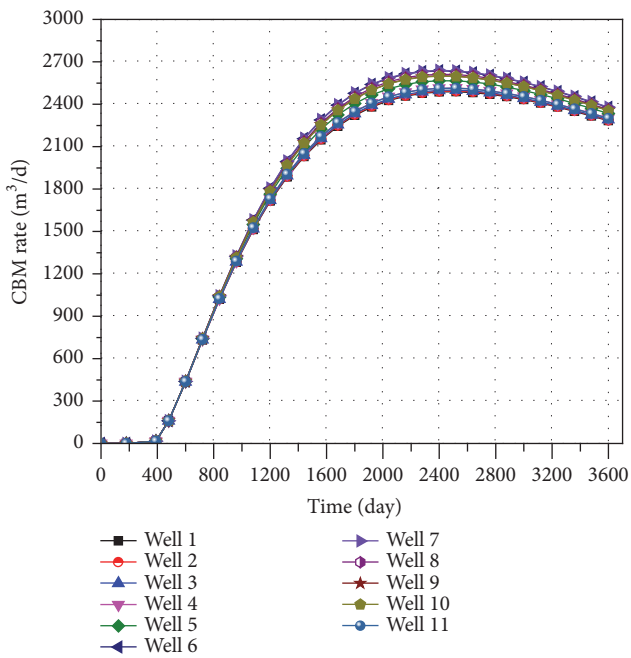


FIGURE 11: Daily well gas productions.

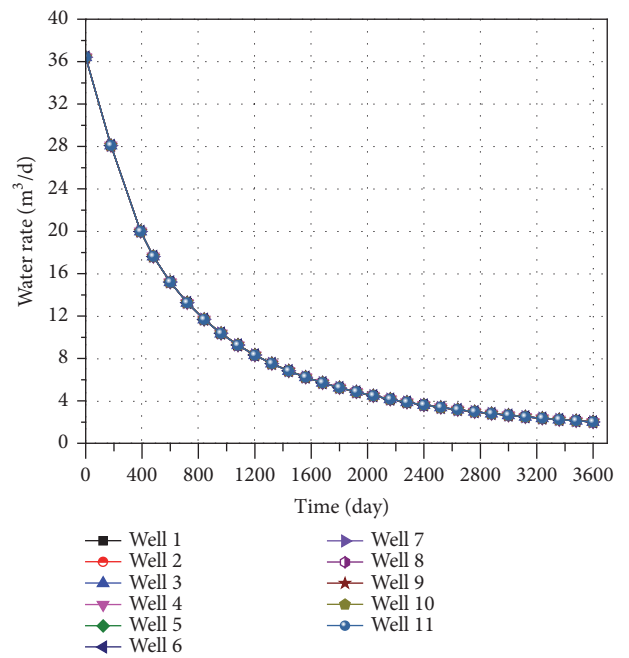


FIGURE 12: Daily well water productions.

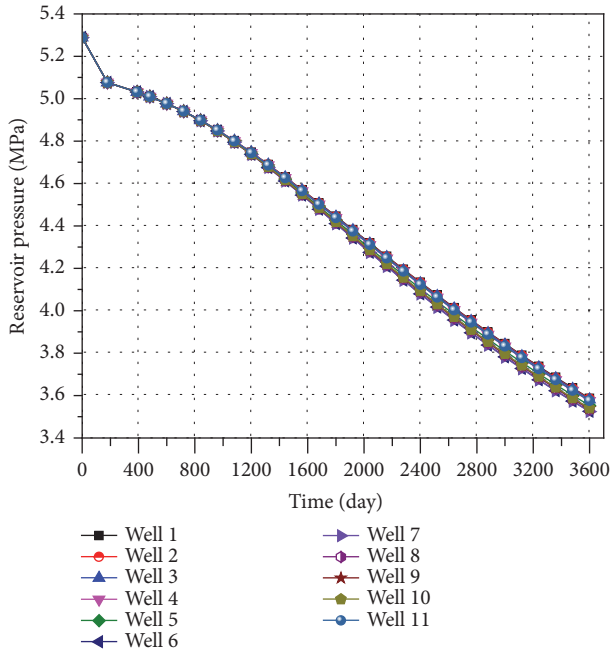


FIGURE 13: Reservoir pressures.

is basically the same. At the beginning of production, the formation water begins to desorb from formation with the production $36.41 \text{ m}^3/\text{d}$ for each well. Along with the large amount of water abjection, the reservoir pressure reduces gradually to the critical desorption pressure and then gas begins to desorb. During the entire gas production, water production for gas well decreases gradually to $2.02 \text{ m}^3/\text{d}$ in the 10th year. In the late stage of production, water production keeps on decreasing and almost no more water is produced after a period of time.

(3) *Formation Pressure.* The formation pressure changes are illustrated in Figure 13.

Figure 13 is the reservoir pressure for each well with the change of time. At the beginning of production, the reservoir pressure of each well is nearly the same. Later, they are slightly different from each other. The largest reservoir pressure goes to Well 7 which is the nearest to the collection point (Node 12), while the smallest reservoir pressure is Well 1 which is the farthest to the collection point. During the whole production process, reservoir pressure for each well decreases with different decline rate at different periods. In the initial production stage, the decline rate of reservoir pressure is fast and then the pressure falls more slowly. In the 10th year, reservoir pressure falls to 3.53 MPa from original 5.28 MPa.

6. Summary

This paper describes a coupling surface/wellbore/reservoir simulation algorithm which can be used to predict gas production and water production for a period of time. Node method is used for the surface system simulation. Thermodynamic and hydraulic calculation are coupled together to

calculate. CBM BHFP shows that the combination of Hasan-Kabir analytic method and average temperature average deviation coefficient method can provide a relatively high accuracy. The advantages and disadvantages of different combination models are listed as well. CBM productivity prediction is based on material balance. The method presented in this paper can be used to assist the CBM system analysis for CBM engineers by 2 validation examples.

Nomenclature

- a : Coefficient, dimensionless
- a_{ik} : Element of A
- A : Drainage area, m^2
- A_a : Sectional area of annulus, m^2
- A : Correlating matrix of the node and pipe
- A^T : Transpose matrix of A
- b : Coefficient, dimensionless
- B_g : Gas formation volume factor, m^3/Nm^3
- B_w : Water formation factor, m^3/Nm^3
- c_f : Formation compressibility, MPa^{-1}
- c_i : Heat capacity of the medium which flows out from node i , $\text{J}/(\text{kg}\cdot\text{K})$
- c_k : Heat capacity of the medium in section k , $\text{J}/(\text{kg}\cdot\text{K})$
- c_{gi} : Heat capacity of the medium which flows into the network from node i , $\text{J}/(\text{kg}\cdot\text{K})$
- c_t : Total compressibility, MPa^{-1}
- c_w : Water compressibility, MPa^{-1}
- C_m : Matrix compressibility, MPa^{-1}
- d_1 : Tubing outside diameter, m
- d_2 : Tubing inside diameter, m
- dh_L : Step length of aerated fluid column, m
- D : Internal diameter, m
- e : Absolute roughness, m
- f : Tuning factor, dimensionless
- f_g : Gas porosity, dimensionless
- g : Gravity acceleration, m/s^2
- G_p : Produced gas, m^3
- h : Formation thickness, m
- h_L : Aerated fluid column length, m
- H : Gas column length, m
- k : Permeability, md
- k_0 : Initial permeability, md
- k_f : Final permeability, md
- k_g : Effective permeability to gas, md
- k_w : Effective permeability to water, md
- k_{rg} : Relative permeability to gas, dimensionless
- k_{rw} : Relative permeability to water, dimensionless
- k_{rg0} : Final relative permeability to gas, dimensionless
- k_{rw0} : Final relative permeability to water, dimensionless
- K : Bulk elastic modulus, MPa
- L : Pipe length, m
- M : Axial constraint modulus, MPa

M_g : Gas molar mass, kg/mol
 n : Exponent, dimensionless
 n_g : Exponential of relative gas permeability curve, dimensionless
 n_w : Exponential of relative water permeability curve, dimensionless
 N_w : Original water in place, m³
 P : Average pressure, MPa
 P_b : Arbitrary base pressure, MPa
 P_c : Surface casing pressure, MPa
 P_g : Pressure at working fluid level, MPa
 P_i : Initial reservoir pressure, MPa
 P_L : Langmuir pressure, MPa
 P_Q : Inlet pressure of pipe, MPa
 P_r : Average reservoir pressure, MPa
 P_Z : Outlet pressure of pipe, MPa
 P_{wf} : Bottom-hole flowing pressure, MPa
 P_{sc} : Standard pressure, MPa
 ΔP_g : Pressure drop of gas column, MPa
 \mathbf{P} : Node pressure vector
 $\Delta \mathbf{P}$: Pipe pressure drop vector
 q : Mass flow rate, kg/s
 q_g : Gas rate, m³/d
 q_k : Mass flow of the medium in section k , kg/s
 q_w : Water rate, m³/d
 q_{gi} : Mass flow of the medium which flows into the network from node i , kg/s
 q_{ii} : Total mass flow of the medium which flows into node I , kg/s
 q_{sc} : Gas production rate in standard state, m³/d
 \mathbf{q} : Node flow vector
 \mathbf{Q} : Pipe flow vector
 r_e : External radius of reservoir, m
 r_L : Liquid gravity, Pa·m⁻¹
 r_w : Wellbore radius, m
 r_{wa} : Apparent wellbore radius, m
 R : Universal gas constant, J/(mol·K)
 s : Definition parameter, dimensionless
 s_f : Skin factor, dimensionless
 S_g : Average gas saturation, dimensionless
 S_w : Water saturation, dimensionless
 S_{gc} : Irreducible gas saturation, dimensionless
 S_{wc} : Irreducible water saturation, dimensionless
 S_{wi} : Initial water saturation, dimensionless
 \bar{S}_w : Average water saturation, dimensionless
 T : Temperature, K
 T_0 : Ambient temperature, K
 T_i : Temperature of node i , K
 T_r : Reservoir temperature, K
 T_Q : Temperature of the starting point of the pipeline, K
 T_{gi} : Temperature of the medium which flows into the network from node i , K
 T_{sc} : Standard temperature, K
 T_k^R : Temperature of the end of section k , K
 V_{sg} : Apparent velocity, m/s

V : Gas content, m³/t
 V_L : Langmuir volume, m³/t
 V_r : Reserve volume, m³
 W_e : Encroached water, m³
 W_p : Produced water, m³
 Z : Gas compressibility factor, dimensionless
 Z_{sc} : Standard gas compressibility factor, dimensionless
 Z^* : Gas factor for unconventional gas reservoir, dimensionless
 ν : Poisson ratio, dimensionless
 μ_g : Gas viscosity, Pa·s
 μ_w : Water viscosity, Pa·s
 ϕ : Porosity, dimensionless
 ϕ_0 : Initial porosity, dimensionless
 ϕ_f : Final porosity, dimensionless
 ε_i : Maximum strain, dimensionless
 γ : Matrix shrinkability, MPa⁻¹
 γ_g : Gas relative density, dimensionless
 λ : Hydraulic friction coefficient, dimensionless
 ρ_b : Bulk density of the coal, t/m³.

Competing Interests

The authors declare that there is no conflict of interests regarding the publication of this paper.

Acknowledgments

The authors thank the financial support from the Young Scholars Development Fund of SWPU (201599010096).

References

- [1] J. Li and J. Yang, "Brief discussion on development of coal seam gas industry in China," *SCI-TECH Innovation and Productivity*, vol. 8, pp. 20–22, 2011.
- [2] J. R. Dempsey, J. K. Patterson, K. H. Coats, and J. P. Brill, "An efficient model for evaluating gas field gathering system design," *Journal of Petroleum Technology*, vol. 23, no. 9, pp. 1067–1073, 1971.
- [3] R. A. Startzman, W. M. Brummett, J. C. Ranney, A. S. Emanuel, and R. M. Toronyi, "Computer combines offshore facilities and reservoir forecasts," *Petroleum Engineer International*, vol. 49, no. 5, pp. 65–74, 1977.
- [4] M. D. Trick, R. Agarwal, J. R. Ammer et al., *Gas-Field Deliverability Forecasting: A Coupled Reservoir Simulator and Surface Facilities Model*, USDOE Morgantown Energy Technology Center, 1994.
- [5] M. L. Litvak and B. L. Darlow, "Surface network and well tubinghead pressure constraints in compositional simulation," in *Proceedings of the SPE Reservoir Simulation Symposium*, San Antonio, Tex, USA, 1995.
- [6] B. K. Coats, G. C. Fleming, J. W. Watts, M. Ramé, and G. S. Shiralkar, "A generalized wellbore and surface facility model, fully coupled to a reservoir simulator," *SPE Reservoir Evaluation & Engineering*, vol. 7, no. 2, pp. 132–142, 2004.

- [7] S. Al-Mutairi, E. Hayder, A. Munoz, A. Al-Shammari, and N. Al-Jama, "A study of coupling surface network to reservoir simulation model in a large middle east field," in *Proceedings of the North Africa Technical Conference and Exhibition 2010 (NATC '10)*, pp. 805–814, Cairo, Egypt, February 2010.
- [8] B. Guyaguler, V. J. Zapata, H. Cao, H. F. Stamati, and J. A. Holmes, "Near-well-subdomain simulations for accurate inflow-performance- relationship calculation to improve stability of reservoir/network coupling," *SPE Reservoir Evaluation & Engineering*, vol. 14, no. 5, pp. 634–643, 2011.
- [9] M. H. Cullender and R. V. Smith, "Practical solution of gas-flow equations for wells and pipelines with large temperature gradients," *Society of Petroleum Engineers*, pp. 281–287, 1956.
- [10] C. Yang, *Gas Extraction Engineering*, Petroleum Industry Press, Beijing, China, 2001.
- [11] G. Takacs and C. G. Guffey, "Prediction of flowing bottomhole pressures in gas wells," in *Proceedings of the SPE Gas Technology Symposium*, Dallas, Tex, USA, June 1989.
- [12] J. Chen and X. Yue, "Pressure gradient of gas liquid mixture in pumping well," *Journal of Daqing. Petroleum Institute*, vol. 4, pp. 31–39, 1985.
- [13] R. D. Oden and J. W. Jennings, "Modification of the cullender and smith equation for more accurate bottomhole pressure calculations in gas wells," *Society of Petroleum Engineers*, vol. 10, no. 11, 1988.
- [14] A. R. Hasan and C. S. Kabir, "Study of multiphase flow behavior in vertical wells," *SPE Production Engineering*, vol. 3, no. 2, pp. 263–272, 1988.
- [15] X. Liu, Y. Qi, C. Liu, Y. Li, and P. Zhao, "Prediction of flowing bottomhole pressures for two-phase coalbed methane wells," *Acta Petrolei Sinica*, vol. 31, no. 6, pp. 998–1003, 2010.
- [16] H. D. Beggs and J. R. Brill, "Study of two-phase flow in inclined pipes," *Journal of Petroleum Technology*, vol. 25, pp. 607–617, 1973.
- [17] L. Wei, Y. Liu, and Z. Ren, "Node parameter calculation method of oil and gas gathering pipeline network," *Journal of Daqing Petroleum Institute*, vol. 27, no. 4, pp. 79–83, 2003.
- [18] T. Gentzis and D. Bolen, "The use of numerical simulation in predicting coalbed methane producibility from the gates coals, alberta inner foothills, canada: comparison with mannville coal CBM production in the Alberta Syncline," *International Journal of Coal Geology*, vol. 74, no. 3-4, pp. 215–236, 2008.
- [19] C. Yang and Y. Sang, "Application of material balance method in coalbed gas well productivity forecast," *Drilling and Production Technology*, vol. 23, no. 4, pp. 33–37, 2000.
- [20] G. R. King, "Material balance techniques for coal seam and Devonian shale gas reservoirs," in *Proceedings of the SPE Annual Technical Conference and Exhibition*, pp. 181–192, New Orleans, La, USA, September 1990.
- [21] I. Palmer and J. Mansoori, "How permeability depends on stress and pore pressure in coalbeds: a new model," in *Proceedings of the SPE Annual Technical Conference and Exhibition*, pp. 557–565, December 1998.
- [22] A. Corey and C. Rathjens, "Effect of stratification on relative permeability," *Journal of Petroleum Technology*, vol. 8, no. 12, pp. 69–71, 2013.
- [23] J. Yang, Y. Wang, and Z. Chen, "Computation of bottom hole flowing pressure (WBHP) and analysis of influencing factors in coalbed methane well," in *Proceedings of the Coalbed Methane Conference*, pp. 370–377, Beijing, China, 2008.

Research Article

Route Optimization of Pipeline in Gas-Liquid Two-Phase Flow Based on Genetic Algorithm

Jun Zhou,¹ Guangchuan Liang,¹ Tao Deng,² and Jing Gong³

¹Southwest Petroleum University, Chengdu 610500, China

²China National Petroleum Corporation Guangzhou Petroleum Training Center, Guangzhou 510510, China

³China University of Petroleum (Beijing), Beijing 102249, China

Correspondence should be addressed to Jun Zhou; 201599010096@swpu.edu.cn and Guangchuan Liang; lgcdjr@163.com

Received 23 October 2016; Accepted 13 December 2016; Published 19 January 2017

Academic Editor: Jose Alberto Romagnoli

Copyright © 2017 Jun Zhou et al. This is an open access article distributed under the Creative Commons Attribution License, which permits unrestricted use, distribution, and reproduction in any medium, provided the original work is properly cited.

This paper describes the problems in route optimization of two-phase pipelines. Combining the hydraulic calculation with route optimization theory, this paper establishes an automatic route optimization model and adopts the general genetic algorithm (gGA) and steady-state genetic algorithm (ssGA) to solve the model, respectively, gets the optimal route, and discusses the influence of parameters setting to the result. This algorithm was applied in determining pipelines routes in coalbed methane gathering and transporting system in Shanxi Province, China. The result shows that the algorithm is feasible, which improves the hydraulic properties by reducing the pressure drop along the line while the pipeline length is still acceptable.

1. Introduction

In a recent decade, to meet the constant need of energy, although the global economy has come through a downturn, the oil-gas pipelines construction is still prosperous around the world. In 2013, the total length of pipelines under construction or planned to be constructed is about 188,108 km, and the length of those under construction is 53,180 km, 11.4% longer than that in the year 2012, 47,732 km. During the construction, the first step is to determine the pipeline route. The task is frequent and time-consuming and plenty of attempts have been made. Traditionally engineers would determine the route manually on a printed map or solve the problem with optimization theory. Early in the year 1971, Shamir [1] used dynamic programming to determine the optimal route on manual mesh. In years 2004 and 2012, Meisingset et al. [2] and Marcoulaki et al. [3] established the mathematical optimization models in terms of minimum investment separately for submarine pipelines and ground pipelines and solved the models with simulated annealing, but those models did not involve the hydraulic properties.

In the problem of oil-gas pipeline route optimization, pipe flow may be single-phase or multiphase. Multiphase pipe flow

is different from single-phase pipe flow; the pressure drop is closely related to the height along the line. Both uphill section and downhill section can be energy-consuming, yet the energy loss in the uphill section cannot be replenished by the gravity effect of downhill section. Thus with the same starting/ending location and pipeline length, but different routes and different topographic reliefs, different pipelines possess different hydraulic properties. In literature, Xiao et al. [4] used A^* algorithm to study the optimal route of gas-liquid two-phase flow pipeline, yet A^* algorithm is not a global optimization algorithm, which is based on a combined algorithm between Dijkstra's algorithm and Best-First-Search algorithm. In this paper, the authors would use a global optimization algorithm-genetic algorithm (GA) to discuss the optimal route programming of gas-liquid two-phase flow pipelines.

2. Gas-Liquid Two-Phase Pipe Flow

In oil-gas field, people would usually use one pipeline to transport the product of several wells. As long as two-phase flow exists in the pipeline, the pipeline is defined as two-phase pipeline. In an oil-gas mixture transportation pipeline, the oil-gas ratio may vary a lot in different parts. In drainage

pipes of oil-gas separators, the flowing liquid is basically crude oil, but along the pressure drop some dissolved gas would come out. In venting pipes of oil-gas separators, the flow inside is basically natural gas, yet along the flowing there may be water or heavy hydrocarbon condensated. For example, in the coalbed methane gas fields which are largely exploited, the gas came out from the well; along the gas flow there would be water condensation; then gas-liquid two-phase flow would appear. At the same time, in gathering and transporting process, it is not economic to use two pipelines separately transporting crude oil and natural gas in small quantities. Thus in the surface gathering and transporting system, mixture transportation pipelines are widely used. Moreover, in some specific conditions, mixture transportation has some advantages that single-phase pipeline cannot compare with. For instance, in some places that are not suitable for installing gas-liquid separators and processing facilities (such as urban areas, deserts, lakes, ecological reserves, and swamplands), mixture transportation pipelines are necessary. Those pipelines tend to go through hills or mountainous areas, which does not cause any problems when the pipelines are single-phase, because the pressure energy loss during uphill section would be replenished during downhill section. Yet in two-phase flow the situation is much different. Since the liquid holdup and the density of the gas-liquid mixture in downhill section are much smaller than those in uphill section, the pressure cannot be regained that much in downhill section. Therefore, as far as multiphase pipeline route determination is concerned, engineers must give high priority to the hydraulic properties of the pipe flow and combine it with the route optimization.

The distribution of gas and liquid in the two-phase pipe flow varies a lot, and flow patterns vary a lot too. These would influence not only the mechanical relationship of the two-phase flow but also the heat and mass transfer; thus the gas-liquid two-phase flow is very complicated. Currently there are plenty of calculation models of gas-liquid two-phase flow with their own advantages and disadvantages. Yet the research of two-phase models goes beyond our study in the paper. This paper plans to use existing gas-liquid two-phase Beggs-Brill [5] model to integrate hydraulic simulation with route optimization algorithm.

3. Optimization

Route determination involves many aspects, such as like pipeline's design, construction, operation, and maintenance, which include the security of the pipeline, hydraulic and thermal conditions, environmental conservation, historical sites, soil and hydrological conditions, and construction requirements. For route optimization based on intelligence algorithm, the route programming of oil-gas pipelines mainly deals with the following factors: oil-gas production; oil-gas physical properties; the starting point and terminal of the pipeline; the starting and ending pressure of the pipeline; the areas that the pipeline goes through; heights of different places; land types (rocky soil, sandy soil, etc.); forest covered

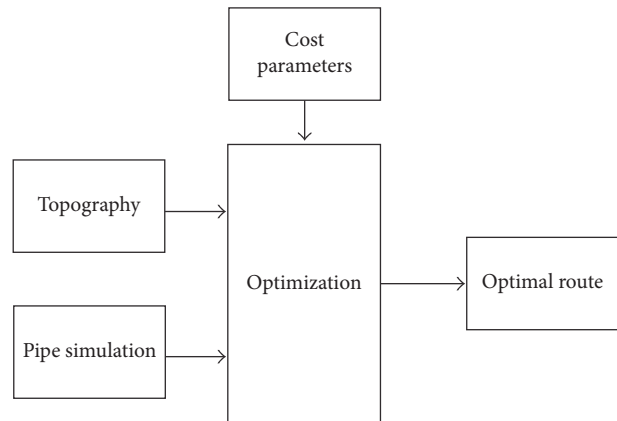


FIGURE 1: Optimization tools.

area; source of water, rivers, roads, railroads, and impenetrable areas. The material and labor costs of pipeline construction; the pipes; regional regulation; constructing techniques; construction goal (usually minimum investment); and other factors influencing the pipeline construction.

We need to find the pipeline route from the starting point to the terminal, satisfy the gas-liquid two-phase flow characters and other constraint conditions, and then make the object function minimum. This paper focuses on the two-phase pipeline route on complex topography, using digital topographical data to decide the optimal route. The overview of the optimization tool is shown in Figure 1.

3.1. Topographical Data

Digital Map. Automatic route optimization is carried out on digital maps, using discrete data (see Figure 2) to represent the continuous surface. Discrete data is the approximation of continuous surface. The higher the resolution is, the closer the approximation is to the real topography and the more accurate the route tracing is. Yet there is a highest resolution limitation. This form has a good compatibility and is consistent with the grid data of GIS (Geographic Information System).

3.2. Algorithm. On the issue of shortest route, the researchers studied several intelligence algorithms [6–8]. Among them, genetic algorithm was established simulating Darwin's evolution theory, which can be used to solve the problems of function optimization or machine learning. It imitates the procedure of inheritance and evolution, that is, selection, replication, crossover, and variation, and introduces the concept of "survival of the fittest" into the algorithm. The block diagram of genetic algorithm is shown in Figure 3.

To carry out the hydraulic calculation of gas-liquid two-phase pipeline, we adopt the method of segmentation to calculate the pressure drop of different sections one by one.

The symbol of discretization is shown in Figure 4. The starting point is N_0 , ending point is N_n , and the nodes divide the pipeline into many sections. The starting and ending points of pipe section j are N_j and N_{j+1} . If only hydraulic

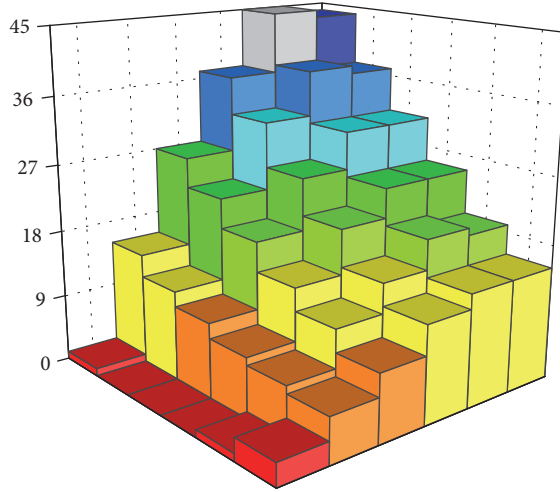


FIGURE 2: Topographical sample (approximately showing real topography).

1	15	27	37	45	44
0	12	23	32	38	37
0	10	19	26	31	31
0	8	15	21	25	25
1	7	12	16	20	19
3	6	9	13	15	15

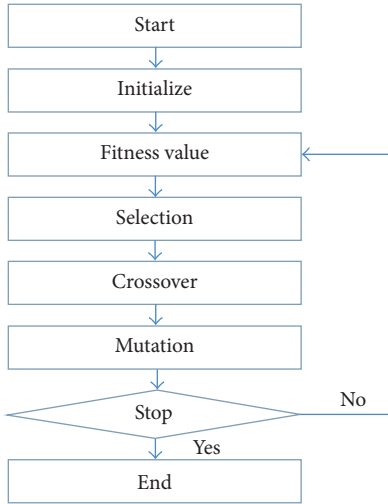


FIGURE 3: The block diagram of genetic algorithm.

calculation is conducted, it means to do hydraulic simulation on a determined route and to manually set the mesh spacing (usually equal mesh spacing). However, in three dimensions, the route is not determined. Therefore at the same time with route optimization, hydraulic calculation must be taken into consideration.

During the optimization, each route represents a pipeline. The nodes on the route divide the pipeline into pipe sections with different lengths, as shown in Figure 5. Calculation accuracy can be guaranteed when the mesh spacing is small enough.

In route optimization, assuming that there is a ground area with limited boundaries, starting point is A (x_0, y_0, z_0) and ending point is B (x_n, y_n, z_n) . There are many routes going from A to B. Assuming that the investment of pipeline is proportional to the pipeline length, the route optimization is to find a route that can minimize the construction investment or optimize other object functions.

The initial population contains m routes; the route i in generation k is expressed as

$$r_k^i = \{(x_{k0}^i, y_{k0}^i, z_{k0}^i), (x_{k1}^i, y_{k1}^i, z_{k1}^i) \dots (x_{k(n-1)}^i, y_{k(n-1)}^i, z_{k(n-1)}^i), (x_{kn}^i, y_{kn}^i, z_{kn}^i)\}. \quad (1)$$

The length of route i in generation k is expressed as

$$L_k^i = \|r_k^i\| = \sum_{j=0}^{n-1} \sqrt{(x_{k(j+1)}^i - x_{kj}^i)^2 + (y_{k(j+1)}^i - y_{kj}^i)^2 + (z_{k(j+1)}^i - z_{kj}^i)^2}. \quad (2)$$

Taking hydraulic conditions into consideration, we have the following.

The pressure drop between adjacent nodes is dp_{kj}^i , so the pressure drop along the route i in generation k is expressed as

$$DP_k^i = \sum_{j=0}^{n-1} dp_{kj}^i \sqrt{(x_{k(j+1)}^i - x_{kj}^i)^2 + (y_{k(j+1)}^i - y_{kj}^i)^2 + (z_{k(j+1)}^i - z_{kj}^i)^2}. \quad (3)$$

Pressure drop dp_{kj}^i can be calculated by many methods. Fitness function is expressed as

$$\text{Fitness}_k^i = \frac{1}{DP_k^i}. \quad (4)$$

Due to the grid data, in genetic algorithm we use integer coding, roulette wheel selection, single-point crossover, and single-point variation for calculation; repeat the procedure in Figure 3 till the best individual is found.

3.3. Realization. Due to the complexity of terrain pipeline optimization, it is often unable to obtain the best path. As we all know, under the plane condition, straight line between two points is the shortest [9]. To test the program, we first optimize the shortest path between two points on the plane.

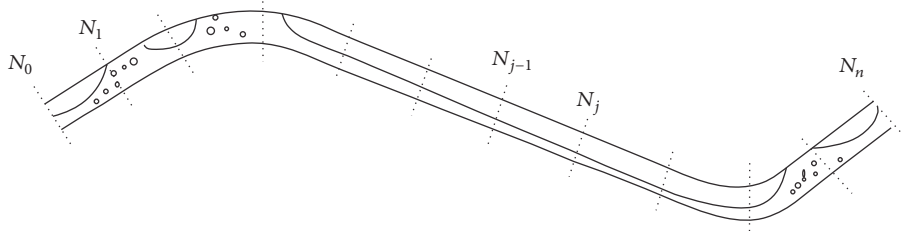


FIGURE 4: Discretization sketch of gas-liquid two-phase pipeline.

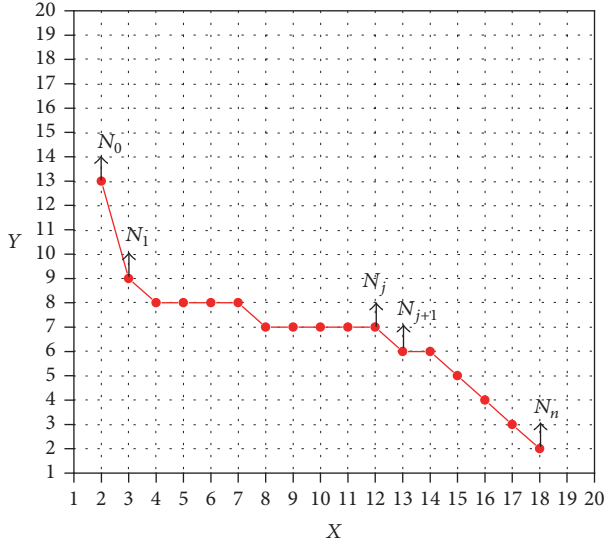


FIGURE 5: Discretization sketch of pipeline route.

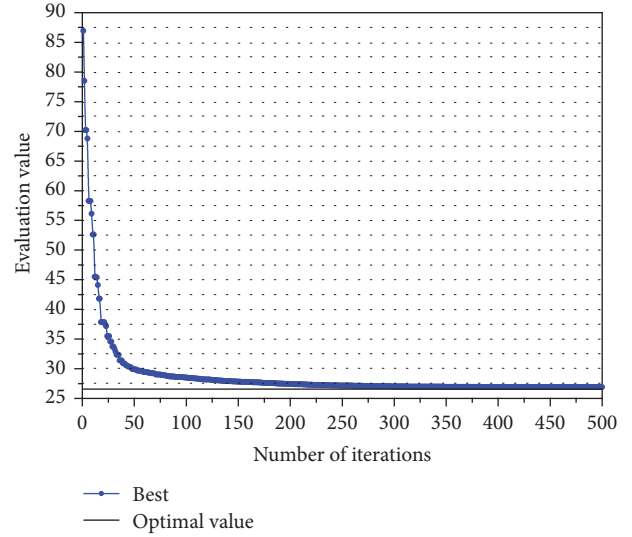


FIGURE 6: Performance of the GA in finding the best solution.

Supposing the population size and the maximum number of iterations are 200 and 1000, respectively, crossover probability and mutation probability are 0.95 and 0.2, respectively. Figure 6 shows the algorithm convergence; as can be seen from the figure, the algorithm converges quickly and approaches the best solution after 250 iterations. Figure 7 shows the path graphs under different generations, and the path approaches a straight line between two points after 500 iterations.

3.4. Test Results and Discussion. General and steady-state genetic algorithms with roulette wheel selection, arithmetic crossover, and uniform mutation are adopted. The computer is Samsung R408, Intel Pentium dual T3400, 2.16 Hz, 1 G RAM.

Generate the digital map with topographical model function.

$$z(x, y) = \sum_{i=1}^h h_i \times \exp \left\{ - \left(\frac{|x - x_{ci}|}{u_i} \right)^{p_i} - \left(\frac{|y - y_{ci}|}{v_i} \right)^{q_i} \right\}. \quad (5)$$

Parameters of topographical function are shown in Table 1.

TABLE 1: Parameters of topographical function.

i	x_c	y_c	p	q	u	v	h
1	25	87	1.5	1.5	30	20	57
2	64	28	2	3.5	65	12	19
3	34	53	3	2	21	13	-32
4	77	92	2	2	6	25	38
5	94	55	3	3	11	14	24
6	65	24	1.5	1.5	13	9	-22
7	15	11	3	2	11	16	-14
8	93	14	3	3	13	11	-17

Here is the route programming of complex topography with grid data. The example digital map is in Figure 8. Mesh number is 20×20 and mesh size is 5×5 .

For genetic algorithms, crossover probability (CP) and mutation probability (MP) are extremely important parameters, which directly affect the optimization quality of the algorithm. In this paper, to analysis the sensitivity of the two GAs to the parameters, CP ranges from 0.4 to 1.0 and MP ranges from 0.0005 to 0.3. Figure 9 shows the averages results of ten independent operations at different probabilities. Two genetic algorithms are sensitive to CP and MP. Both of them

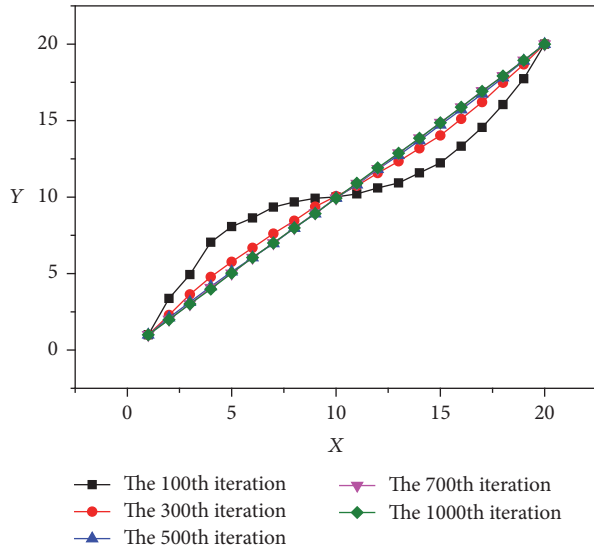


FIGURE 7: Routes sketch of different generations in optimization.

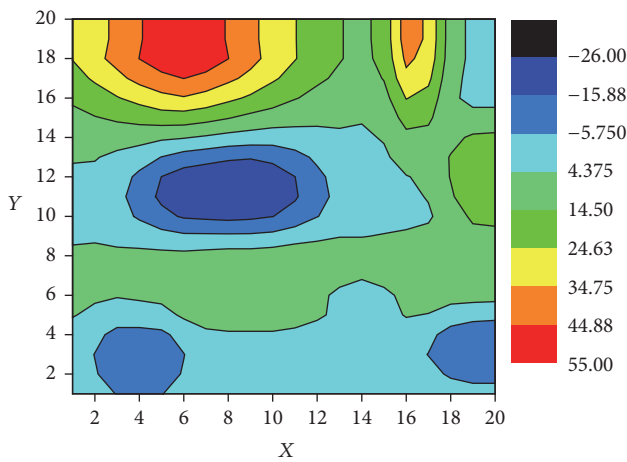


FIGURE 8: Digital profile of topographical surface.

TABLE 2: Best result obtained from ssGA and gGA.

	GN GA	SS GA
CP, MP	0.9, 0.005	1.0, 0.1
Average evaluation value (over ten times)	172.19	173.09
Best evaluation value (over ten times)	163.18	167.34

can obtain best function evaluation values when CP is big. Yet the MP of GN GA is small but that of SS GA is big.

The optimal results of two GA are shown in Table 2. The average and best result of GN GA both are a little smaller than those of SS GA. The best evaluation value is 163.18. In Figure 10, the red curve is optimal route and it bypasses the low areas in the middle.

TABLE 3: Parameter of pipeline simulation.

Parameter	Parameter value
Volume flow rate of gas, m ³ /d	4000
Volume flow rate of liquid, m ³ /d	0.3
Starting pressure, MPa	1.5
Pipe diameter, m	0.2

TABLE 4: Calculation results.

	Real value	Calculation result
Pipeline length	5433.804 m	5570.194 m
Pipeline pressure drop	1.021 MPa	0.644 MPa

4. Example Analysis

The existing pipeline data and simulation parameter is shown in Table 3.

The calculation model of gas-liquid two-phase pipe flow is Beggs-Brill [8] model to calculate liquid holdup and pressure drop. For more detailed information of the model, please refer to Appendix A.

The topographical data comes from digital map, whose file format is TIF shown in Figure 11 and the pixel size in grid information is 21 m × 136.21 m. The elevation model of this block (red box in Figure 11) is shown in Figure 12, with an area of 27.5625 km² and mesh number of 250 × 250.

In Figure 12, point A is the starting point, point B the ending point, and dotted line the existing pipeline. It is obvious in the figure that the line passes through high mountains in the middle. With the model in this paper we can get the optimal route represented by solid line. From the starting point, the line goes down and bypasses the hills to the ending point. The route under three-dimension topography is shown in Figure 13.

The calculation results are presented in Table 4. Table 4 lists out the pipeline length and pressure drop of both optimal route and real route. From Figures 14 and 15, the variation of existing pipeline elevation is big while the optimal pipeline elevation goes gently. Pipeline length increased to 5570.194 m from 5433.804 m by 2.45%, yet which is still acceptable, and the pressure drop along the line reduced to 0.644 MPa from 1.021 MPa by 36.92%. This greatly improves the hydraulic properties of the pipeline.

5. Conclusions

- (1) This paper establishes a pipeline route determination model combined hydraulic calculation in complex topography. With the digital topographical data, the optimal route can be automatically determined.
- (2) Genetic algorithm can be used to select an optimal route for gas-liquid two-phase pipeline. The parameters of genetic algorithm would have an influence on optimization result. If topographical data and pipeline parameters are known, with a program the optimal

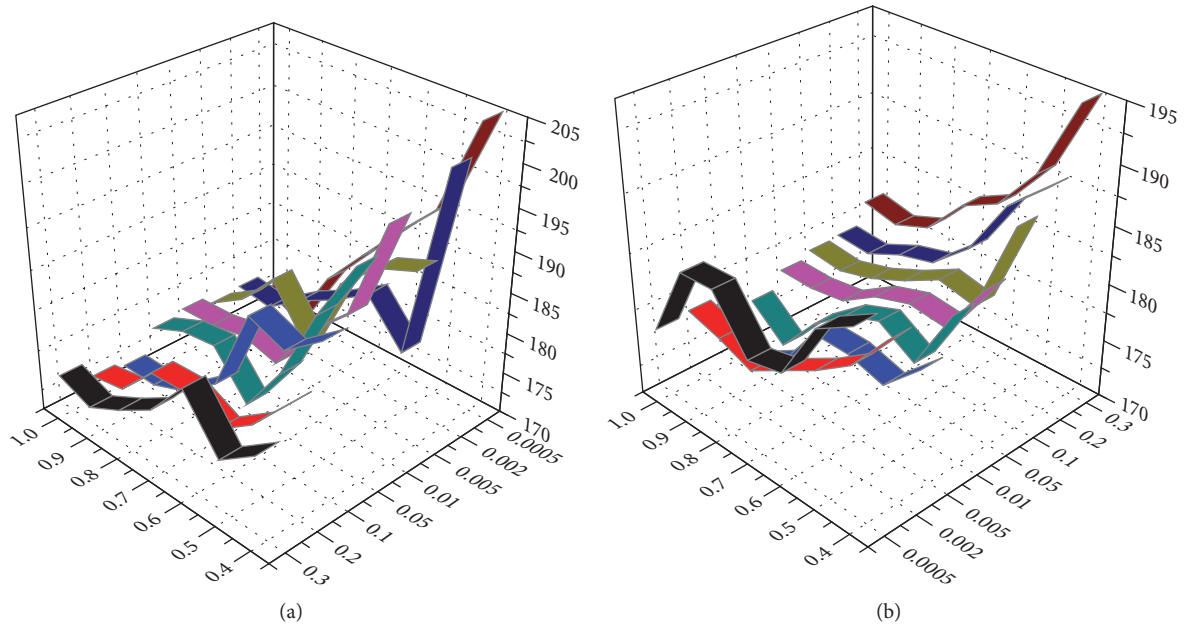


FIGURE 9: Effect of variations of CP and MP on the performance of gGA (a) and ssGA (b).

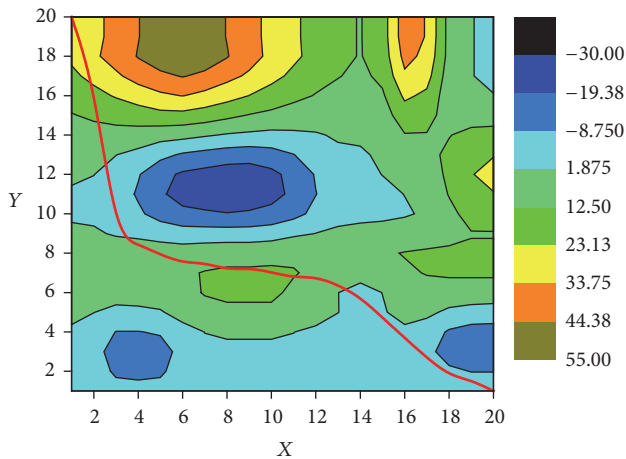


FIGURE 10: Result of route curves.

route can be determined. As the example in paper, this method can reliably seek out the route.

- (3) This paper gives a structure of pipeline route design. It is a reference for the engineers. They can add other expenses according to the real situation.

Appendix

A. Beggs-Brill Liquid Holdup Relative Expression

Beggs-Brill relative expression (BB relative expression) can be used to calculate the liquid holdup. When dip angle $\theta = 0$, the calculation result is the liquid holdup of horizontal pipes; when $\theta \neq 0$, the result is the liquid holdup of inclined pipes, which has a correction factor.

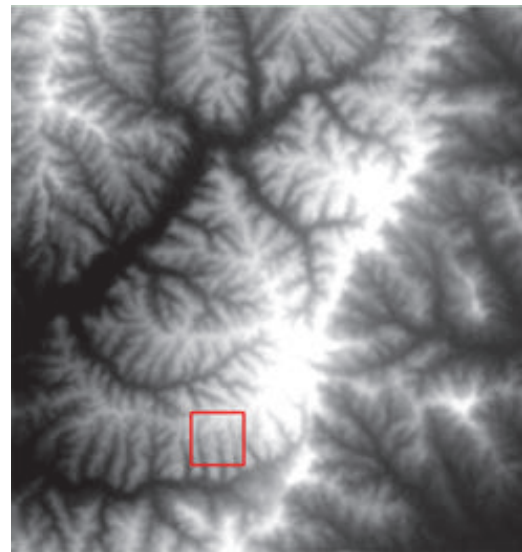


FIGURE 11: Topography file in TIF of some block.

Before calculating liquid holdup, first identify flow pattern, and Table 5 presents the rules of flow pattern identification.

The equation to calculate liquid holdup of horizontal pipe is

$$H_L(0) = \frac{aR_L^b}{Fr^c}$$

$$R_L = \frac{Q_l}{Q_l + Q_g} \tag{A.1}$$

$$Fr = \frac{w^2}{gd}$$

TABLE 5: Rules of flow pattern identification.

Flow pattern	Identification rules		Calculating method of L
	R_L	Fr	
Separated flow	<0.01	$<L_1$	$L_1 = 316 \times R_L^{0.302}$ $L_2 = 9.252 \times 10^{-4} \times R_L^{-2.4684}$ $L_3 = 0.01 \times R_L^{1.4516}$ $L_4 = 0.5 \times R_L^{6.738}$
	≥ 0.01	$<L_2$	
Transition flow	≥ 0.01	$>L_2 \ \& \ <L_3$	
Intermittent flow	$\geq 0.01 \ \& \ <0.4$	$>L_2 \ \& \ <L_1$	
	≥ 0.4	$>L_3 \ \& \ \leq L_4$	
Dispersion flow	<0.4	$\geq L_1$	
	≥ 0.4	$>L_4$	

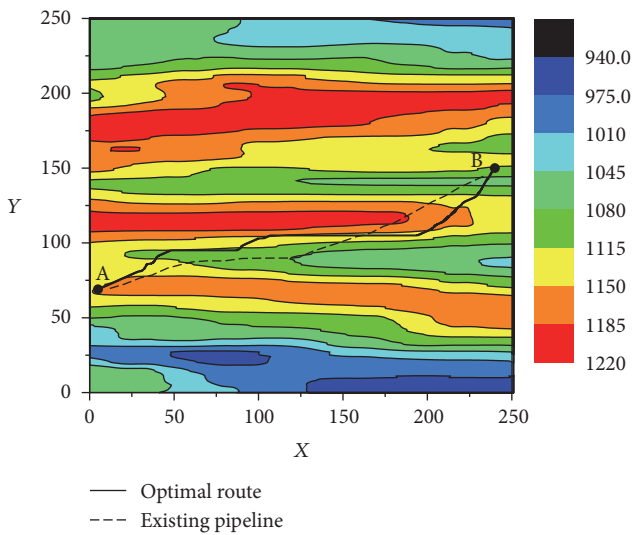


FIGURE 12: Pipeline route in contour map.

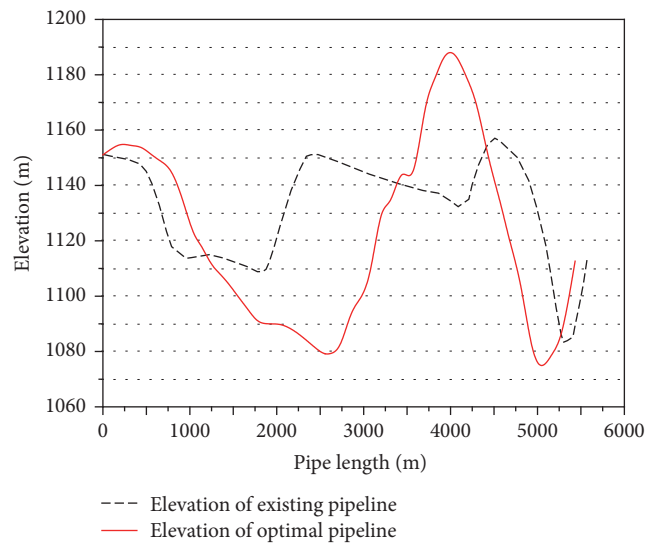


FIGURE 14: Elevation along the line.

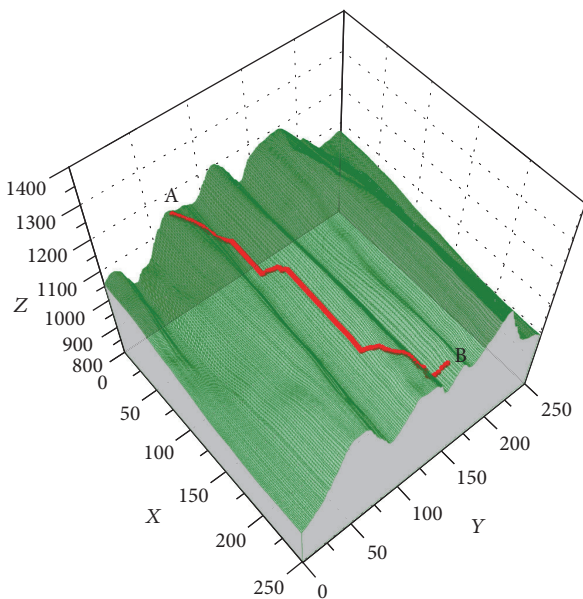


FIGURE 13: Pipeline route in 3D topographical map.

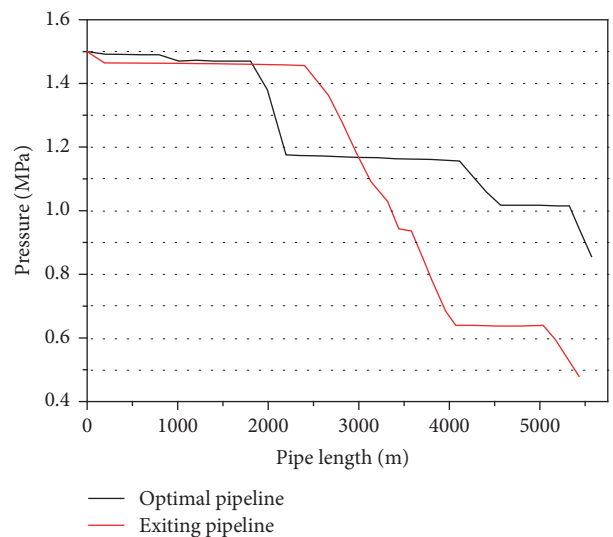


FIGURE 15: Pressure along the line.

TABLE 6: Different coefficient of a , b , and c .

Flow pattern	a	b	c
Separated flow	0.980	0.4846	0.0868
Intermittent flow	0.845	0.5351	0.0173
Dispersion flow	1.065	0.5824	0.0609

TABLE 7: Coefficient values.

Flow pattern	d	e	f	g
Uphill separated flow	0.011	-3.768	3.539	-1.614
Uphill intermittent flow	2.96	0.305	-0.4473	0.0978
Uphill dispersion flow		$C = 0$	$\phi = 1$	
Downhill flow	4.70	-0.3692	0.1244	-0.5056

In the equation, R_L is volume liquid holdup and Fr is Froude dimensionless number.

With different flow pattern, we use different coefficient to calculate a , b , and c . The results are listed in Table 6.

Correction factor is

$$\varphi = 1 + C \left[\sin(1.8\theta) - \frac{1}{3} \sin^3(1.8\theta) \right]. \quad (\text{A.2})$$

When $\theta = 90^\circ$,

$$C = (1 - R_L) \ln(dR_L^e N_{Lw}^f Fr^g) \quad (\text{A.3})$$

$$N_{Lw} = W_{sL} \left(\frac{\rho_L}{g\sigma} \right)^{0.25}$$

In the equation, N_{Lw} is liquid apparent velocity index.

The coefficients d , e , f , and g depend on flow patterns, as shown in Table 7.

The correction factor ϕ represents the liquid holdup ratio of inclined pipe to horizontal pipe:

$$\phi = \frac{H_L(\theta)}{H_L(0)}. \quad (\text{A.4})$$

B. Beggs-Brill Pressure Drop Relative Expression

B.1. Pressure Drop Gradient Calculating.

$$-\frac{dp}{dl} = \frac{[H_L \rho_L + (1 - H_L) \rho_G] g \sin \theta + \lambda (2wM/\pi d^3)}{1 - [H_L \rho_L + (1 - H_L) \rho_G] w w_{sg}/p} \quad (\text{B.1})$$

In the equation, H_L is liquid holdup, dimensionless; p is average absolute pressure of flow in the pipe, Pa is λ -hydraulic friction coefficient of gas-liquid mixed pipeline, dimensionless; ρ_g is density of gas and liquid, kg/m^3 ; M is mass flow rate of the gas-liquid mixture, kg/s ; w is the flow

velocity of gas-liquid mixture, m/s ; w_{sg} is apparent velocity of gas, m/s ; d is inner diameter of pipes, m ; and θ is dip angle, degree.

Among all those calculating methods of gas-liquid mixture transportation pipeline with topographic relief, BB pressure drop calculating method is the only one taking downhill energy recovery into consideration. If liquid holdup equals 1 or 0, the method turns into calculating single-phase liquid or gas pipeline.

B.2. Laws of Two-Phase Hydraulic Friction Coefficient. Assuming hydraulic friction coefficient of homogeneous flow is λ_0 , the hydraulic friction coefficient ratio of two-phase flow to homogeneous flow is λ/λ_0 .

$$\left(\frac{\lambda}{\lambda_0} \right) = e^n$$

$$m = \frac{R_L}{[H_L(\theta)]} \quad (\text{B.2})$$

$$n = \frac{-\ln m}{0.0523 - 3.182 \ln m + 0.8725 (\ln m)^2 - 0.01853 (\ln m)^4}$$

When $1 < m < 1.2$, $n = \ln(2.2m - 1.2)$.

For hydraulically smooth pipes, the hydraulic friction coefficient of homogeneous flow is λ_0 , which can be looked up in Moody graph or calculated by the following equations:

$$\lambda_0 = \left[2 \lg \left(\frac{\text{Re}_0}{4.5223 \lg \text{Re}_0 - 3.8215} \right) \right]^{-2} \quad (\text{B.3})$$

$$\text{Re}_0 = \frac{dw\rho_f}{\mu} = \frac{dw [\rho_L R_L + \rho_g (1 - R_L)]}{[\mu_L R_L + \mu_g (1 - R_L)]}$$

Figure 16 is the program chart of BB method to get pressure drop.

Nomenclature

- i : Route number in genetic algorithm
- j : Pipe section number
- k : Generation k in genetic algorithm
- N_j : Node number
- (x_j, y_j) : The coordinates of node N_j
- z_j : The elevation of node N_j
- r_k^i : Nodes set of the route i in generation k
- L_k^i : Length of route i in generation k
- DP_k^i : The pressure drop along the route i in generation k
- dp_{kj}^i : The pressure drop along pipe section j between nodes N_j and N_{j+1} .

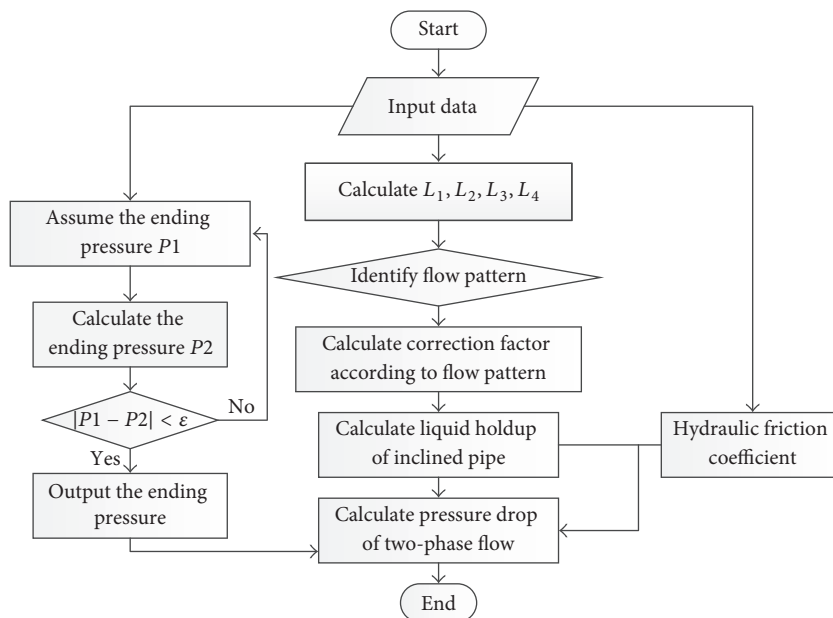


FIGURE 16: The program chart of BB method.

Competing Interests

The authors declare that they have no competing interests.

Acknowledgments

The authors appreciate the financial support from the Young Scholars Development Fund of SWPU (201599010096).

References

- [1] U. Shamir, "Optimal route for pipelines in two-phase flow," *Society of Petroleum Engineers Journal*, vol. 11, no. 03, pp. 215–222, 1971.
- [2] H. Meisingset, J. Hove, and G. Olsen, "Optimization of pipeline routes," in *Proceedings of the 14th International Offshore and Polar Engineering Conference*, Toulon, France, May 2004.
- [3] E. C. Marcoulaki, I. A. Papazoglou, and N. Pixopoulou, "Integrated framework for the design of pipeline systems using stochastic optimisation and GIS tools," *Chemical Engineering Research and Design*, vol. 90, no. 12, pp. 2209–2222, 2012.
- [4] J. J. Xiao, A. J. Al-Muraikhi, and A. M. Qahtani, "Automated route finding for production flowline to minimize liquid inventory and pressure loss," in *Proceedings of the SPE Annual Technical Conference and Exhibition (ATCE '06)*, Texas, USA, September 2006.
- [5] D. H. Beggs and J. P. Brill, "A experimental study of two-phase flow in inclined pipes," *Journal of Petroleum Technology*, vol. 25, no. 5, pp. 607–617, 1973.
- [6] Z. Huang, S. Chen, L. Kang, and Y. Chen, "Solving the shortest path on curved surface based on simulated annealing algorithm," *Journal Wuhan University*, vol. 46, no. 3, pp. 273–276, 2000.
- [7] D. D. Yang and R. Ran, "Genetic algorithm based shortest path planning on curved surface," *Computer Simulation*, vol. 23, no. 8, pp. 168–169, 2006.
- [8] J. Y. Luo, "The study on PSO algorithm to seek shortest path on curved surface," *Journal of Min Jiang University*, vol. 25, no. 5, pp. 14–17, 2007.
- [9] J. Zhou, X. Li, T. Deng, M. Cheng, and J. Gong, "Layout optimization of branch pipeline network on curved surface using genetic algorithm," in *Proceedings of the 10th International Pipeline Conference (IPC '14)*, Calgary, Canada, October 2014.

Research Article

Numerical Simulation on Structure Optimization of Liquid-Gas Cylindrical Cyclone Separator

Peng Chang,¹ Tian Hu,¹ Li Wang,² Sen Chang,² Tianjing Wang,¹ and Yueshe Wang¹

¹State Key Laboratory of Multiphase Flow in Power Engineering, Xi'an Jiaotong University, Xi'an, China

²No. 5 Natural Gas Production Plant, PetroChina Changqing Oilfield Company, Inner Mongolia, China

Correspondence should be addressed to Yueshe Wang; wangys@mail.xjtu.edu.cn

Received 1 July 2016; Revised 16 August 2016; Accepted 22 August 2016

Academic Editor: Evangelos Tsotsas

Copyright © 2016 Peng Chang et al. This is an open access article distributed under the Creative Commons Attribution License, which permits unrestricted use, distribution, and reproduction in any medium, provided the original work is properly cited.

With the further development of oilfield, liquid-gas separation has become an essential problem. Cylindrical cyclone separators are popular in the industrial process due to the advantage that they are simple, compact, and inexpensive to manufacture. In this paper, a three-dimensional turbulence model including Reynolds stress model was established to describe the mixture flow field in the separator. Through the numerical simulation, the separation efficiency was investigated under different parameter cases such as separator length, gas phase outlet diameter, and inlet shape. It can be indicated from the simulation results that the separation efficiency decreases with the increase of the separator length, and the separation efficiency increases firstly and then decreases with the increase of the gas phase outlet diameter as well as the liquid phase outlet. Furthermore, the rectangular inlet is more suitable than the circular inlet with the separation efficiency changing from 66.45% to 79.04%. In the end, the optimal geometrical structure was presented with separation efficiency of 86.15%.

1. Introduction

For the past several decades, conventional gravity based separators, such as settling tanks, have been extensively used in industries. Therefore, they are bulky and expensive and show slow separation. Due to these defects, in recent years, the industry has shown keen interest in the development and application of alternatives to the conventional separators. One of such alternatives is the cylindrical cyclone separator (CCS). Unlike the slow settling of particles within a settling tank, a cyclone separator shows fast separation and utilizes less space. It is simply a cylinder installed with a downward inclined tangential inlet and two outlets provided at the top and the bottom, respectively. It operates under the action of centrifugal forces, without any internal moving devices. Fluid mixture enters in the cyclone and makes a swirl motion; because of the centrifugal force, the dense phase of the mixture gains a relative motion in the radial direction and is separated from the mixture. The CCS utilizes the energy obtained from the fluid pressure gradient to create rotational fluid motion instead of using electricity and other types of

energy, which leads to relative economy in power usage and flexibility.

The CCS has a variety of potential applications, varying from partial separation to complete separation. It is widely used in industrial processes for separation of dust from gas streams or for product recovery. Potential applications include control of gas/liquid ratio of multiphase flow, portable well test metering, and pre-separation upstream of slug catchers [1]. Nowadays, the CCS plays a key role in multiphase flow metering loop. In this area, gas and liquid phases are separated in the CCS. Each of the separated phases is metered by a single-phase flow meter installed in the outlets of the CCS, respectively. After metering, the gas and liquid phases are recombined downstream of the meters to recover two-phase flow. Despite its simplicity, the disadvantage of this separator is that the pressure drop and mixture pressure of inlet are high compared with traditional settling chambers.

In order to improve the separating process, primarily, we should understand the fluid dynamics of this separator, such as vorticity and annular zones of reverse flow. Reydon and Gauvin [2] studied the behavior of confined

vortex flow in conical cyclones. Kouba et al. [3] presented experimental results for air-water system and the effect of inlet inclination angle, operating pressure, and body and inlet geometry on liquid carry-over phenomenon for gas-liquid cylindrical separators. Davies and Watson [4] carried out a study, indicating size, cost, and performance benefits of a modified cyclone over a conventional separator in offshore applications. Gomez et al. [5] proposed a mechanistic model to predict the hydrodynamic flow behavior in a CCS. Four typical systems were designed for actual industrial application, including multiphase metering loop with both single-phase and multiphase flow meters, pre-separation, and full-separation configurations. Arpandi et al. [6] presented new experimental data and an improved mechanism to predict the hydrodynamic flow behavior in the CCS, including the operational envelope, equilibrium liquid level, vortex shape, velocity, and holdup distributions. Hreiz et al. [7] carried out an experiment to study the effect of inlet nozzle design on the performance of the CCS. Theories of confined vortex flow have so far been unable to predict many features of the flow fields observed due to strongly coupled, nonlinear partial differential equations of mass and momentum conservation involved in the fluid dynamics.

With the development of powerful digital computers, this problem can be solved by computational fluid dynamics (CFD). It subdivides the solution domain into a large number of control volumes and converts the partial differential equations by integration over these control volumes into their algebraic equivalents. Boysan et al. [8] presented one of the first CFD models of CCS, showing that the standard $k-\epsilon$ turbulence model cannot be used for simulating flows with swirl, because it may result in excessive turbulence viscosities and unrealistic tangential velocities. Hoekstra et al. [9] suggested that Reynolds stress model (RSM) can solve the anisotropic turbulence problem, which has been widely used for cyclones and the corresponding numerical simulation in recent studies. Wang et al. [10] presented a numerical study of the gas-powder-liquid flow in a hydrocyclone with the Reynolds stress model, which was verified by the measured results. In recent years, the so-called combined approach of discrete element method (DEM) and CFD (CFD-DEM) has been developed and accounts for both particle-particle and particle-fluid interactions. The CFD-DEM approach has proven to be effective in modeling various particle-fluid flow systems. Chu et al. [11] presented a mathematical model to describe the flow characteristics in dense medium cyclones by means of combining DEM with CFD. The DEM is used to model the motion of discrete particles and the CFD is used to model the motion of discrete particles.

CFD provides an economical means of understanding the complex fluid dynamics and how they are affected by changes in both design and operating conditions. Various CCS have been presented in previous literatures. Crowe and Pratt [12] developed a two-dimensional (2D) model to predict the increase of the overall collection efficiency with solid loading ratio. Movafaghian et al. [13] studied experimentally and theoretically the hydrodynamic flow behavior in CCS. The parameters of this investigation include three different inlet geometries, four different liquid viscosities, three system

pressures, and the effect of surfactant. Erdal et al. [14] presented a 2D model of single-phase and two-phase flow in several CCS configurations. Results are also compared with experimental data including tangential velocity profiles and tangential velocity decay, showing good agreement. In fact, if the inlet is ignored, CCS can be considered as symmetric and CFD models can be simplified to a two-dimensional case. Although this method can greatly reduce computational time, it cannot be used to assess changes in inlet design or offset vortex finders. With the development of computer, recent CFD models mostly use full three-dimensional shape to explore flow characteristics in CCS.

Minier and Simonin [15] used a three-dimensional model with Eulerian-Lagrangian approach on a three-dimensional numerical grid applying a modified $k-\epsilon$ turbulence model. A comparison of the predicted flow field with experimental data was not included in this publication. Furthermore, variations of the coefficients of restitution in the particle-wall model from elastic to completely inelastic bouncing behavior have shown only minor influence on the predicted efficiency grade. Derksen [16] presented a prediction of a flow in a high-efficiency cyclone at $Re = 280000$ with numerical investigation. He used calculations using a large eddy simulation (LES) based on the Smagorinsky model, which agree well with experimental data. de Souza and Neto [17] have used subgrid scale Smagorinsky model to predict the behavior of a water-fed hydrocyclone. The numerical results presented the main features of the flow rules and agreed reasonably well with experimental data. The authors suggested that LES represents an interesting alternative to classical turbulence models when applied to numerical solution of fluid flows within hydrocyclones.

According to the above literatures, a large number of researchers were devoted to numerically exploring the flow characteristic and design of CCS. However, up to now, few researchers present a study including all structure factors of CCS, such as shape of inlet and outlet, height, and diameter. In this study, different efficiency caused by different factors is investigated, giving a basis of CCS designing.

2. Mathematical Model of Liquid-Gas Cylindrical Cyclone Separator

A classical liquid-gas cylindrical cyclone separator illustrated in Figure 1 is studied for the present computation. The gas and liquid mixtures flow through the inclined inlet section and then, due to the centrifugal force, a swirl causing the gas and liquid to separate is formed. The liquid moves toward the wall and downward, whilst the gas flows toward the center and exits from the upper gas phase outlet.

For the convenience of computation, some assumptions are proposed as follows: (1) the flow state is steady in the separator; (2) the dispersed phase (gas phase) is uniformly distributed in the continuous fluid (liquid phase); (3) the gas and liquid phases are incompressible and the properties of the mixture such as viscosity are constant; and (4) the flow in the cyclone separator is regarded as isothermal; namely, there is no heat transfer between the phases. The conservation equations of the flow phases involved can be written in a

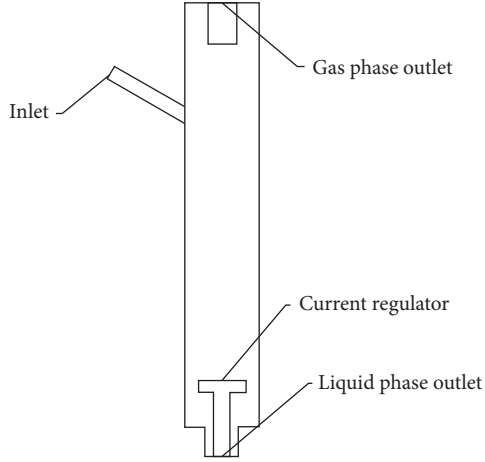


FIGURE 1: The structure diagram of a classical cylindrical cyclone separator.

generalized form based on the Reynolds-averaging model. The equations are presented as follows:

$$\begin{aligned} \nabla \cdot (\rho \bar{u}) &= 0, \\ \nabla \cdot (\rho \bar{u} \bar{u}) &= -\nabla p + \nabla \cdot (\mu \nabla \bar{u}) - \nabla \cdot (\overline{\rho \bar{u}' \bar{u}'}), \end{aligned} \quad (1)$$

in which \bar{u} is the velocity vector, μ is the viscosity, and $\overline{\rho \bar{u}' \bar{u}'}$ is the Reynolds stress tensor.

2.1. Turbulence Model. Numerical methods have been developed to solve (1). At present, standard k - ε model, RNG k - ε model, algebraic stress model, and Reynolds stress model are adopted to numerically simulate the turbulence flow of cyclone separators. In the present paper, the flow in the cyclone separator is strongly swirling flow, which has the anisotropic feature. In order to obtain the values of the Reynolds stress terms, the Reynolds stress model was carried out for its adaptation with the strongly anisotropic flow. The Reynolds stress model enables depicting the complex turbulence flow. The Reynolds stress equation is presented as follows:

$$\frac{\partial \overline{\rho u'_i u'_j}}{\partial t} + \bar{u}_k \frac{\partial \overline{\rho u'_i u'_j}}{\partial x_k} = P_{i,j} + \phi_{i,j} + D_{i,j} - \varepsilon_{i,j}, \quad (2)$$

in which $P_{i,j}$ is the stress production term which is ignored in this paper, $\phi_{i,j}$ is the pressure-strain correlation, $D_{i,j}$ is the diffusion term, and $\varepsilon_{i,j}$ is the dissipation rate of the turbulent kinetic energy. They are presented, respectively, as follows:

$$\phi_{i,j} = -C_1 \rho \frac{\varepsilon}{k} \left(\overline{u'_i u'_j} - \frac{2}{3} k \delta_{i,j} \right) - C_2 \left(P_{i,j} - \frac{2}{3} \rho \delta_{i,j} \right), \quad (3)$$

$$D_{i,j} = \frac{\partial}{\partial x_k} \left(\frac{\mu_t}{\sigma_t} \frac{\partial \overline{u'_i u'_j}}{\partial x_k} \right), \quad (4)$$

$$\varepsilon_{i,j} = \frac{2}{3} \rho \varepsilon \delta_{i,j}. \quad (5)$$

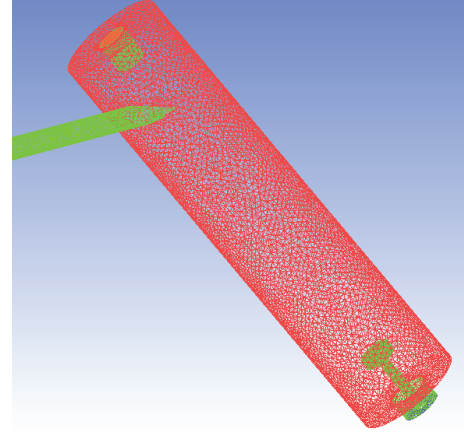


FIGURE 2: The grid distribution diagram of the cylindrical liquid-gas separator.

Otherwise, the turbulent kinetic energy k and the dissipation rate ε are given, respectively, by

$$\frac{Dk}{Dt} = \frac{\partial}{\partial x_l} \left(c_k \frac{k^2}{\varepsilon} \frac{\partial k}{\partial x_l} + \frac{\mu}{\rho} \frac{\partial k}{\partial x_l} \right) - \overline{u'_i u'_l} \frac{\partial u_i}{\partial x_l} - \varepsilon, \quad (6)$$

$$\begin{aligned} \frac{D\varepsilon}{Dt} &= \frac{\partial}{\partial x_l} \left(c_\varepsilon \frac{k^2}{\varepsilon} \frac{\partial \varepsilon}{\partial x_l} + \frac{\mu}{\rho} \frac{\partial \varepsilon}{\partial x_l} \right) - c_{\varepsilon 1} \frac{\varepsilon}{k} \overline{u'_i u'_l} \frac{\partial u_i}{\partial x_l} \\ &\quad - c_{\varepsilon 2} \frac{\varepsilon^2}{k}. \end{aligned} \quad (7)$$

Therefore, the Reynolds stress equations are closed and can be solved.

2.2. Numerical Method and Boundary Condition. Equations were solved numerically through transferring to algebraic equations based on the control volume method. The pressure-velocity coupling algorithm SIMPLE and the QUICK interpolation scheme were used in the numerical simulation. For the consideration of strongly swirling flow in the cyclone separator, the PRESTO! scheme was adopted for pressure discretization. The prototype design of cyclone separator was based on [18]. Figure 2 shows the geometric configuration and mesh distribution of the cyclone separator in this paper, and all the test cases were simulated using unstructured tetrahedral grids generated by a robust method.

Boundary conditions were set as follows: the inlet boundary condition was assumed as velocity inlet condition and the velocities were set for water and methane gas separately. It was assumed that the inlet velocity was uniform. The boundary condition for the wall was regarded as no slip. Finally, the gas phase outlet was regarded as pressure outlet condition as well as the liquid phase outlet, and the pressure was set at atmospheric pressure.

2.3. Turbulence Model Verification. To demonstrate the feasibility of the numerical simulation, a comparative test was carried out. An experiment about the effect of inlet volume flow on the separation efficiency was performed in [18]. In

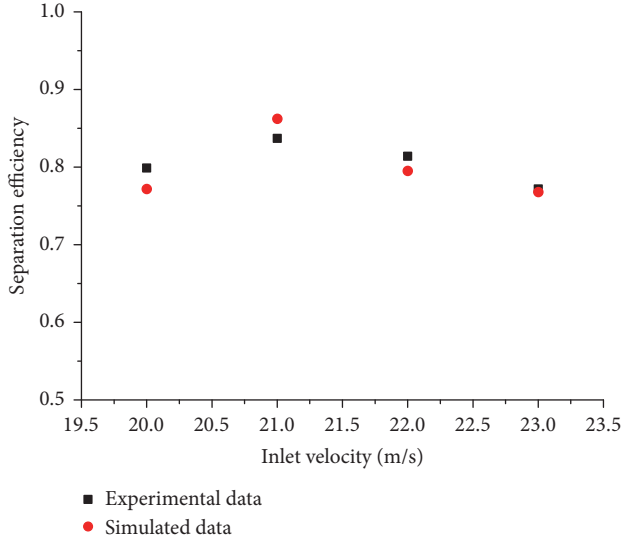


FIGURE 3: The comparison of the simulated data and the experimental data.

the experiment, the mass flow values were set as $11 \text{ m}^3/\text{h}$, $11.5 \text{ m}^3/\text{h}$, $12 \text{ m}^3/\text{h}$, and $12.5 \text{ m}^3/\text{h}$ separately, corresponding to 20 m/s, 21 m/s, 22 m/s, and 23 m/s. The geometric model of the simulation was the same as the separator of the experiment. The inlet is rectangular and the size is $15 \text{ mm} \times 10 \text{ mm}$, the separator length is 840 mm, the diameter is 100 mm, the gas phase outlet diameter is 26 mm, and the liquid phase diameter is 36 mm. The separation efficiency α was defined as the ratio of the gas phase outlet gas content and the inlet gas content, which can be written as follows:

$$\alpha = \frac{m_{g,o}}{m_{g,i}} \quad (8)$$

The comparison of the simulation and the experiment is shown in Figure 3. It can be indicated that there is a good agreement between the experiment data and the simulation data. Therefore, the simulation method in this paper is applicable and flexible.

3. Results and Discussion

In this paper, the effect of some parameters such as separator length, the diameter of the liquid phase outlet and the gas phase outlet, and inlet velocity on the separation efficiency was considered. The values of the parameters were listed in Table 1.

3.1. The Effect of the Separator Length on the Separation Efficiency. The separator length has essential impact on the gas and liquid separation. In this paper, three separators with different lengths are considered. Figure 4 shows the gas volume fraction distribution under three values of length. It can be indicated that, with the increase of the length, the separation performance becomes bad, which can also be deduced from Figure 5 which presents the gas volume

TABLE 1: Different parameters values for simulation test.

Case number	1	2	3
L_s (mm)	440	840	1600
D_g (mm)	16	26	36
D_l (mm)	22	36	50
Inlet shape	Circular	Rectangular	

fraction on the cross section of the gas phase outlet. The reason for the variation of the separation performance may be associated with the tangential velocity and the static pressure distribution. When the length value increases, the liquid-gas mixture stays longer in the cyclone separator, which causes liquid and gas mix again. It can be seen from Figure 6 that the tangential velocity decreases when the length value increases. When the length is 1600 mm, the tangential velocity is almost zero, which demonstrates that the liquid and the gas do not separate. Generally, the separation efficiency is proportional to the tangential velocity. On the other hand, static pressure difference is another important factor for liquid-gas separation. The pressure difference supplies centripetal force of the circular motion in the cyclone separator. When the pressure difference is greater, the trend of the liquid-gas separation is more obvious. Figure 7 shows the distribution of the static pressure with different lengths. It indicates that the pressure difference varies in contrast to the variation of the length; therefore, the separation effect becomes worse with the increase of the separator length.

3.2. The Effect of the Gas Phase Outlet Diameter on the Separation Efficiency. The gas phase outlet diameter is another important parameter. When the liquid and gas separate, the gas forms the gas column close to the center of the separator. The gas phase outlet diameter depends on the size of the gas column. The gas volume fraction distribution with three different gas phase outlet diameters is shown in Figure 8. It can be indicated that the volume fraction increases at the beginning and then decreases when the diameter value is larger than a specific value. This can be explained as follows: when the gas phase outlet diameter is very small, the gas column could not flow out completely from the gas phase outlet. When the diameter is very large, larger than the gas column, the gas column will carry the liquid and flow from the gas phase outlet. It can be seen from Figure 9 that although the average tangential velocity is the largest for the case of $r_g = 13 \text{ mm}$, the difference of the velocity value is not serious.

3.3. The Effect of the Liquid Phase Outlet Diameter on the Separation Efficiency. The liquid phase outlet diameter is also evaluated in this paper. Figure 10 shows the gas volume fraction on the cross section of the gas phase outlet with three different liquid phase outlet diameters. It can be observed that the volume fraction increases at the beginning and then decreases when the diameter value is larger than a specific value. The tangential velocity listed in Figure 11 will give the explanation of the phenomenon. For the case of $r_l = 18 \text{ mm}$, the average tangential velocity is the largest, which leads to the best separation effect. We can see from Figure 10 that

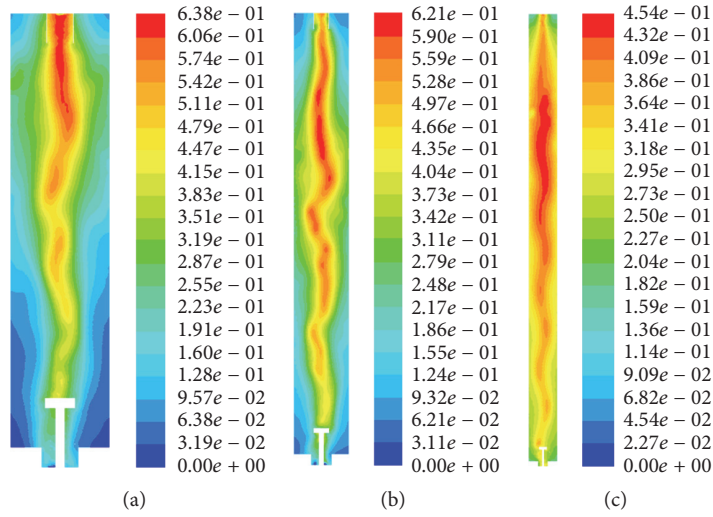


FIGURE 4: The volume fraction of gas with different lengths of the separator: (a) $L_s = 440$ mm; (b) $L_s = 840$ mm; (c) $L_s = 1600$ mm.

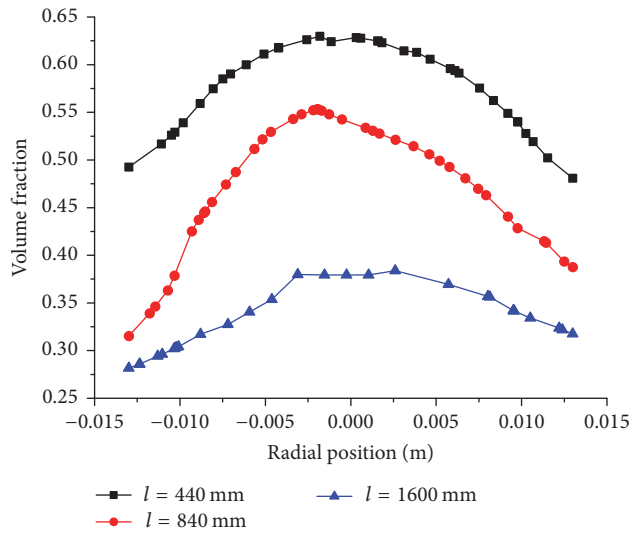


FIGURE 5: The gas volume fraction distribution on the cross section of the gas phase outlet.

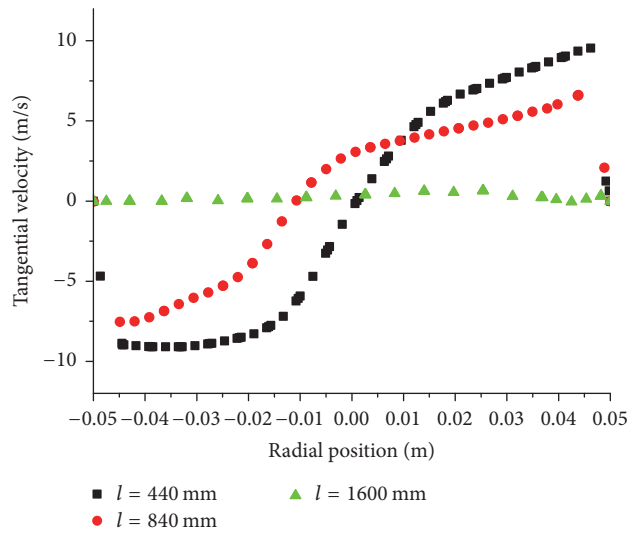


FIGURE 6: Tangential velocity distribution on the cross section of the separator middle position.

TABLE 2: The comparison of separation efficiency with optimized structure.

Case number	1	2	3	4
Inlet shape and size (mm)	Circular ($D = 20$)	Circular ($D = 20$)	Rectangular ($20 * 20$)	Rectangular ($20 * 20$)
Length/diameter (mm/mm)	840/100	440/100	840/100	440/100
Gas phase outlet diameter (mm)	13	13	13	13
Liquid phase outlet diameter (mm)	18	18	18	18
Separation efficiency	66.45%	76.39%	79.04%	86.15%

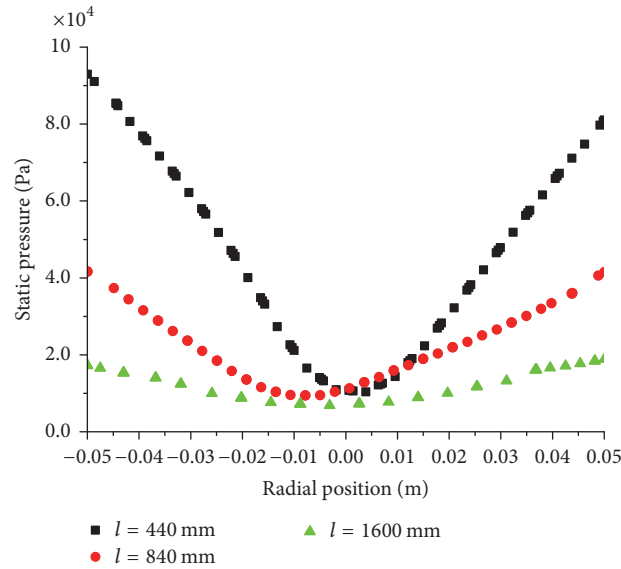


FIGURE 7: Static pressure distribution on the cross section of the separator middle position.

the gas volume fraction increases when the gas is close to the separator center, which demonstrates the existence of the gas column. Figure 11 shows that high tangential velocity occurs in the near-wall region, and it decays rapidly toward the separator center.

3.4. The Effect of the Inlet Shape on the Separation Efficiency.

The inlet shape plays an important role in the optimal design for the reason that it decides the distribution of the incoming gas and liquid and the initial tangential velocity. In this paper, two inlet shapes are considered, that is, rectangular and circular. Figure 12 presents the gas volume fraction distribution on the cross section of the gas phase outlet for two-inlet shape. The maximum value of the volume fraction for the rectangular inlet is above 0.6, but for circular inlet it is about 0.54. In Figure 13, the maximum tangential velocity for the rectangular inlet is 8 m/s, but for circular inlet it is about 7 m/s. As a consequence, the separation efficiency is greater for the rectangular inlet than for the circular inlet. For the rectangular inlet, the incoming flow enters the cyclone separator in tangential direction more easily, which causes the tangential velocity to be less lost. Therefore, the rectangular shape is more suitable for cyclone separator.

Through the above simulations and analysis, it can be indicated that the length of the separator should be shorter,

the diameter of the gas phase outlet and the liquid phase outlet should be appropriate, and the shape of the inlet should be rectangular. The optimal design parameters are listed in Table 2. The optimal design parameters are case number 4 and the separation efficiency is 86.15%.

4. Conclusion

This study carries out the simulation of the flow and liquid-gas separation in the cylindrical cyclone separator with different geometric structures and sizes. The gas volume fraction, tangential velocity, and static pressure are presented and analyzed to evaluate the liquid-gas separation. The following conclusions could be drawn from the results obtained in this investigation:

- (1) For the case of the separator length, the separation efficiency decreases with the increase of the separator length. But the length should be long enough for full separation of liquid and gas.
- (2) The separation efficiency increases firstly and then decreases with the increase of the gas phase outlet diameter, as well as the liquid outlet diameter.

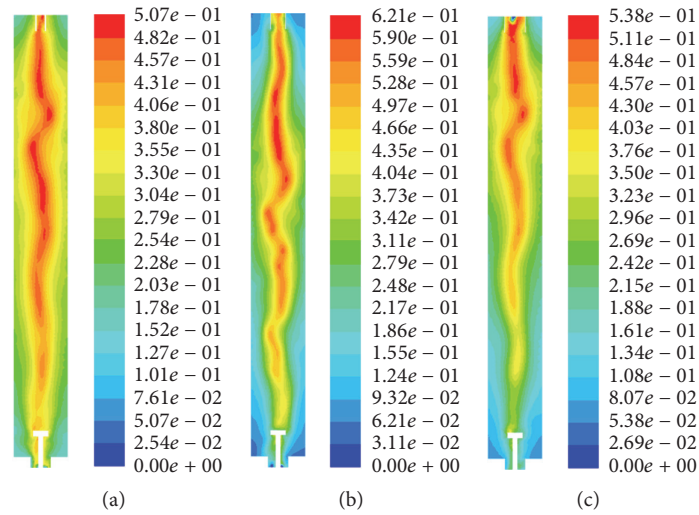


FIGURE 8: The volume fraction of gas with different gas phase outlet diameters: (a) $r_g = 8$ mm; (b) $r_g = 13$ mm; (c) $r_g = 18$ mm.

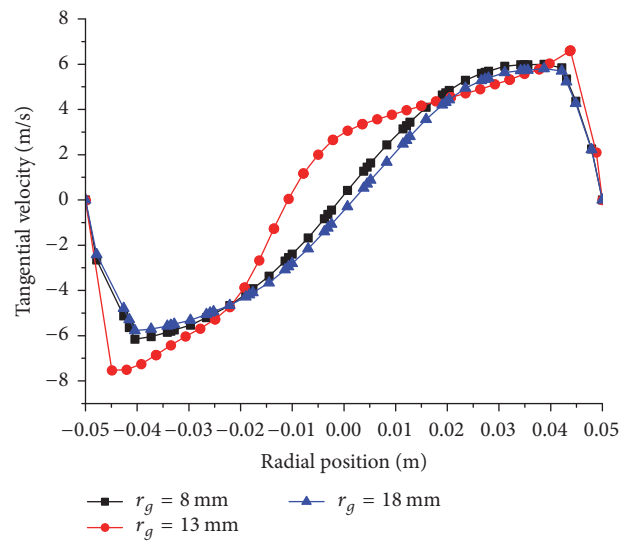


FIGURE 9: Tangential velocity distribution on the cross section of the separator middle position.

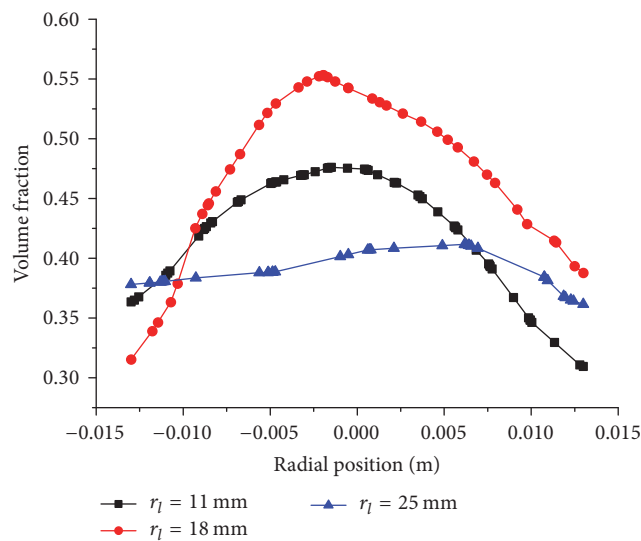


FIGURE 10: The gas volume fraction distribution on the cross section of the gas phase outlet.

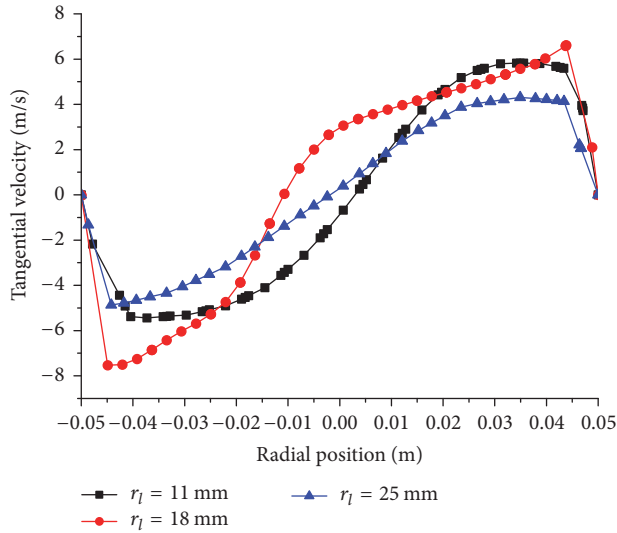


FIGURE 11: Tangential velocity distribution on the cross section of the separator middle position.

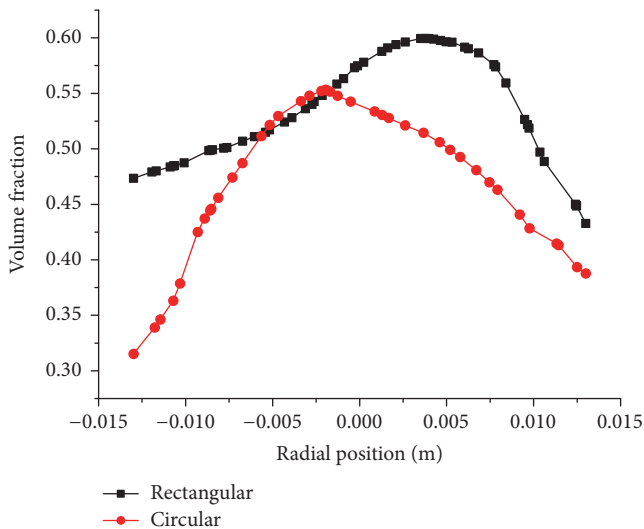


FIGURE 12: The gas volume fraction distribution on the cross section of the gas phase outlet for two-inlet shape.

- (3) For the shape of the inlet, the rectangular inlet is more suitable than the circular inlet, and the separation efficiency changes from 66.45% to 79.04%.
- (4) The optimal geometric structure for the cyclone separator is listed as follows: for the rectangular inlet, the length and diameter ratio is 440/100, the gas phase outlet diameter is 13 mm, and the liquid phase outlet diameter is 18 mm. At the same time, the separation efficiency is 86.15%.

Nomenclature

D : Dynamic viscosity, Pa·s
 k : Turbulent kinetic energy

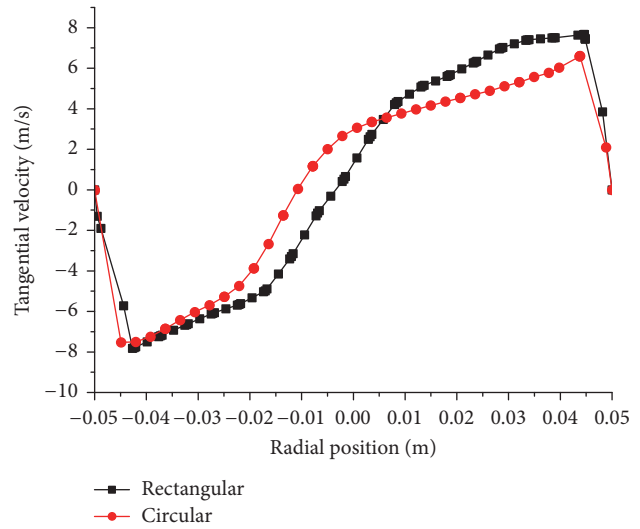


FIGURE 13: Tangential velocity distribution on the cross section of the separator middle position for two-inlet shape.

m : Mass flow rate, kg/s
 p : Static pressure, Pa
 \vec{u} : Velocity vector, m/s
 μ : Dynamic viscosity, Pa·s
 ρ : Density, kg/m³
 ϕ : Pressure-strain correlation
 ε : Dissipation rate of the turbulent kinetic energy
 α : Separation efficiency.

Competing Interests

The authors declare that they have no competing interests.

References

- [1] E. G. Arato and N. D. Barnes, "In-line free vortex separator used for gas/liquid separation within a novel two-phase pumping system," in *Hydrocyclones*, pp. 377–396, Springer, Amsterdam, The Netherlands, 1992.
- [2] R. F. Reydon and W. H. Gauvin, "Theoretical and experimental studies of confined vortex flow," *The Canadian Journal of Chemical Engineering*, vol. 59, no. 1, pp. 14–23, 1981.
- [3] G. E. Kouba, O. Shoham, and S. Shirazi, "Design and performance of gas-liquid cylindrical cyclone separators," in *Proceedings of the BHR Group 7th International Meeting on Multiphase Flow*, pp. 307–327, Cannes, France, June 1995.
- [4] E. Davies and P. Watson, "Miniaturized separators for offshore platforms," in *Proceedings of the 1st New Technology for Exploration & Exploitation of Oil and Gas Reserves Symposium, Luxembourg*, pp. 75–85, April 1979.
- [5] L. E. Gomez, R. S. Mohan, O. Shoham, and G. E. Kouba, "Enhanced mechanistic model and field-application design of gas/liquid cylindrical cyclone separators," *SPE Journal*, vol. 5, no. 2, pp. 190–198, 2000.
- [6] I. Arpandi, A. R. Joshi, O. Shoham, and G. E. Kouba, "Hydrodynamics of two-phase flow in gas-liquid cylindrical cyclone separators," *SPE Journal*, vol. 1, no. 4, pp. 427–436, 1996.

- [7] R. Hreiz, R. Lainé, J. Wu, C. Lemaitre, C. Gentric, and D. Fünfschilling, "On the effect of the nozzle design on the performances of gas-liquid cylindrical cyclone separators," *International Journal of Multiphase Flow*, vol. 58, pp. 15–26, 2014.
- [8] F. Boysan, W. H. Ayers, and J. Swithenbank, "A fundamental mathematical modelling approach to cyclone design," *Transactions of the Institution of Chemical Engineers*, vol. 60, no. 4, pp. 222–230, 1982.
- [9] A. J. Hoekstra, J. J. Derksen, and H. E. A. Van Den Akker, "An experimental and numerical study of turbulent swirling flow in gas cyclones," *Chemical Engineering Science*, vol. 54, no. 13-14, pp. 2055–2065, 1999.
- [10] B. Wang, K. W. Chu, and A. B. Yu, "Numerical study of particle-fluid flow in a hydrocyclone," *Industrial & Engineering Chemistry Research*, vol. 46, no. 13, pp. 4695–4705, 2007.
- [11] K. W. Chu, B. Wang, A. B. Yu, and A. Vince, "CFD-DEM modelling of multiphase flow in dense medium cyclones," *Powder Technology*, vol. 193, no. 3, pp. 235–247, 2009.
- [12] C. T. Crowe and D. T. Pratt, "Analysis of the flow field in cyclone separators," *Computers & Fluids*, vol. 2, no. 3-4, pp. 249–260, 1974.
- [13] S. Movafaghian, J. A. Jaua-Marturet, R. S. Mohan, O. Shoham, and G. E. Kouba, "The effects of geometry, fluid properties and pressure on the hydrodynamics of gas-liquid cylindrical cyclone separators," *International Journal of Multiphase Flow*, vol. 26, no. 6, pp. 999–1018, 2000.
- [14] F. M. Erdal, S. A. Shirazi, O. Shoham, and G. E. Kouba, "CFD simulation of single-phase and two-phase flow in gas-liquid cylindrical cyclone separators," *SPE Journal*, vol. 2, no. 4, pp. 436–445, 1997.
- [15] J. P. Minier and O. Simonin, "A numerical approach of cyclone separators," in *Proceedings of the 2nd European Symposium on Separation of Particles from Gases*, pp. 121–136, Nuremberg, Germany, March 1992.
- [16] J. Derksen, "LES-based separation performance predictions of a stairmand cyclone," in *Proceedings of the 10th Workshop on Two-Phase Flow Predictions, Martin-Luther-Universität Halle-Wittenberg*, pp. 217–226, Halle, Germany, 2002.
- [17] F. J. de Souza and A. S. Neto, "Large eddy simulations of a hydrocyclone," in *Proceedings of the ASME 2002 Joint US-European Fluids Engineering Division Conference*, pp. 559–564, American Society of Mechanical Engineers, Montreal, Canada, July 2002.
- [18] R. Cao, *Numerical simulation and structure optimal of columnar gas and liquid separator [M.S. thesis]*, Daqing Petroleum Institute, 2009.